# Atomic scale simulations of the interactions of plasma species on nickel catalyst surfaces

Proefschrift voorgelegd tot het behalen van
de graad van doctor in de wetenschappen aan
de Universiteit Antwerpen te verdedigen door

**Wesley Somers**

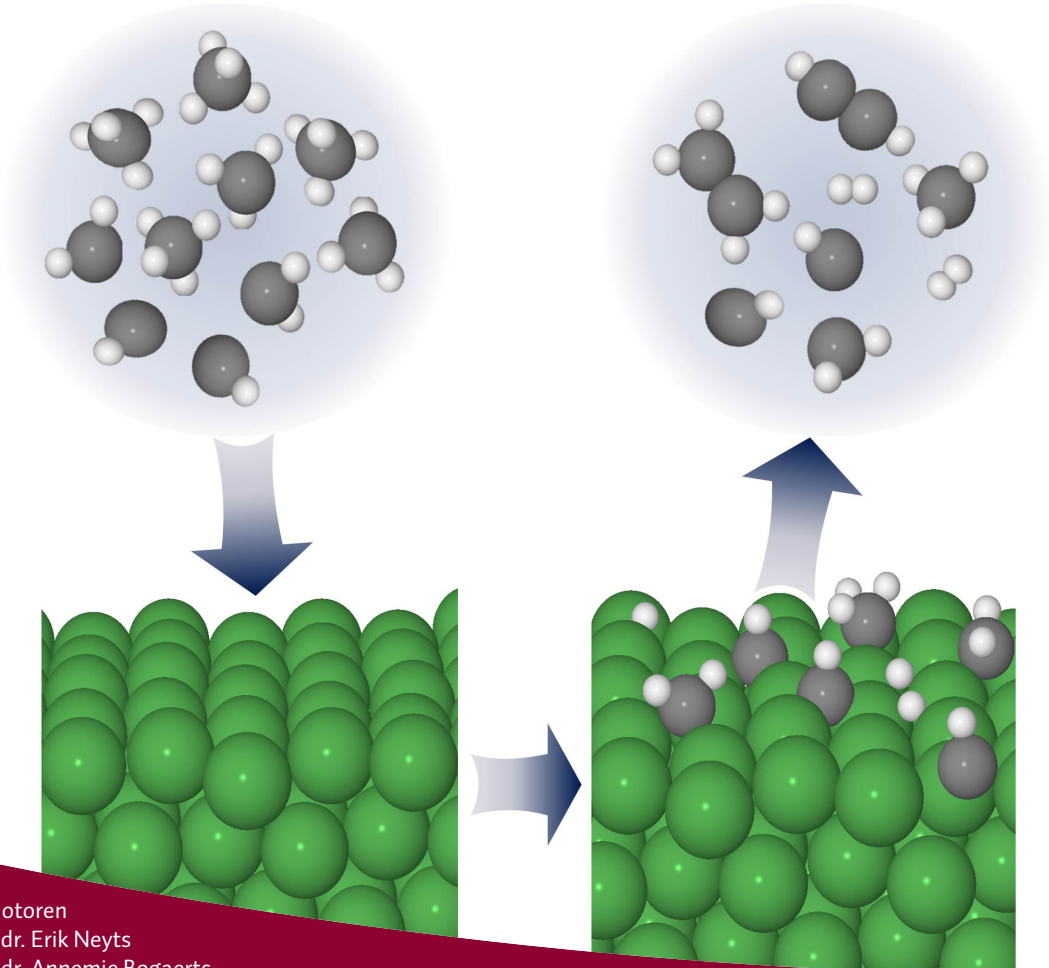

Promotoren
Prof. dr. Erik Neyts
Prof. dr. Annemie Bogaerts

Faculteit Wetenschappen
Departement Chemie

Antwerpen 2015

Universiteit Antwerpen

Universiteit Antwerpen

Faculteit Wetenschappen
Departement Chemie

# Atomic scale simulations of the interactions of plasma species on nickel catalyst surfaces

# Simulaties op atomaire schaal van de interacties van plasmadeeltjes op nikkel katalysatoroppervlakken

Proefschrift voorgelegd tot het behalen
van de graad van doctor in de wetenschappen
aan de Universiteit Antwerpen
te verdedigen door

**Wesley Somers**

Promotoren: Prof. Dr. Erik Neyts en Prof. Dr. Annemie Bogaerts

Antwerpen, 2015

# Contents

# Acknowledgments

In this section, I want to thank everybody who helped and encouraged me during my research.

First of all, I would like to express my gratitude to my two supervisors, prof. Erik Neyts and prof. Annemie Bogaerts. Thank you for giving me the opportunity to do this PhD, and for your guidance during the last four years. It is remarkable how you always managed to find time for me in your busy schedules. Our discussions were always to the point, indicating what needed to be done and what problems could occur. I really enjoyed this way of working with both of you.

I am also thankful to prof. A. C. T. van Duin for providing the ReaxFF code that I used during my research.

The Turing HPC infrastructure at the CalcUA core facility of the Universiteit Antwerpen (UA), a division of the Flemish Supercomputer Center VSC, funded by the Hercules Foundation, the Flemish Government (department EWI) and the UA is acknowledged for calculation support.

Next, I would like to thank all my present and former colleagues from the PLASMANT group. You are all great people and I enjoyed working with you.

Special thanks go to Ramses, Robby, Stefan, Wouter VG, Wouter W, Koen and Christophe for the many fun moments, also outside of the university. It is always great to spend time with you. I am also grateful to Maksudbek and Umedjon for the nice atmosphere in our office.

My thanks also go to Luc, Nelly and Ingrid for helping me with the technical and administrative issues that I have encountered during my PhD.

I would also like to thank a couple of people from my personal life, whose friendship is very important to me. Jonathan, Ward, Bastian, Mitch, Tycho, Robbe and Kim, you were always interested in the progress of my research (or studies). Whether we watched football, went for a drink or took a trip, you helped me to relax when I needed to. Thanks for your support.

Finally, my family has been a huge support for me. Especially my parents deserve my utmost gratitude. You have always believed in me and supported me my entire life. Thanks for being there for me.

Wesley Somers, May 2015

# List of Figures

# List of Tables

# Chapter 1:
# Dry reforming and plasma catalysis

In this chapter, a general introduction to the greenhouse gas effect and to plasma catalysis is given, providing the motivation for this thesis. This is followed by explaining the complex nature of plasma catalysis. Possible effects of the plasma on the catalyst, and vice versa, are discussed. Additionally, an overview of the ongoing research on plasma catalysis is given. There is currently very little fundamental knowledge available regarding the mechanisms of plasma catalysis, and computational research may contribute to a better understanding of the operative mechanisms in plasma catalysis. The aim of this PhD dissertation is therefore to obtain more insight in plasma catalysis by performing molecular dynamics simulations, as discussed in the final part of this chapter.

# 1.1. Introduction

### 1.1.1. Greenhouse gases

Greenhouse gases (GHGs) are the type of gases that prevent heat from escaping the Earth's atmosphere. Without these gases, the average surface temperature would be around -6°C, while the actual value is about 15°C [1–5]. However, human activities have significantly increased the GHG concentrations in the atmosphere, which leads to an enhanced greenhouse effect and eventually, climate change [6].

The gases in the Earth's atmosphere that induce the greenhouse effect are water vapor, carbon dioxide, methane, nitrous oxide and chlorofluorocarbons. Most of these gases have a specific global warming potential (GWP) to indicate to what extent they contribute to the greenhouse effect. As a reference value, the GWP of carbon dioxide is set equal to one. The GWPs are summarized in Table 1.1, together with the average lifetime of the GHGs [6]. Most anthropogenic emitted GHGs are $CO_2$, mainly emitted through burning of fossil fuels and industrial processes, and $CH_4$, while the emissions of greenhouse gases with high GWP values remain low.

**Table 1.1:** GWP and average lifetime of different greenhouse gases.

| Greenhouse gas | GWP (over 20 years) | Lifetime (years) |
|---|---|---|
| $CO_2$ | 1 | variable |
| $CH_4$ | 84 | 12.4 |
| $N_2O$ | 264 | 121.0 |
| Chlorofluorocarbons (CFCs) | 100 - 15000 | 1 - 50000 |

The enhanced greenhouse effect has led to global warming, i.e., there is an average surface temperature increase of 0.85°C over the period of 1880 to 2012 [6,7]. The global warming is in turn responsible for a rise in sea level of 0.19 m between 1901 and 2010 [5–7]. These changes may seem small, but they are relevant for the Earth's physical systems. Without proper actions, the

global warming trend and its consequences will only increase. Possible mitigation strategies are an increased use of renewable energy [8] or carbon capture and storage (CCS) or utilization (CCU) facilities [9], or enhancing the energy efficiency of industrial processes [4]. The latter is certainly beneficial for the methane reforming reactions, since these are widely used to convert greenhouse gases into useful products.

### 1.1.2. Enhancing methane reforming as a mitigation strategy

a) Steam and dry reforming of methane

Methane is converted to syngas, i.e. a mixture of $H_2$ and CO, in the so-called steam and dry reforming reactions, which are shown below [10–16].

Steam reforming: $\mathrm{CH_4} + H_2O \rightleftharpoons CO + 3H_2 \quad \Delta\mathrm{H}^0_{298} = 206\ kJ/mol$

dry reforming: $\mathrm{CH_4} + CO_2 \rightleftharpoons 2CO + 2H_2 \quad \Delta\mathrm{H}^0_{298} = 247\ kJ/mol$

Additionally, the high pressure steam reforming can be followed by the exothermic water gas shift (WGS) reaction to produce more $H_2$ and change the $H_2$/CO ratio:

WGS reaction: $CO + H_2O \rightleftharpoons CO_2 + H_2 \quad \Delta\mathrm{H}^0_{298} = -41\ kJ/mol$

Both reforming reactions are endothermic; hence these processes are performed at high temperatures, i.e. in the order of 1000 K [11,17–21]. Furthermore, catalysts are used in these processes, with the commonly used catalysts being Ni, Co, Ir, Pd, Rh or Ru metals supported on metal oxides such as $Al_2O_3$ or $TiO_2$ [22–26].

Syngas is important in various industrial applications, such as the Fischer-Tropsch process for forming liquid hydrocarbons and the Haber-Bosch process to produce ammonia [27,28]. Other chemicals like methanol, dimethyl ether and formic acid are also formed by reactions involving syngas or one of its

components. Methane reforming is thus the initial step in the synthesis of many products. Furthermore, hydrogen is a potential clean energy source as hydrogen fuel cells are highly efficient, without significant emissions. The definitive commercial implementation, however, is impeded by the complexity of safely storing and transporting the fuel. However, car manufacturers continue to invest in research to overcome this issue.

b) Alternative to the conventional methane reforming

Conventional steam or dry reforming of methane is widely used to produce syngas, but the high temperatures require a high energy input. Other important challenges include maintaining the catalyst activity and reducing carbon formation, sintering and sulphur poisoning [29]. In order to overcome these issues, the combination of non-thermal atmospheric plasma technology and catalysis, called plasma catalysis, is proposed as an alternative to the conventional process. This technique seems promising, since the plasma can activate the molecules and induce reactions at reduced temperatures, while the catalyst can increase the selectivity.

Plasma catalysis is, however, very complex and the exact mechanisms of the interactions between the plasma and catalyst are far from understood [22,30,31]. Experimentally, it is difficult to study the process without disturbing the plasma, which changes its properties. Therefore, computational research may be a very useful alternative to obtain fundamental information about the mechanisms.

This PhD dissertation aims to elucidate the interactions of hydrocarbon plasma species at nickel catalyst surfaces by means of computer simulations. For this purpose, molecular dynamics simulations are performed and their capability of describing plasma catalysis is assessed. Before turning to the results of the simulations, more information about plasma technology and plasma catalysis is given in the next sections of this chapter, while a description of the computational details is given in Chapter 2.

# 1.2. Plasma and plasma catalysis

### 1.2.1. Plasmas

A plasma is a completely or partially ionized gas. It is also known as the fourth state of matter, next to solid, liquid and gas. Plasmas typically consist of a large variety of species, including electrons, ions (both positive and negative), photons, radicals, as well as electronically, vibrationally and rotationally excited species. Even though there is a large variety of charged species, a plasma is globally quasi-neutral, i.e. the charges compensate each other.

Both natural and man-made plasmas exist. For instance, the solar corona, lightning and the Aurora Borealis are natural plasmas. Artificial plasmas are created by deliberately adding energy to a gas, for instance by applying an electric field or adding thermal energy, which breaks down the gas into electrons and ions. Laboratory plasmas can be divided in two groups: (1) high temperature or fusion plasmas, and (2) low temperature plasmas or gas discharges. Furthermore, plasmas can also be subdivided as either thermal or non-thermal. In a thermal plasma, all plasma species are in thermal equilibrium, with temperatures in the order of 10000 K and above. In contrast, the temperatures of the various plasma species are not equal to one another in a non-thermal plasma. Specifically, there is no thermal equilibrium between the highly energetic electrons and the other plasma species. This is because the light electrons easily gain energy from the electric field while they are difficult to thermalize through collisions due to their low mass. Only a small part of the electron energy is distributed through collisions, which gives rise to new species and also helps to sustain the plasma. Therefore, the electron temperature is still high, i.e. from 10000 K to 100000 K, while the other species have a temperature in the range of 300 – 1000 K. The electron density in non-thermal plasmas is lower than that in thermal plasmas, i.e. typically less than $10^{20}$ $m^{-3}$ and between $10^{21}$ $m^{-3}$ and $10^{26}$ $m^{-3}$, respectively [32].

In non-thermal plasmas, most energy is thus transferred to the electrons, while the gas temperature remains relatively low. The combination of highly energetic electrons and other reactive species such as ions or radicals can induce certain reactions, which are normally performed under thermal conditions. A typical example of a non-thermal plasma source is the so-called dielectric barrier discharge (DBD). This source has frequently been investigated as a potential alternative for reforming reactions [33–40].

Another interesting type of plasmas is the so-called warm plasma, i.e., a plasma with a high electron temperature and density that is still in local non-equilibrium. An example of a warm plasma that is gaining more attention is the gliding arc discharge, which can be operated in the thermal or non-thermal regime, or even in a transitional regime [41,42].

### 1.2.2. Plasma catalysis

Plasma catalysis is an emerging technique that combines the high reactivity of the plasma with the high selectivity of a catalyst. More importantly, a synergistic effect is sometimes observed, due to the influence of the plasma on the catalyst properties and vice versa. A synergistic effect is obtained when the outcome of plasma catalysis is better than the sum of the separate results of plasma and catalysis. This synergism has been mostly reported for the removal of volatile organic compounds (VOCs) [43–48], although a number of reports also demonstrate such synergism in hydrocarbon reforming [49–52]. There are, however, also some reports that demonstrate a negative effect when combining a plasma with a catalyst for methane reforming [53–56]. This variety in reported effects of plasma catalysis illustrates that its efficiency strongly depends on the precise operating conditions. Indeed, the synergistic effect that is obtained for methane reforming is most common at relatively low temperatures, i.e. below 973 K.

Examples of synergistic effects during the plasma catalytic methane reforming are currently limited. Experimental studies mainly focus on the conversion,

selectivity and energy efficiency of the process, and do not address the mechanisms of the interactions between the plasma and catalyst [43,48,53–65]. Nevertheless, more fundamental knowledge of these mechanisms will increase the insight in plasma catalysis, and is therefore crucial for understanding and optimization of plasma catalysis.

The use of non-thermal plasma to activate the catalyst is interesting because it can significantly reduce the operating temperature compared to the conventional catalytic process. The reduced temperature increases the catalyst stability, since sintering and coking of the catalyst occurs at high temperatures. In practice, the combination of a plasma with a catalyst may be achieved in either a single-stage or two-stage configuration [66,67]. In the single-stage configuration, the catalyst is placed inside the discharge, which allows direct interaction between the plasma and the catalyst. The short-lived species in the plasma, such as vibrationally excited species, will therefore also interact with the catalyst. In the two-stage configuration, the catalyst is positioned either down- or upstream of the plasma. Only long-lived species and stable intermediates will be able to reach the catalyst from the plasma, or vice versa. Since in this case the catalyst is not placed inside the discharge, thermal plasmas can also be used in this configuration without the risk of melting of the catalyst [68,69]. In the rest of this dissertation, we refer to the single-stage configuration of plasma catalysis.

### 1.2.3. Interactions between the plasma and the catalyst

Both the plasma and catalyst properties are changed when they are combined. For instance, the plasma can change the catalyst surface properties by ion, electron or photon interactions. On the other hand, the presence of the catalyst in the discharge can alter its electric properties. An overview of the various effects that the plasma and catalyst have on each other is shown in Figure 1.1, and discussed below [22,30,31].

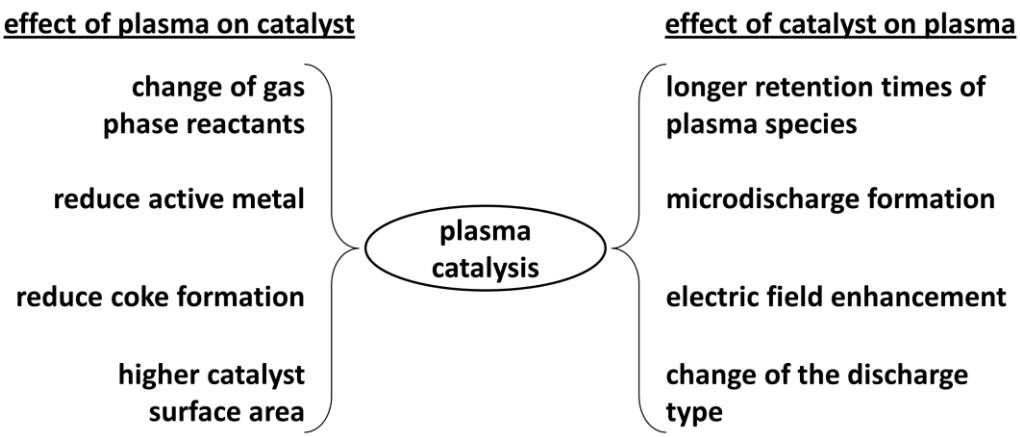


**Figure 1.1:** Overview of the various effects between the plasma and the catalyst.

a) Effect of plasma on catalyst

*Change of gas phase reactants*

The composition of the plasma is different from that of the gas phase in a pure catalytic setup. For the latter, most reactant molecules are in the electronic and vibrational ground state, while the plasma consists of many excited species that can adsorb on the catalyst surface. The vibrationally excited states in the plasma can reduce the activation barrier for some surface reactions [22]. These differences in gas phase reactants and reactivity change the distribution of formed species.

*Reduce active metal*

Metal oxide catalysts can be reduced in the plasma to their metallic form. This has for instance been demonstrated for the reduction of NiO to metallic Ni in a DBD for dry reforming [54,64,65].

*Higher catalyst surface area*

It is demonstrated that the plasma increases the catalyst dispersion, leading to a larger total surface area [70–72]. This increases the catalytic activity

*Reduce coke formation and sintering rate*

The higher dispersion of the active metal might lower the coke formation [63]. Moreover, the lower operating temperature of the plasma also reduces the sintering rate [29,73].

b) Effect of catalyst on plasma

*Longer retention time of plasma species*

When reactant gas molecules are adsorbed on the catalyst surface, the retention time and concentration of these molecules in the discharge will be enhanced. This can lead to additional reactions [22].

*Microdischarge formation*

Microdischarges may be formed inside (sufficiently large) catalyst pores because of a strong electric field in or near these pores [74–76]. For instance, microdischarges are observed inside porous ceramics with pore sizes between 50 and 200 µm [77,78]. The characteristics of these microdischarges are different from those of the plasma. As a consequence, the reaction behavior inside the catalyst pores is also expected to be different.

*Electric field enhancement*

The presence of the catalyst in the plasma induces a packed bed effect at the catalyst surface. The same effect is obtained by inserting dielectric materials in the discharge region [56,79]. Due to charge accumulation on the surface of the packing material, the electric field is enhanced [80]. The extent of the enhancement is determined by the dielectric constant, curvature and contact angle of the packing material [22]. This change in the electric field affects the electron energy distribution in the plasma, and thus the electron impact reactions. Therefore, the chemical composition of the plasma is changed by the presence of the catalyst. It is also possible to use a lower voltage to initiate the discharge because of the reduced discharge gap distance in the reactor. This is also interesting for reducing the energy efficiency of a process.

*Change of the discharge type*

Catalytic pellets can also lead to so-called surface discharges, in which an intensive discharge is formed around the contact points of the pellets [54,80]. This leads to higher electron impact ionization and dissociation rates, and an increase in the concentration of reactive species. Hence, the plasma chemistry in the reactor is changed.

## 1.3. Fundamental studies related to plasma catalysis

As mentioned above, most studies are focused on increasing the conversion, selectivity and energy efficiency of the process, and provide little understanding of the mechanisms in plasma catalysis [43,48,53–65]. However, an increased insight in these mechanisms is necessary to improve the applications of plasma catalysis. Experimentally, not all mechanisms can be addressed, since any disturbance of the plasma changes its properties. This is where computational research may be of interest. The aim of such research is to study specific processes separately, in order to gradually unravel the mechanisms of plasma catalysis. Even so, this still remains challenging because separate modelling of plasma processes and catalysis is already complex. Hence, the combination of both techniques is even more difficult. As a consequence, most computational studies currently focus on either modelling the catalysis process or on the plasma modelling.

### 1.3.1. Plasma chemistry, without catalysis

In addition to experiments, the plasma chemistry without the presence of a catalyst can be simulated with 0D kinetic models and fluid models, typically for a 1- or 2-dimensional system. They can describe density profiles of the plasma species, and give information on production and loss processes, conversion and fluxes of the species towards the walls of the reactor. Such models have been used to study the plasma chemistry in methane reforming and $CO_2$ splitting [81–86]. Ideally, the influence on the electric field of a (catalytic) packing material in the discharge could be simulated in a 3D model.

However, such models have an enormous degree of complexity and are thus difficult to build.

### 1.3.2. Catalysis, without plasma chemistry

On the other hand, the modelling of catalytic processes without the presence of a plasma is typically done at the atomic scale, to gain a molecular level insight. Both density functional theory (DFT) and classical molecular dynamics (MD) simulations are used for this purpose. They provide an accurate description of individual reactions of ground state species on catalyst surfaces.

a) DFT simulations

In a DFT simulation, the energy of the system is expressed as a functional of the electron density, i.e., a density functional. This computational technique is relatively accurate. So-called time-dependent DFT can also handle electronically excited states, which is of interest for plasma systems. However, these simulations often suffer from a high computational cost. Therefore, DFT simulations are typically limited to a very small system size, i.e., in the order of 100 to a few hundred atoms and a short time scale in the order of picoseconds.

In case of methane reforming, the experimental studies mainly focused on the adsorption and decomposition of $CH_4$ on nickel catalysts [87–89]. DFT calculations provided additional information regarding energy barriers of the occurring reactions [90–92].

b) Classical MD simulations

In a MD simulation, the trajectories of all atoms in the system are followed through space and time by integrating their equations of motion. In classical MD, the forces between the atoms are derived from a suitable interatomic potential. This potential is the key component of the simulation. The potential defines an approximate energy landscape instead of the real energy

landscape. They are mostly constructed by fitting the potential parameters against experimental and DFT data. Therefore, the results of the simulations are directly correlated to the accuracy of this fitting procedure. MD simulations cover larger systems for longer time scales compared to DFT simulations, i.e. thousands to millions of atoms on nanosecond time scales. In this dissertation, we used MD simulations to study the reactions of $CH_x$ (x={1,2,3}) radicals and vibrationally excited $CH_4$ on several nickel surfaces. A technical description of MD simulations is provided in Chapter 2.

Various MD studies relevant for methane reforming on Ni have been described in the literature [92–95]. In [93], it is observed that the Ni(100) surface is more reactive than the Ni(111) surface, and that a stepped Ni(111) surface has an intermediate reaction rate. Other studies investigated the dissociation of methane and higher hydrocarbons on nickel surfaces, as well as the binding energies of $CH_x$ species on Ni(111) [92,94,95].

These works provided a good description of interactions between several hydrocarbons on different nickel surfaces. However, in most cases these molecules were already adsorbed. A complete sequence of impact, (dissociative) adsorption and desorption is missing. Furthermore, other plasma species such as vibrationally excited molecules are not included in these works. In this dissertation, the possibility of including vibrationally excited $CH_4$ in classical MD simulations is discussed in Chapters 6 and 7.

### 1.3.3. Reactivity of vibrationally excited $CH_4$ on nickel catalyst surfaces

Vibrational excitation occurs when a molecule absorbs a specific quantum of energy to shift the molecule from its ground state to a higher vibrational state, i.e. the energy is transferred to one of the vibrational modes. This may lower the activation barrier for surface reactions, since the energetic state of the reactants is increased [96]. However, experimental [97–103] and computational [104–111] studies on the reactivity of vibrationally excited $CH_4$ illustrate that the reactivity is highly mode-specific.

Methane has four vibrational modes, namely: ($\nu_1$) symmetric C-H stretch, ($\nu_2$) symmetric bend, ($\nu_3$) antisymmetric C-H stretch and ($\nu_4$) antisymmetric bend vibration. The vibrational efficiency, $\eta_{vibr}$, of a vibrational state indicates whether it is more beneficial to add energy to vibrational motion ($\eta_{vibr} > 1$) or to translational motion ($\eta_{vibr} < 1$). The vibrational efficiency is derived from the energy difference ($\Delta E$) between the adsorption curves of the ground and vibrationally excited state of $CH_4$ and the added vibrational energy ($\Delta E_{vibra}$):

$$\eta_{vibr} = \frac{\Delta E}{\Delta E_{vibra}} \tag{1.1}$$

The reported $\eta_{vibr}$ values of several vibrationally excited $CH_4$ states on Ni(111) and Ni(100) are summarized in Table 1.2 [112,113].

**Table 1.2:** Vibrational efficiencies of different vibrational states on Ni(111) and Ni(100) reported in literature. The *-marker denotes that the shape of the adsorption curve is not fully determined.

| vibr. state | surface | $\eta_{vibr}$ | reference |
|---|---|---|---|
| $\nu_3$ | Ni(111) | 1.25 | [102] |
| $2\nu_3$ | Ni(111) | 0.90 | [103] |
| $3\nu_4$ | Ni(111) | 0.72 | [98] |
| $\nu_1$ | Ni(100) | 1.40* | [100] |
| $\nu_3$ | Ni(100) | 0.94* | [99] |
| $2\nu_3$ | Ni(100) | 0.96 | [101] |
| $3\nu_4$ | Ni(100) | ≤ 0.50* | [98] |

As indicated in Table 1.2, not all adsorption curves are fully determined. Furthermore, it is experimentally difficult to excite a large fraction of $CH_4$ to the $\nu_1$ and $\nu_2$ vibrational mode. These modes are Raman-active, while the $\nu_3$ and $\nu_4$ modes are strongly IR-active. The Raman excitation is less efficient than the IR absorption in producing significant quantities of excited state molecules. As a consequence, no experimental data of the $\nu_2$ vibrational mode is available. Therefore, a full computational analysis of the efficiency of vibrationally excited $CH_4$ is highly desirable for gaining full insight in the interaction of vibrationally excited $CH_4$ molecules with surfaces.

## 1.4. Aim of this work and structure of the thesis

The aim of this dissertation is to increase the insight in plasma catalysis by performing molecular dynamics simulations of the interactions of plasma species on nickel catalyst surfaces. Furthermore, the capability of this simulation type for describing plasma catalysis is assessed. The studied plasma species are $CH_x$ (x={1,2,3}) radicals and vibrationally excited $CH_4$. These particles are allowed to impinge on in total six different nickel surfaces. More information about the simulation method and the nickel surfaces is given in Chapter 2.

In Chapter 3, we investigate the interactions of the $CH_x$ radicals on the nickel surfaces at a temperature of 400 K. The simulations provide results regarding the adsorption probability and reactivity after adsorption of the radicals, as a function of the nickel surface.

In Chapter 4, the emphasis is on the temperature influence on $H_2$ formation following $CH_x$ impacts on Ni(111). The studied temperature range is 400 K – 1600 K, in which both $H_2$ formation as C-diffusion into the surface are followed.

In Chapter 5, the influence of temperature and surface structure on the reactivity of the $CH_x$ radicals is investigated. We investigate if there is a correlation between the C-H bond breaking probability of the adsorbed radicals and $H_2$ formation on each surface.

In Chapter 6, the scope of the research is extended towards the reactivity of vibrationally excited $CH_4$. Such excitation is normally described with a quantum mechanical approach. Therefore, in this chapter, an approach is developed to include vibrational motion in MD simulations.

In Chapter 7, the accuracy of the approach to include vibrational motion described in Chapter 6 is validated. This is done by performing impacts of vibrationally excited $CH_4$ on Ni(111), and comparing the results with literature. Possible corrections and limitations of the approach will be discussed.

# Chapter 2:
# Description of the model

In this chapter, the basics of classical molecular dynamics simulations are explained. In this simulation technique, the time evolution of a set of interacting atoms is followed by integrating their equations of motion. The integration is performed with the velocity-Verlet algorithm, while we use the ReaxFF potential to derive the forces between the atoms. Furthermore, the Berendsen and Bussi thermostats, which control the temperature of the simulation, are explained. In the final part of this chapter, the six different nickel surfaces that are used in this dissertation are described.

## 2.1. Introduction

Computer simulations provide a theoretical basis for understanding experimental observations and results. In a real experiment, the parameter dependencies make it very difficult to study the influence of one parameter, without affecting the other parameters. In a computer simulation however, specific parameters may be changed, while the other parameters remain constant. Ideally, experimental and computational studies are combined to explain obtained results, and to predict the result of changing the operating conditions.

As mentioned in the previous chapter, density functional theory (DFT) and classical molecular dynamics (MD) simulations are two techniques used to study processes at the atomic scale. Even though DFT calculations are very accurate, the very small system size (100 to a few hundred atoms) and time scale (in the order of picoseconds) does not allow a full dynamical study of the interactions of plasma species on nickel surfaces. Therefore, classical MD simulations are used in this dissertation to study the sequence of impacts and reactions of $CH_x$ radicals on the surfaces. This simulation type has a larger system size and time scale compared to DFT, i.e., thousands to millions of atoms in nanosecond time scales. However, it is important to realize both the strengths and limitations of this simulation type. For instance, classical MD is less accurate than DFT. The parameters of the potential that is used to calculate the forces acting on the atoms are fitted to experimental and DFT data. Hence, the potential can only be as accurate as the data it is fitted to. Furthermore, the simulations are also limited with respect to the timescale they can handle, even though this is longer compared to DFT. Specifically, if certain reactions are not observed during the MD simulations, it does not necessarily mean that these reactions will not take place at all. The time scale of the MD simulations is possibly too short for these reactions to occur. Finally, it is also difficult to describe electronic or vibrationally excited states in classical MD simulations (see Chapters 6 and 7).

The microscopic information (atomic positions, velocities,…) that is generated in MD simulations is not directly comparable with experimental data. In order to make such a comparison, the microscopic state (microstate) of a system is converted to macroscopic terms (temperature, pressure,…) by statistical mechanics.

The trajectories of *N* atoms in the system can be considered as time-dependent coordinates in a 6*N* dimensional phase space, since there are 3*N* positions and 3*N* momenta. At any moment, the configuration of the system is thus defined by these 6*N* coordinates, i.e., a particular point $\Gamma$ in phase space. The instantaneous value of a physical property *A* is determined as a function of $\Gamma$. Each time step, the configuration of the system changes, and so $\Gamma$ and *A* are time-dependent. The average over all the different configurations obtained over time results in a set of configurations distributed according to a statistical ensemble. The value of a physical property *A* is thus obtained as the average over its various instantaneous values:

$$A_{obs} = \langle A \rangle_t = \lim_{t_{obs}\to\infty} \frac{1}{t_{obs}} \int_0^{t_{obs}} A\big(\Gamma(t)\big)\, dt \tag{2.1}$$

A typical MD simulation is made over a large finite number of time steps, $n_{obs}$, so equation 2.1 is rewritten as follows:

$$A_{obs} = \langle A \rangle_t = \frac{1}{n_{obs}} \sum_{n=1}^{n_{obs}} A\big(\Gamma(n)\big) \tag{2.2}$$

## 2.2. Classical Molecular Dynamics simulations

### 2.2.1. Newtonian dynamics

In this dissertation, we performed classical MD simulations, in which the trajectories of all atoms in the system are followed through space and time by integrating their equations of motion. The atoms in these simulations are point masses, while in reality, atoms are quantum mechanical particles. The

Schrödinger equation should be solved to correctly describe the system at the atomic level. However, solving the equation is not possible for systems with many atoms. This issue is solved in classical MD by disregarding the existence of electrons and making use of a (approximate) potential energy function, ensuring that the atomic interactions can be described as a function of the positions of the nuclei only.

The motion of the atoms in the simulations is then described by integrating Newton's equations of motion:

$$\boldsymbol{F}_i = m_i \boldsymbol{a}_i = m_i \frac{d^2 \boldsymbol{r}_i}{dt^2} \tag{2.3}$$

Where $\boldsymbol{F}_i$ is the force on atom *i*, $m_i$ the mass, $\boldsymbol{r}_i$ the position and $\boldsymbol{a}_i$ the acceleration of the atom. The force acting on an atom determines its acceleration and velocity, and thus, its new positions as a function of time. More information about the integration algorithm that is used in this dissertation is given in §2.2.2.

The force on the atom is calculated as the negative derivate of the potential energy (*U*), which is dependent of the atomic positions:

$$\boldsymbol{F}_i = -\nabla_{\mathbf{r}_\mathrm{i}} \mathrm{U}(\mathbf{r}_\mathrm{i}, \dots, \mathbf{r}_\mathrm{N}) \tag{2.4}$$

This equation illustrates the need for an accurate interatomic potential, since the entire time evolution depends on the potential. Note that MD is a deterministic simulation technique, i.e., once the initial positions and velocities are chosen, the further time evolution is completely determined.

As stated above, the use of a good potential is essential for the reliability of the results. All simulations presented in this dissertation are performed with the reactive force field ReaxFF. More information about this potential is given in §2.3.

### 2.2.2. Numerical integration

Various algorithms have been developed to perform the integration of the equations of motion. Such an algorithm should be accurate, time reversible, robust, symplectic (i.e., conserve phase space density) and permit a long time step. The so-called velocity-Verlet algorithm is a simple yet good algorithm that fulfills these conditions, and it is therefore used in this dissertation [114]. It calculates the velocities of the atoms in two steps, by using both the current and new values of the acceleration $\boldsymbol{a}$. It is a more convenient variant of the Verlet algorithm, in which the velocities of the atoms are calculated in one step.

The velocity-Verlet scheme is as follows:

$$\boldsymbol{r}(t+\Delta t) = \boldsymbol{r}(t) + \boldsymbol{v}(t)\Delta t + \frac{1}{2}\boldsymbol{a}(t)\Delta t^2 \tag{2.5}$$

$$\boldsymbol{v}\left(t+\frac{1}{2}\Delta t\right) = \boldsymbol{v}(t) + \frac{1}{2}\boldsymbol{a}(t)\Delta t \tag{2.6}$$

Calculate new force: $\boldsymbol{F}(t+\Delta t)$

$$\boldsymbol{a}(t+\Delta t) = \boldsymbol{F}(t+\Delta t)/m \tag{2.7}$$

$$\boldsymbol{v}(t+\Delta t) = \boldsymbol{v}\left(t+\frac{1}{2}\Delta t\right) + \frac{1}{2}\boldsymbol{a}(t+\Delta t)\Delta t \tag{2.8}$$

Here, $\boldsymbol{v}$ is the velocity of the atom and $\Delta t$ is the time step. The velocity-Verlet algorithm allows the calculation of kinetic and potential energy at the same time. Furthermore, the error on the velocities is reduced compared to the basic Verlet scheme. The excellent long-time energy conservation is another important strength of the velocity-Verlet algorithm. With a longer time step, a longer physical time is simulated. However, too long time steps will cause energy drifts. In this dissertation, we used a time step of 0.25 fs.

### 2.2.3. Temperature control

In a standard MD simulation, the number of particles in the simulation box (N), the volume (V) of the box and the total system energy (E) remain constant. This isolated system corresponds to the microcanonical (or NVE) ensemble. In this ensemble, the instantaneous temperature, *T(t)*, is calculated as a function of the total kinetic energy of the system:

$$T(t) = \frac{\sum_i^N m_i \boldsymbol{v}_i^2(t)}{3k_B N} \tag{2.9}$$

Here, $k_B$ is the Boltzmann constant and *N* the number of particles. The instantaneous kinetic and potential energy will fluctuate around an average value at equilibrium, and so will the temperature.

In this dissertation, MD simulations of particle impacts on a substrate with a defined temperature are performed. However, the NVE ensemble is not suited for such a process. Indeed, the energy transfer between the particle and substrate during the impact causes a local temperature rise of the substrate. This heat should be dissipated in order to keep the substrate near the desired temperature, but this is not possible in the isolated system. Therefore, other ensembles that control the temperature of the system are used to mimic the thermal dissipation. In this dissertation, we used the Berendsen [115] and Bussi [116] thermostat to control the temperature. These thermostats adjust the atomic velocities in order to enforce the desired temperature. Clearly, the rescaling of the atom velocities does not conserve the total energy.

a) Berendsen thermostat

This method couples the system to an external heat bath [115]. The temperature is then controlled by rescaling the atomic velocities at each time step with the factor $\lambda$:

$$\mathbf{v}_i' = \lambda \mathbf{v}_i \tag{2.10}$$

The scaling factor $\lambda$ is calculated as follows:

$$\lambda = \sqrt{1 + \frac{\Delta t}{\tau}\left(\frac{T_{set}}{T} - 1\right)} \tag{2.11}$$

Here, $\Delta t$ is the time step, $\tau$ is a coupling parameter determining the strength of the heat bath, $T_{set}$ is the desired temperature and $T$ is the instantaneous temperature of the system. Typical values of $\Delta t/\tau$ vary between 1.0 and 0.001. If the value of $\tau$ is too high, the system is coupled to a weak heat bath. As a result, there is almost no velocity correction ($\lambda \approx 0$), and the microcanonical ensemble is recovered. On the other hand, if the value of $\tau$ is too small, the system is forced to the desired temperature without allowing significant temperature fluctuations. Note that even with a value of $\tau$ between these limits, the fluctuations in thermodynamic properties do not correspond to the true canonical NVT ensemble. Because of this, Bussi et al. proposed another method for controlling the temperature that samples a correct canonical distribution.

b) Bussi thermostat

The Bussi thermostat also rescales the velocities with a factor, $\alpha$, to enforce the correct distribution for the kinetic energy corresponding to the desired temperature [116]. It uses Hamilton's or Newton's equations to evolve the system for a single time step, after which the kinetic energy is calculated. This is followed by evolving the kinetic energy for a single time step by using a auxiliary stochastic procedure. Finally, the velocities are rescaled to enforce this new value of the kinetic energy. The Bussi thermostat thus differs from the Berendsen thermostat in the way the scaling factor is calculated. Whereas the Berendsen formalism relies on a simple deterministic function to obtain the rescaling factor during each time step, Bussi's approach is a stochastic procedure where the rescaling factor is randomly sampled from a specified distribution. In contrast to the Berendsen thermostat, this thermostat is able to correctly generate the canonical ensemble.

The scaling factor is calculated as follows:

$$\alpha^2 = \mathrm{e}^{-\frac{\Delta t}{\tau}} + \frac{\overline{K}}{N_f K}\left(1 - \mathrm{e}^{-\frac{\Delta t}{\tau}}\right)\left(R_1^2 + \sum_{i=2}^{N_f} R_i^2\right) + 2\mathrm{e}^{-\frac{\Delta t}{\tau}} R_1 \sqrt{\frac{\overline{K}}{N_f K}\left(1 - \mathrm{e}^{-\frac{\Delta t}{\tau}}\right)} \quad (2.12)$$

Here, *K* is total kinetic energy, $\overline{K}$ the average kinetic energy, $N_f$ the number of degrees of freedom, $R_i$ a Gaussian-distributed random number and $\tau$ a coupling constant, similar to the one in the Berendsen formulation.

### 2.2.4. Periodic boundaries

Typically, MD simulations contain a limited number of atoms compared to the number of atoms in a macroscopic system. A part of these atoms is located near the walls of the simulation box. If these walls are treated as rigid boundaries, the movement and reaction behavior of the atoms near the walls is different than those in the bulk area. This is prevented by using periodic boundary conditions. With this method, the atoms are still contained in the simulation box, but there are no physical walls. The central simulation box is replicated in the desired directions, forming an infinite lattice. In our simulations, periodic boundary conditions are applied in the {x,y} directions. Therefore, the surface is considered as a free infinite surface. An atom that leaves the central simulation box on one side will be replaced by its image that enters the central simulation box on the opposite side. This guarantees that the number of atoms in the central simulation box is conserved.

The potential energy is calculated as a function of the atomic positions. When using periodic boundary conditions, an atom can interact with other atoms, or with the images of these atoms. These interactions occur as long as the atoms or the images are located within the cut-off radius of the interatomic potential. Clearly, an atom should not interact with an image of itself, and it may only interact once with another atom or with the image of that atom. These conditions are fulfilled with the minimum image criterion, which states that the distance between any pair of atoms is the shortest possible distance between them.

## 2.3. ReaxFF potential

### 2.3.1. Overview

ReaxFF is a reactive force field with parameters that are optimized from quantum mechanical (QM) calculations for reaction energies, reaction barriers, configuration energies and geometrical and structural data. This QM based optimization results in an accurate potential, that can simulate bond breaking and formation processes. It is called a reactive force field because the connectivity is determined by bond orders that are calculated from interatomic distances, which in turn, are determined every MD step. ReaxFF is capable of describing both covalent and ionic bonds, as well as the entire range of intermediate interactions. This is possible for a large variety of elements and their compounds, such as hydrocarbons [117–119], metals and metal-catalysed reactions [120,121], and silicon and silicon dioxide [122].

In this dissertation, the force field parameters for the Ni/C/H set developed and validated by Mueller and co-workers are used [93]. The ReaxFF parameters are fitted against QM results, which are obtained from both periodic and cluster ab initio calculations. The parameters are optimized to accurately describe the binding energies of hydrocarbons at the nickel surface, subsurface and bulk sites. For instance, the dehydrogenation barriers of $CH_4$, and the migration energies of H- and C-atoms into the bulk obtained with ReaxFF are in agreement with the QM values. Furthermore, the ReaxFF parameters are also optimized against the heats of formation of nickel carbides. In ReaxFF, the face center cubic (fcc) structure of nickel is the energetically most favorable structure, with an expansion/compression curve that is similar to the curve obtained from QM calculations. The equilibrium lattice spacing of the fcc structure in ReaxFF is equal to 3.656 Å. This is in agreement with the QM value of 3.54 Å and the experimental value of 3.524 Å [123].

### 2.3.2. Potential functions

The total system energy is divided over partial energy terms, related to pair interactions, lone electron pairs, atomic over- and undercoordination, valence and torsion angles, penalty energy, conjugation, hydrogen bonding, and van der Waals and Coulomb interactions. The van der Waals and Coulomb interactions are calculated between every pair of atoms, so that ReaxFF describes not only covalent bonds but also non-bonded interactions between all atoms. Furthermore, charge distributions are calculated based on geometry and connectivity using the electronegativity equalization method (EEM) [124]. The total system energy is expressed as follows:

$$E_{system} = E_{bond} + E_{lp} + E_{over} + E_{under} + E_{val} + E_{tors} + E_{pen} + E_{conj} + E_{Hbond} + E_{vdWaals} + E_{Coulomb} \quad (2.13)$$

ReaxFF is based on the bond order/bond distance relationship, introduced by Abell [125] and applied to hydrocarbons by Brenner [126]. It calculates chemical bonds directly from the interatomic distances $r_{ij}$, which are updated every time step. The total bond order for each bond is the summation over the sigma-bonds (single bond), pi-bonds (double bonds) and double pi-bonds (triple bonds):

$$BO'_{ij} = BO'^{\sigma}_{ij} + BO'^{\pi}_{ij} + BO'^{\pi\pi}_{ij} = exp\left[p_{bo,1}\left(\frac{r_{ij}}{r_0^{\sigma}}\right)^{p_{bo,2}}\right] + exp\left[p_{bo,3}\left(\frac{r_{ij}}{r_0^{\pi}}\right)^{p_{bo,4}}\right] + exp\left[p_{bo,5}\left(\frac{r_{ij}}{r_0^{\pi\pi}}\right)^{p_{bo,6}}\right] \quad (2.14)$$

Here, $r_0^{\sigma}$, $r_0^{\pi}$ and $r_0^{\pi\pi}$ are the covalent bond radii of the possible bonds between *i* and *j*, and $p_{bo,1}$ to $p_{bo,6}$ are fitting parameters. After a correction to overcoordination, the correct bond order, $BO_{ij}$, is used to determine the bond energy:

$$E_{bond_{i,j}} = -D_e^{\sigma} \cdot BO_{ij}^{\sigma} \cdot exp\left[p_{be,1}\left(1 - \left(BO_{ij}^{\sigma}\right)^{p_{be,2}}\right)\right] - D_e^{\pi} \cdot BO_{ij}^{\pi} - D_e^{\pi\pi} \cdot BO_{ij}^{\pi\pi} \quad (2.15)$$

here $D_e^{\sigma}, D_e^{\pi}$ and $D_e^{\pi\pi}$ are the dissociation energies of the respective bonds while $p_{be,1}$ and $p_{be,2}$ are bond energy parameters. This equation ensures that the energy and force associated with a bond smoothly go to zero as the bond breaks.

The other energy terms in equation 2.13 are large functions that contain a number of fitting parameters of the force field. A detailed overview of these functions and the used fitting parameters can be found in literature [117,119].

## 2.4. Nickel surfaces

In this dissertation, six different nickel surface structures are considered. Four of these surfaces are flat surfaces with a different crystallinity, consisting of 300 nickel atoms. The remaining two surfaces are step-edged structures, which we denote as $sNi_1$ and $sNi_2$. These two surfaces are included in this dissertation since defect (step) sites may be formed at the catalyst surface in a plasma as a result of, for example, ion bombardment [93,127]. The difference between both surfaces is the length of the steps in order to determine the influence of this deviation in the surface.

All nickel surfaces are first energy-minimized using the conjugate gradient method [128]. This is followed by an isothermal-isobaric (NPT) simulation at the desired temperature to relax internal stresses. Afterwards, the surfaces are equilibrated using either the Berendsen or Bussi thermostat. The used thermostat is specified in each of the following chapters. Note that after the minimization, the atoms in the lowest layer of each surface structure have fixed positions. This prevents that the entire surface moves in the *z* direction in the simulation box. Cleary, this influences the reaction behavior of the lowest nickel atoms. However, our simulations are focused on the reactions that occur near the top of the surface. Furthermore, H- and C-atoms that diffuse through the lowest layer are removed from the simulation.

Maximum 250 consecutive impacts are performed on each surface in this dissertation. The nickel surfaces are sufficiently large for this number of impacts, since not every impact results in adsorption of a radical (see §3.3.2.a, Figure 3.6). Furthermore, the interactions of incoming radicals with other radicals already adsorbed on the surface is also of interest. All six nickel surfaces are shown in Figure 2.1, and are listed below in the same order.

a) Ni(111)

This is the most stable nickel surface and the most abundant surface facet in typical nickel catalysts [129,130]. The 300 atoms are equally divided over 6 layers.

b) Ni(100)

This surface has a higher surface energy than Ni(111) and is also present in nickel catalysts [131]. Again, the 300 atoms are equally divided over 6 layers.

c) Polycrystalline nickel, pNi

The crystallinity of a catalyst surface might change due to the interactions with the plasma. Consequently, this can alter the reactivity of the catalyst. For this reason, a polycrystalline nickel surface is created, to elucidate this effect of change in crystallinity. The structure shows a (111) facet and a (100) facet, as shown in Figure 2.1. Again, the 300 atoms are equally divided over 6 layers.

d) Amorphous nickel, aNi

The amorphous surface is also included to study the effect of change in crystallinity. The 300 atoms are randomly distributed in the cell volume, so separate layers are difficult to distinguish.

e) $sNi_1$

This surface consists of 255 nickel atoms that are distributed over 6 layers in such a manner that the surface has a stepped structure.

f) $\underline{sNi_2}$

This surface consists of 345 nickel atoms that are distributed over 6 layers in such a manner that the surface has a stepped structure.

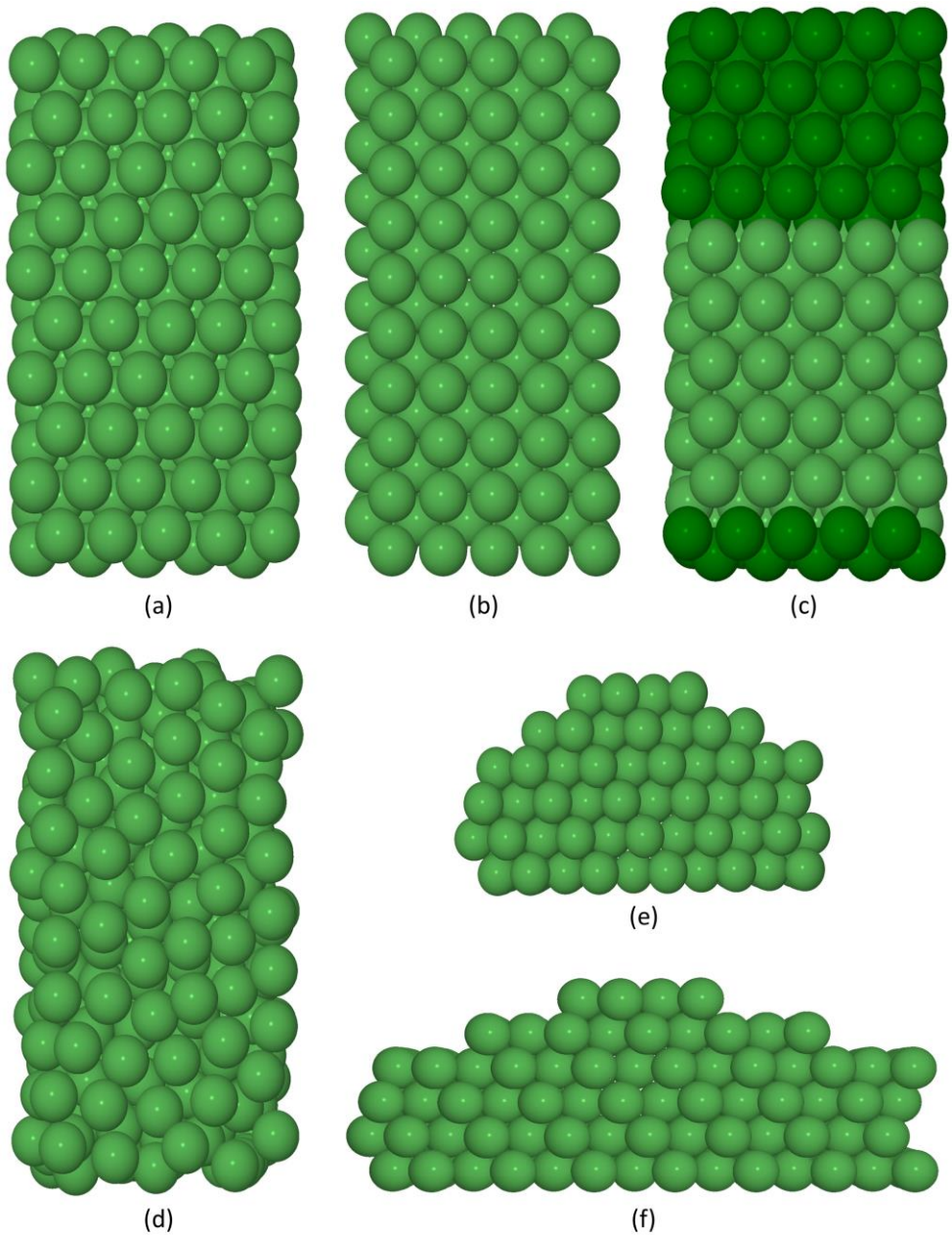


**Figure 2.1:** Top view of (a) Ni(111), (b) Ni(100), (c) pNi, for which the dark green spheres represent the (111) facet and the light green spheres the (100) facet, (d) aNi and side view of (e) $sNi_1$ and (f) $sNi_2$.

# Chapter 3:
# $CH_x$ interactions on various nickel catalyst surfaces at 400 K

In this chapter, the adsorption probability and reaction behavior of $CH_x$ (x={1,2,3}) radicals on various nickel catalyst surfaces is investigated at a temperature of 400 K, which is significantly lower than typical thermal reforming temperatures but characteristic for DBD plasmas. The aim of this study is to increase the insight in (1) the reactivity of the radicals, and (2) the influence of the nickel surface structure on this reactivity.

It is shown that the adsorption probability is related to the number of free electrons of the impacting radical, and to the steric hindrance caused by the hydrogen atoms bonded on the radical. Furthermore, the reactivity after adsorption is found to be high for the $CH_2$ and CH radicals, and to some extent, surface dependent. These results elucidate the reactivity of the radicals at a temperature of 400 K, and they demonstrate the potential of MD simulations to study such reactive systems.

---

This chapter is based on the following publication: W. Somers, A. Bogaerts, A.C.T. van Duin and E.C. Neyts, Plasma Species Interacting with Nickel Surfaces: Towards an Atomic Scale Understanding of Plasma-Catalysis, J. Phys. Chem. C 116 (2012) 20958-20965.

## 3.1. Introduction

As a first step towards a better understanding of the interactions of hydrocarbon plasma species on nickel catalyst surfaces, MD simulations of the impacts of $CH_x$ (x={1,2,3}) radicals on such surfaces are performed at a temperature of 400 K. These simulations have a twofold purpose. First, the results of these simulations are compared with relevant DFT and MD studies that are found in literature. This will enable us to validate our simulations with ReaxFF. Second, these simulations give valuable information concerning the reactivity of the radicals, and the influence of the nickel surface structure on this reactivity.

The validation can be done by comparing with the results of Mueller et al., who studied the dissociation of adsorbed methyl radicals on nickel surfaces as a function of temperature, by means of MD simulations [93]. It was observed that the Ni(100) surface is more reactive than the Ni(111) surface and that a stepped Ni(111) surface has an intermediate reactivity. Although this study does not include the adsorption process of the methyl radical, the influence of the nickel surface after adsorption can be compared to our simulations. Furthermore, since our simulations also include the adsorption process, and $CH_2$ and CH radicals, a more in-depth analysis is possible.

## 3.2. Description of the simulations

### 3.2.1. Nickel surfaces

In this chapter, we consider four different nickel surfaces, i.e., Ni(111), Ni(100) and the stepped structures $sNi_1$ and $sNi_2$ (see section 2.4 above). Comparison of the results on Ni(111) and Ni(100) can elucidate the influence of the connectivity of the nickel atoms on the reactivity after impact of the radicals. Furthermore, by comparing the results on Ni(111) and the stepped surfaces, whose atoms have the same connectivity, the effect of small curvatures or defects can be investigated. Finally, the two step-edged surfaces have the

same number of steps, but the steps have a different size, in order to determine the influence of this deviation in the surface. Prior to the impacts, all four surfaces are first equilibrated at 400 K using the Berendsen thermostat [115] with a coupling constant of 100 fs, followed by a relaxation in the microcanonical ensemble (NVE). In order to simulate an infinite surface, periodic boundary conditions are applied in the {x,y} directions.

### 3.2.2. Simulation method

The impacting species are $CH_x$ radicals (x={1,2,3}), which are typically created in a $CH_4$ discharge at a gas temperature of 400 K [84]. These radicals are added to the system at a *z* position of 10 Å above the top layer of the nickel surface and with random {x,y} coordinates. The initial velocity vector of the incident radical is randomized and its magnitude is set to the root-mean-square velocity corresponding to the substrate temperature of 400 K. Since the incident radical is added to the system at a distance of 10 Å above the top layer, the initial movement of the radical is not influenced by the surface. These random positional and velocity settings guarantee unique starting conditions for each impact.

Both non-consecutive as well as consecutive impacts are performed. The single non-consecutive impacts provide information concerning the reactivity of the impacting plasma species and their reactions after adsorption. Afterwards consecutive impacts are performed to further study the reactions after adsorption, and to mimic experimental conditions. The single non-consecutive impacts, in which each impact occurs on a pristine nickel surface, are followed for 4 ps in the NVE ensemble. When the radical impacts on the surface, it is adsorbed, reflected or decomposed. Each impact of each case is repeated 500 times in order to obtain statistically reasonable reaction coefficients.

Upon impact on the nickel surface, bonds can be formed or broken, which results in an energy change. However, in the NVE ensemble, the total energy

of the system remains constant throughout the simulations and the temperature will change instead of the energy. Experimentally, the change in temperature is dissipated over the surface. However, in the NVE ensemble, this temperature change is not corrected. Therefore, the consecutive impacts are performed as follows. Each impact is first followed in the NVE ensemble for 5 ps. Then, the resulting surface is equilibrated to 400 K with the Berendsen thermostat, to re-equilibrate the system at the correct temperature. This equilibrated surface is subsequently used as the input configuration for the next radical impact. This sequence is continued until clear trends in the adsorption probability and reactivity are observed. The results shown in this chapter are obtained after 150 $CH_3$ impacts, and 200 $CH_2$ and CH impacts. The higher number of simulated $CH_2$ and CH impacts is due to their higher reactivity after adsorption. These consecutive impact simulations take much more time than simulations of single impacts. Because of this, 5 simulations are performed for each radical (instead of 500 simulations for the single, non-consecutive impacts) and the reported results are the averages over these 5 simulations.

## 3.3. Results and Discussion

### 3.3.1. Single, non-consecutive, impacts

a) Adsorption probability

The adsorption probabilities of the three different $CH_x$ radicals on the four different nickel surfaces are depicted in Figure 3.1. The results show that the CH radicals adsorb with the highest probability on all surfaces, followed by the $CH_2$ radicals, with adsorption probabilities around 99 and 90%, respectively. The $CH_3$ radicals have the lowest adsorption probability, ranging from 48.5% on Ni(111) to about 56% on the three other surfaces.

The differences between the adsorption probabilities of the $CH_x$ radicals can be explained by the number of free electrons of the radical. This number increases from one in $CH_3$ to three in CH, leading to a higher reactivity, since

these electrons can bond to the surface. However, the increase in adsorption probability from $CH_3$ to $CH_2$ is not equal to the increase from $CH_2$ to CH. Hence, an additional effect influencing the adsorption process must exist. Indeed, the C-H bonds of the radical cause steric hindrance, which shields the free electrons from the surface, and prevents the radical to bind to it. The higher the number of C-H bonds, the stronger is the steric hindrance, which results in a lower adsorption probability. This is very similar to earlier observations of the reactivity of plasma species in both a-C:H thin film growth [132–134] as well as diamond growth [135–137].

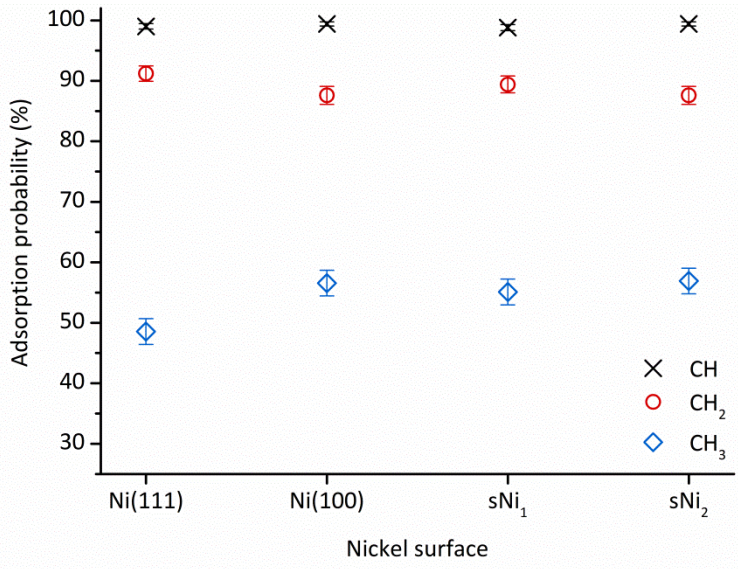


**Figure 3.1:** Adsorption probabilities and associated standard deviations for the single impacts of the $CH_x$ radicals on the four different nickel surfaces.

The difference between the nickel surfaces is most significant for the $CH_3$ impacts. Indeed, the adsorption probability on Ni(100) is about 8% higher than on Ni(111). This difference is related to the connectivity of the nickel atoms in the top layer. In the closer packed Ni(111), each nickel surface atom is connected to six other atoms of the top layer, each at a distance of 2.5 Å. However, in Ni(100), there are only four top layer atoms connected to each nickel surface atom, also at a distance of 2.5 Å. Therefore, the incoming $CH_3$ radical is less hindered by the surrounding atoms on the (100) surface, which implies a weaker steric hindrance of the C-H bonds compared to impacts on

Ni(111). Thus, the reduced connectivity of Ni(100) relative to Ni(111) increases the geometric cross section of the surface nickel atoms, and therefore the surface reaction cross section.

The steps on the nickel surface also influence the adsorption probability of $CH_3$. Indeed, the adsorption probability is 55% and 57% on $sNi_1$ and $sNi_2$, respectively, which is 6.5% and 8.5% higher than on Ni(111). Indeed, the presence of the edges locally increases the reaction cross-section between the incoming radical and the surface, which explains the higher adsorption probability compared to the step-less surface. This can be confirmed by investigating the $CH_3$ binding sites. There are four possible binding sites: $\mu_1$ on-top, $\mu_2$ bridge, $\mu_3$ fcc and $\mu_3$ hcp (see Figure 3.2) [138].

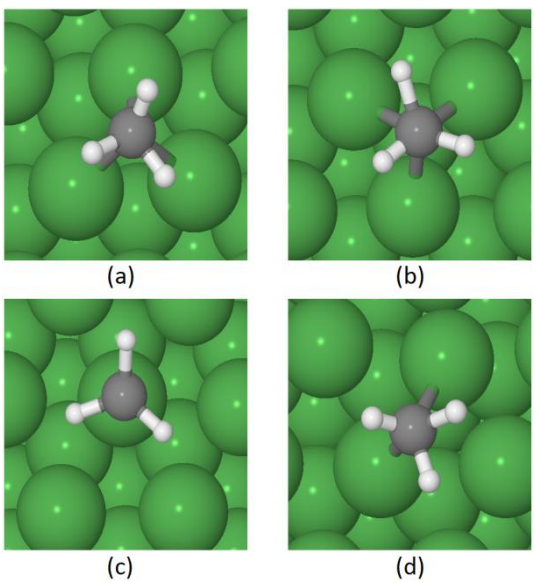


**Figure 3.2:** Four possible binding sites on Ni(111): (a) $\mu_3$ fcc, (b) $\mu_3$ hcp, (c) $\mu_1$ on-top and (d) $\mu_2$ bridge.

On Ni(111), all nickel surface atoms have the same local environment, and almost 40% of the adsorptions take place on a μ1 on-top site, as shown in Figure 3.3. The remaining 60% of the adsorptions is equally divided over the two $\mu_3$ sites. The $\mu_2$ bridging site is only occupied a couple of times. On both stepped surfaces, up to 65% of the adsorptions occur on the $\mu_1$ site, mostly near the edges. Indeed, the local Ni-coordination is lower at this location,

resulting in a higher reactivity. However, the introduction of steps also lowers the fraction of adsorptions on $\mu_3$ sites, since these sites are shielded by the above-lying nickel atoms (cf. Figure 2.1).

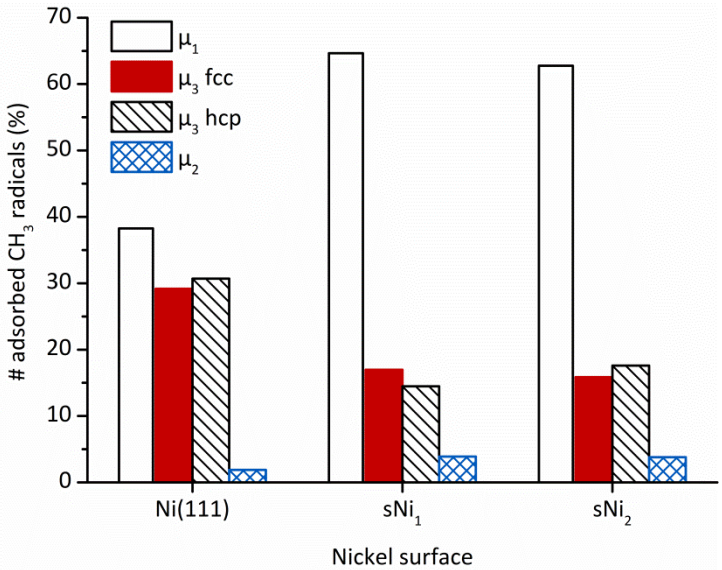


**Figure 3.3:** Occupied adsorption sites of $CH_3$ radicals on Ni(111), $sNi_1$ and $sNi_2$.

For the $CH_2$ and CH impacts, the difference between the adsorption probabilities on the different nickel surfaces is much smaller. As discussed above, the steric hindrance of these radicals is rather limited while their intrinsic reactivity is higher with respect to $CH_3$, such that their adsorption probability is less influenced by steps or surrounding atoms in the top layer of the surface. Clearly, reflection still occurs when the radical impacts with the hydrogen directed straight towards the surface.

b) Reactions after adsorption

After adsorption of the $CH_3$ radicals, we observe that some of the C-H bonds break. This results in the formation of adsorbed atomic hydrogen and $CH_2$ on the nickel surface. After the bond breaking, both $CH_2$ and the H-atom stay connected to the surface, without reacting further during the simulated time. This process of C-H bond breaking occurs in only 1% of the adsorption events in the case of $CH_3$ adsorbed on Ni(111) (see Table 3.1).

On the other surfaces, there is a slight increase in the bond breaking probability for $CH_3$, up to 9% on Ni(100). The overall bond breaking reactivity of $CH_3$ is determined by multiplying these values with the corresponding adsorption probabilities, plotted in Figure 3.1. Since Ni(111) has the lowest adsorption probability and displays the least reactions after adsorption, it is predicted to be the least reactive surface, although the overall reactivity of $CH_3$ on the other surfaces also remains low.

**Table 3.1:** Fraction of broken C-H bonds and the associated standard deviations after adsorption of $CH_3$ on the four different nickel surfaces.

| Nickel surface | Fraction of broken C-H bonds (%) |
|---|---|
| Ni(111) | 1.12 ± 0.65 |
| Ni(100) | 9.00 ± 1.63 |
| $sNi_1$ | 6.60 ± 1.43 |
| $sNi_2$ | 7.35 ± 1.48 |

The reactivity of $CH_2$ is much higher than that of $CH_3$, as illustrated in Figure 3.4. First, the breaking of one C-H bond occurs for more radicals, ranging from 69 % to 85 %. Second, there is also a small fraction of radicals in which both C-H bonds are broken. This can lead to the formation of $H_2$, although in most cases the two hydrogen atoms remain adsorbed on the surface as single atoms. Only 1% of the adsorptions on Ni(111) results in the formation of $H_2$, while the majority of the adsorptions (i.e., ∼85 %) results in cleavage of a single C-H bond. The bond breaking of two C-H bonds without $H_2$ formation does not occur on this surface. Once one C-H bond is broken, the resulting adsorbed CH particle is stable for the remaining simulation time. On the two stepped surfaces, fewer radicals are reacting, although the breaking of the two bonds seems to be more favorable on these surfaces compared to the flat Ni(111) surface.

The highest reactivity is found for Ni(100), since most adsorbed radicals undergo further reactions and this surface has the highest probability for

breaking both C-H bonds (with and without $H_2$ formation). In contrast to $CH_3$, the adsorption probabilities of $CH_2$ on the four surfaces are quite similar, such that the difference in overall bond breaking reactivity is mainly determined by the reactions after adsorption. This makes Ni(100) the most reactive surface for the $CH_2$ impacts. Indeed, the surface energy of Ni(100) is higher than that of Ni(111), with reported values between 1.487 and 2.426 J/m² for Ni(100) and 1.171 and 2.011 J/m² for Ni(111) [131]. Using ReaxFF, we find a surface energy of 2.0 $J/m^2$ for Ni(100) and a value of 1.2 $J/m^2$ for Ni(111), thus corresponding well with the average literature values. The higher surface energy of Ni(100) increases the reactivity of the surface, as observed in our results. The results also imply a higher surface energy for the stepped surfaces compared to the Ni(111) surface, but unfortunately, no data for the surface energy on stepped Ni(111) surfaces is found to validate this observation. However, previous works on the dissociation of $CH_4$ [139] and CO [140] on the terraces and steps of Ni(111) surfaces described the higher reactivity along the steps of the surface. This is in good agreement with our findings.

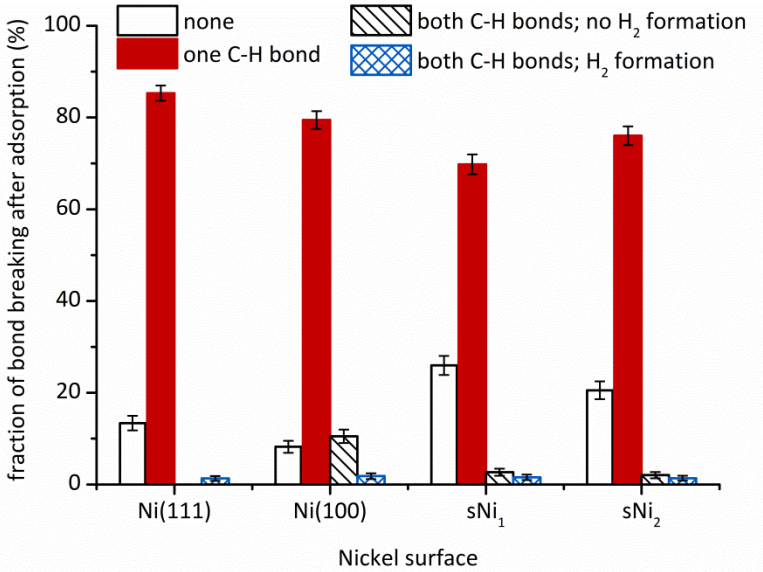


**Figure 3.4:** Observed C-H bond breaking and the associated standard deviations after adsorption of $CH_2$ on the four different nickel surfaces.

Finally, for the CH radicals, the highest reactivity is also found on the Ni(100) surface. Besides C-H bond breaking, diffusion of carbon atoms into the surface

is also observed for these impacts. Mostly, the C-atoms remain on top of the surface after the C-H bond cleavage (see Figure 3.5). In only 6% of the adsorption events, the carbon atom diffuses into the nickel surface once the C-H bond is broken. The three other surfaces, i.e. with the (111) facet, have an equal probability of bond cleavage without diffusion of the carbon atom into the surface. However, the stepped structures show a higher percentage of carbon atoms diffusing inwards, to interstitial sites between the top layer and the first subsurface layer. Corresponding to their relative stabilities, we observe a preferential occupation of the octahedral sites relative to the tetrahedral sites. The presence of step-edges in the structure thus lowers the penetration barrier of the top layer, making it easier for the carbon atoms to diffuse to the first subsurface layer. The results for $sNi_1$ and $sNi_2$ are very similar, which indicates that the difference in size of the steps hardly has an influence.

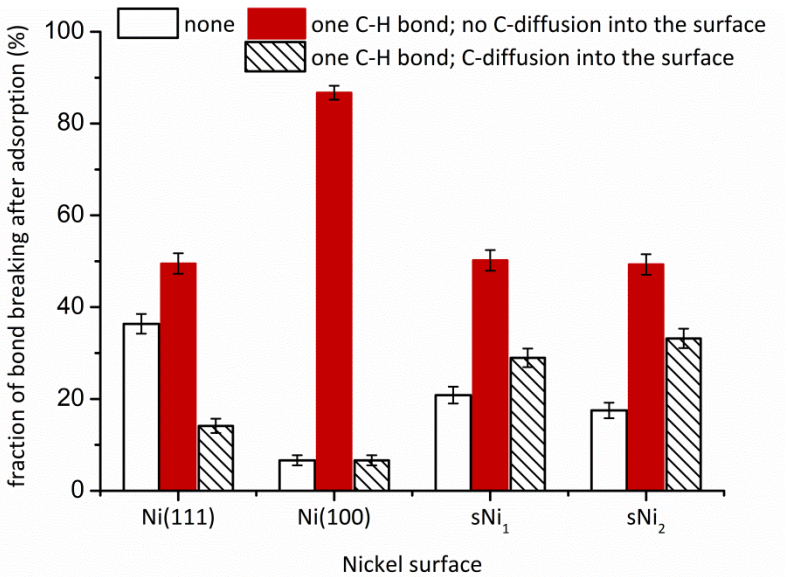


**Figure 3.5:** Observed C-H bond breaking and the associated standard deviations after adsorption of CH on the four different nickel surfaces.

Similar to the $CH_2$ radicals, the adsorption probabilities of the CH radicals only have a small influence on the difference in the overall reactivity because of their similar values. Ni(100) is thus the most reactive surface, with a C-H bond cleavage for 93% of the impacting CH radicals.

### 3.3.2. Consecutive impacts

a) Adsorption probability

The average adsorption probabilities of the radicals after the consecutive impacts (Figure 3.6) follow the previously discussed observation of the single impacts, i.e. the CH radical adsorbs the most on each surface and the $CH_3$ radicals the least. The adsorption probability after the consecutive impacts is as expected, i.e., lower than after the single impacts, since previously adsorbed molecules sterically hinder the adsorption of new incoming molecules.

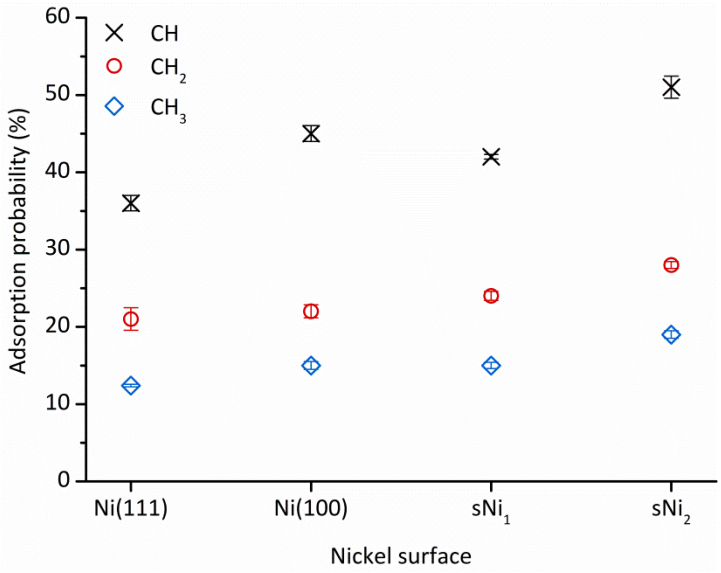


**Figure 3.6:** Adsorption probabilities and associated standard deviations for the consecutive impacts of the $CH_x$ radicals on the four different nickel surfaces.

However, in contrast to the single impacts, the largest difference between the surfaces is obtained for the CH radicals, instead of the $CH_3$ radicals, as also shown in Figures 3.7a – 3.7c. In these figures, the average number of adsorptions is shown as a function of the number of impacts per surface binding site, in order to make a proper comparison between the surfaces.

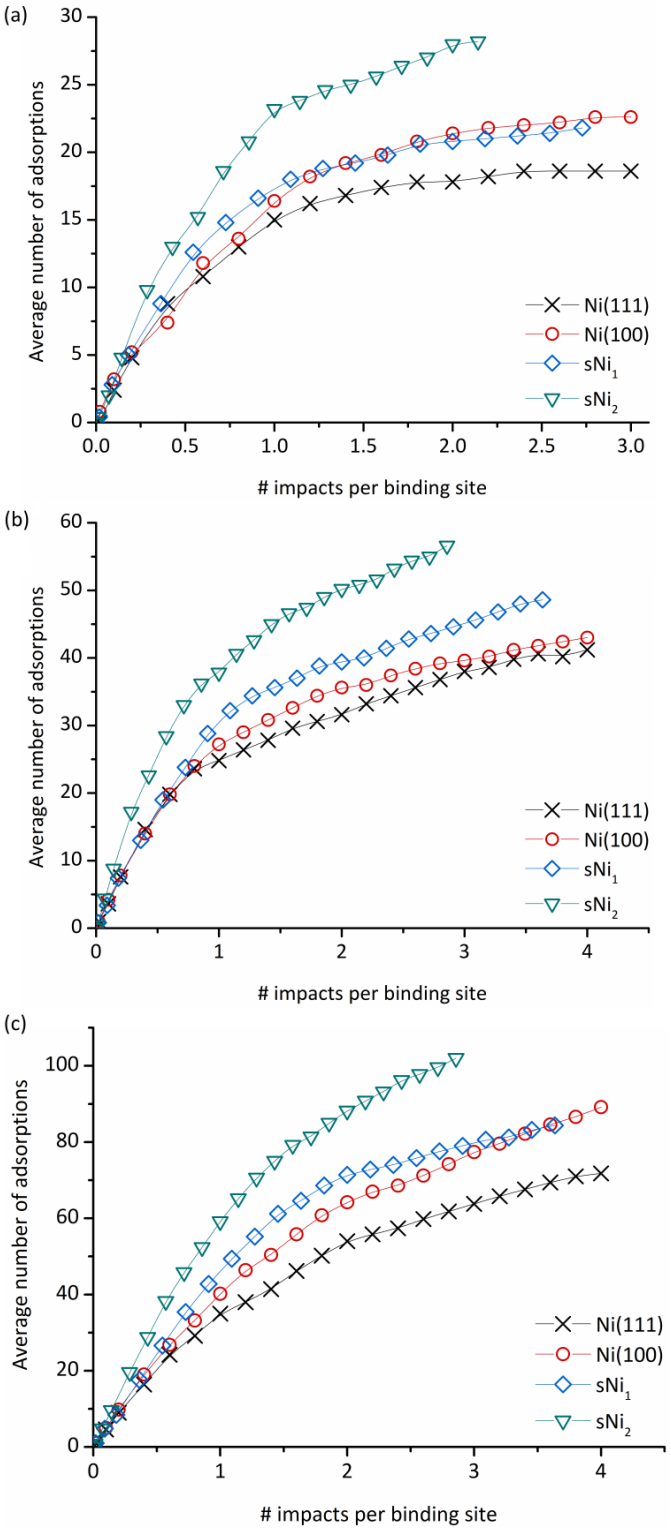


**Figure 3.7:** Average number of adsorptions of the (a) $CH_3$, (b) $CH_2$ and (c) CH radicals on the different nickel surfaces as a function of the number of impacts per binding site.

Both Ni(111) and Ni(100) have 50 binding sites, while $sNi_1$ and $sNi_2$ have, 55 and 70 binding sites, respectively. Ni(111) has the lowest adsorption probability for each radical after the same number of impacts per binding site. On Ni(100) and $sNi_1$, $CH_3$ adsorption increases by 22 % compared to Ni(111), which corresponds to 4 additional adsorptions after the same number of $CH_3$ impacts per binding site. The difference between $sNi_1$ and Ni(111) for the adsorbed $CH_2$ radicals is similar, with an increase in adsorptions of maximum 17 % on $sNi_1$, i.e., 7 additional $CH_2$ adsorptions on $sNi_1$. For the CH impacts, the number of adsorptions on Ni(100) and $sNi_1$ maximally increase by 24 %, i.e., 17 additional adsorptions, compared to Ni(111). A part of these additional adsorptions are due to diffusion of C-atoms into the structure, which makes some binding sites available again. This occurs the most on the stepped surfaces, just as after the single impacts (cf. Figure 3.5). In contrast to the single impacts, the fraction of C-atoms that diffuse into the structure is higher for Ni(100) than for Ni(111), hence the higher number of adsorptions on Ni(100).

There are always more radicals adsorbed on $sNi_2$ than on the other surfaces after the same number of impacts per binding site. Clearly, this is due to the higher number of binding sites on $sNi_2$. Indeed, the number of binding sites on $sNi_2$ is 1.4 times higher than on Ni(111) and Ni(100) and 1.27 times higher than on $sNi_1$, while the average number of adsorptions after the same number of impacts per binding site is 1.2 to 1.6 times higher on $sNi_2$ compared to the other surfaces.

In Figures 3.7a – 3.7c, two stages can be distinguished, the most obvious in the last two figures. In the first stage, the average number of adsorptions per binding site increases at the same rate for all surfaces, and thus the number of adsorbed radicals is similar for each surface. In the second stage, differences in the adsorption numbers arise between the surfaces, which are maintained for the remaining impacts. The start of the second stage is not so clear for the $CH_3$ impacts. After 0.2 impacts per binding site the first small difference between the surfaces is observed. This difference then increases during the

following impacts before remaining stable. The start of the second stage for the $CH_2$ and CH impacts is more obvious and nearly coincides for both cases, namely after about 0.7 impacts per binding site. At this moment, a large part of the surface area is covered by the adsorbed radicals. The adsorption probability of new impinging radicals is then influenced by the reactions at the surface, including the diffusion into it. As mentioned before, the C-diffusion into the surface is higher for Ni(100) and the stepped surfaces, hence the higher number of adsorptions for these surfaces.

b) Reactions after adsorption

The results of the single impacts illustrated the low reactivity of the $CH_3$ radicals, which is also observed for the consecutive impacts (Figure 3.8). The number of broken C-H bonds remains low, with comparable values for the different surfaces.

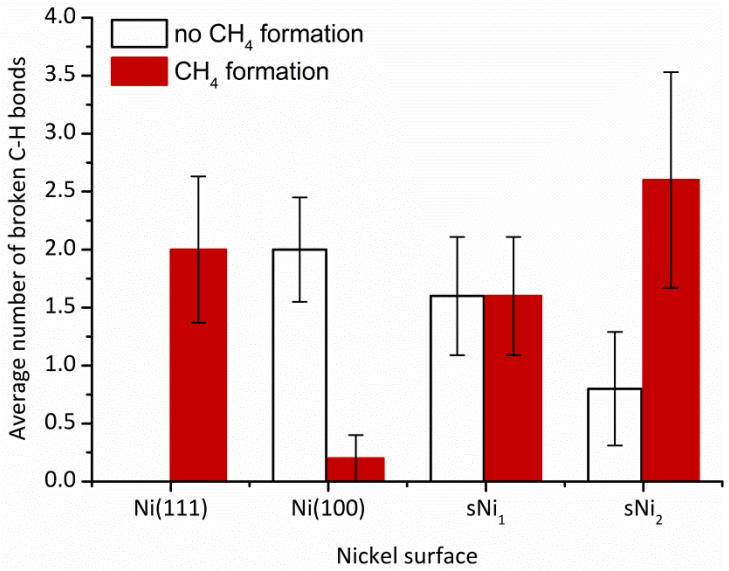


**Figure 3.8:** Average number of broken C-H bonds, sometimes followed by $CH_4$ formation, and the associated standard deviations of the adsorbed $CH_3$ radicals on the different nickel surfaces after 150 consecutive impacts.

Interestingly, however, the mechanism for this bond breaking process is found to be dependent on the surface morphology. On Ni(111), a C-H bond of an adsorbed radical is only broken if the hydrogen atom involved is subtracted by

an incoming radical, forming a volatile $CH_4$ molecule. This mechanism rarely occurs on Ni(100), on which the C-H bond simply breaks without interacting with another incoming radical. On the two stepped structures, both mechanisms are observed.

During the consecutive impacts of $CH_2$ and CH radicals, a wider range of molecules is formed in comparison to the $CH_3$ impacts. After 200 $CH_2$ impacts, incoming radicals have recombined to form $CH_3$ or even $CH_4$, but also $C_2H_4$ and $C_2H_6$ are formed (see Figure 3.9). The $H_2$ formation as observed in the single impact simulations still occurs on Ni(100) and the stepped surfaces, but it is not increased and is almost negligible.

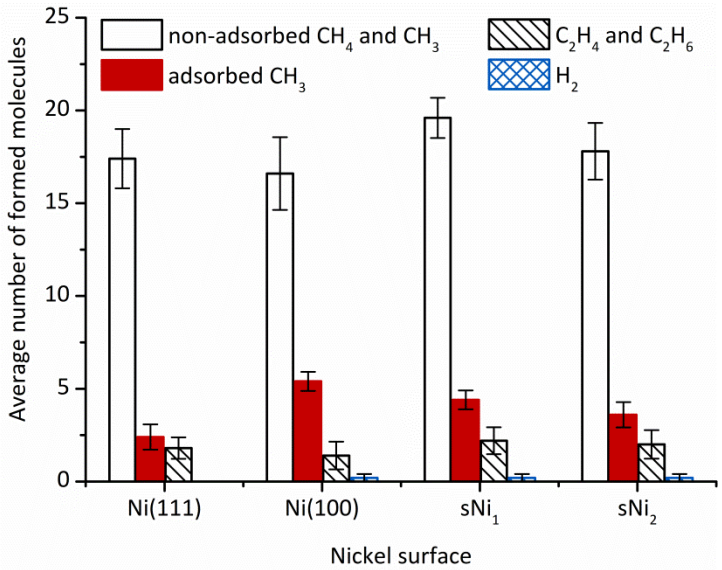


**Figure 3.9:** Average number of formed molecules and the associated standard deviations after 200 consecutive $CH_2$ impacts on the different nickel surfaces.

The four surfaces show similar results, although there are two important differences:

1. There is a difference in the possible mechanisms for the formation of $CH_3$ and $CH_4$ between the Ni(100) and the (111) surfaces. On the (111) surfaces, these molecules are formed by subtraction of the H-atom(s) of the C-H bond(s) of adsorbed molecules by incoming radicals. The C-

H bonds of the adsorbed molecules can also be broken without interaction with incoming radicals, resulting in an adsorbed H-atom on the surface. However, the adsorbed H-atoms on the (111) surfaces do not react further, and simply remain adsorbed as single atoms (see Figure 3.10). This leaves only one mechanism for the $CH_3$ and $CH_4$ formation. On Ni(100), $CH_3$ and $CH_4$ are also formed by subtraction of the H-atom(s) of the C-H bond(s) of adsorbed molecules by incoming radicals. Furthermore, they can also be formed when the H-atoms adsorbed on the surface are subtracted by incoming radicals. This is illustrated in Figure 3.10, in which the number of adsorbed H-atoms on Ni(100) decreases as the impacts continue. Thus, on Ni(100) there are two mechanisms for forming $CH_3$ and $CH_4$.

2. The presence of surface steps slightly increases the reactivity towards the formation of new molecules, as shown by comparing the results between Ni(111) and $sNi_1$/$sNi_2$ in Figure 3.9.

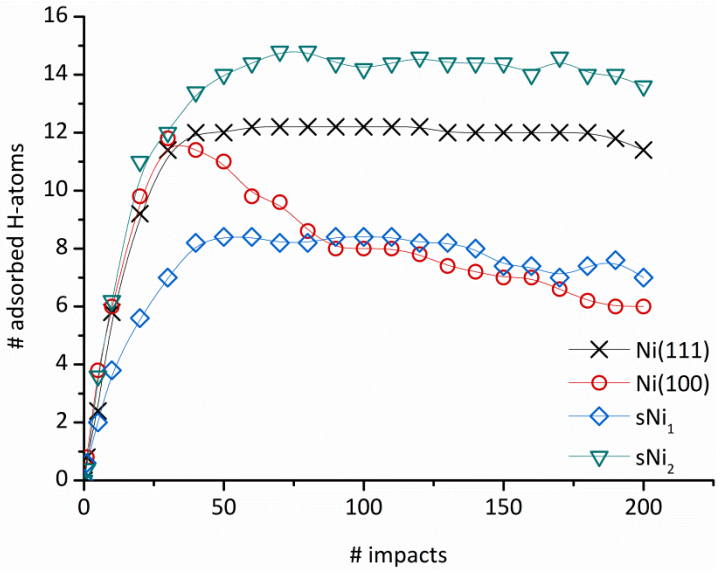


**Figure 3.10:** Average number of H-atoms adsorbed on the different nickel surfaces as a function of the number of $CH_2$ impacts.

After 200 consecutive CH impacts, a wide variety of non-adsorbed species is formed, i.e. $CH_4$, $CH_3$, $CH_2$, $H_2$ and $C_2H_x$ (x={1,2,3}), as shown in Figure 3.11. Furthermore, adsorbed $CH_3$ and $CH_2$ radicals are also observed. In comparison

to the single impacts, some $H_2$ formation is observed, though the yield is small. The resulting surface after 200 consecutive CH impacts on Ni(111) is shown in Figure 3.12, illustrating the reactivity and complexity on the surface.

Again, the results between the different surfaces are similar, although some differences compared to the $CH_2$ impacts are observed. To form the above mentioned species, incoming radicals can subtract either a H-atom from an adsorbed radical, as well as a H-atom adsorbed as an atom on the surface. This occurs on all the surfaces, in contrast to the corresponding formation process after $CH_2$ impacts, in which case this process is only observed on the Ni(100) surface. Furthermore, the influence of the steps is smaller compared to the $CH_2$ impacts. While the steps induce $H_2$ formation, the $C_2H_x$ formation stays the same.

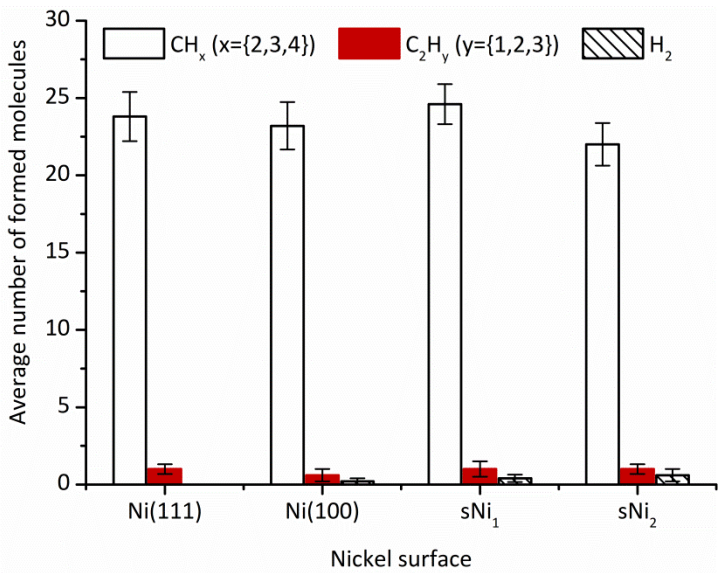


**Figure 3.11:** Average number of formed non-adsorbed molecules and the associated standard deviations after 200 consecutive CH impacts on the different nickel surfaces.

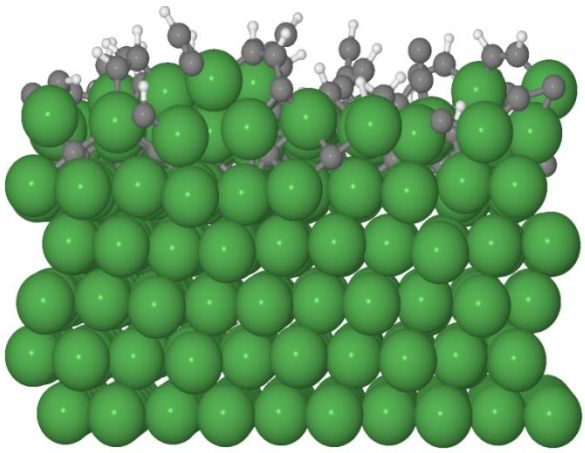

**Figure 3.12:** Side view of the Ni(111) surface after 200 consecutive CH impacts, illustrating the complexity of the system.

### 3.3.3. Comparison between $sNi_1$ and $sNi_2$

While the influence of steps on the surface is clearly illustrated in the two previous sections, the size of these steps seems to have little effect. Especially in the case of the single impacts, the difference between both stepped surfaces is minimal for the adsorption probability, the occupied adsorption sites and the reactions after adsorption. Even when the reactivity becomes more complex with the consecutive impacts, the results on $sNi_1$ and $sNi_2$ remain similar. We can thus conclude that the size of the steps used in this study only has a small influence, and for this reason, we did not include $sNi_2$ in our further studies.

A cautionary remark is that various defects or step-edges can be present on a nickel surface, so other types of surfaces than $sNi_1$ and $sNi_2$ can be formed. This might give rise to larger variations in reactivity. However, it is difficult to estimate the extent of this effect and it would be more a trial-and-error based method to find the most reactive step-edged structure. Because of this, the emphasis of this work is kept on determining the difference in reactivity between flat surfaces with a different orientation and only one stepped surface, namely $sNi_1$.

## 3.4. Conclusion

The interaction of $CH_x$ (x={1,2,3}) plasma species on four different nickel surfaces was investigated using reactive molecular dynamics simulations. To mimic typical plasma catalysis conditions, the temperature was set to 400 K.

It is shown that the CH radical has the highest adsorption probability on all surfaces, both for single and consecutive impacts, followed by $CH_2$ and $CH_3$. This decrease in reactivity in the series CH – $CH_2$ – $CH_3$ can be explained by the decreasing number of free radical electrons and the increasing steric hindrance.

For the single impacts, the differences between the nickel surfaces is the most significant for $CH_3$, for which the adsorption probability on Ni(100) and the two step-edged structures is higher than on Ni(111). This results from the increased geometric cross section of the surface nickel atoms of Ni(100) and the two step-edged structures compared to Ni(111), and therefore the higher surface reaction cross section.

Furthermore, the breaking of some C-H bonds is observed after adsorption, especially for the $CH_2$ and CH radicals. In most cases, only one C-H bond is broken and the hydrogen atom remains on the nickel surface after the bond cleavage. Only for a small fraction of the adsorbed $CH_2$ radicals, both C-H bonds break. This is followed by either $H_2$ formation or diffusion of the hydrogen atoms over the surface. The diffusion of the carbon atom into the surface occurs only for adsorbed CH radicals, and predominantly on step-edged structures.

For the consecutive impacts, the largest differences in adsorption probability on the various surfaces are observed for the CH radicals. On Ni(100) and the stepped structures, there is more diffusion of adsorbed carbon atoms into the surface, which increases the adsorption probability. During the consecutive impacts, two stages are detected. In the first stage, the average number of

adsorptions as a function of the impacts per binding site increases at the same rate for all the surfaces. Afterwards, in the second stage, differences in adsorption rates arise between the surfaces, which are maintained for the remaining impacts.

The reactivity during the consecutive impacts is high for CH and $CH_2$ on all surfaces. Different mechanisms are observed during the $CH_2$ impacts, i.e. the adsorbed H-atoms on Ni(100) are included in the reaction mechanisms, whereas the H-atoms adsorbed on the Ni(111) structures are not. The presence of steps in a structure leads to additional C-H bond breaking after $CH_3$ impacts and a slight increase in $C_2H_4$, $C_2H_6$ and $H_2$ formation after $CH_2$ impacts. After CH impacts, the steps induce $H_2$ formation, but the effect is smaller compared to the $CH_2$ impacts.

There is no clear effect of the size of the steps. The results for $sNi_1$ and $sNi_2$ are very similar, and therefore $sNi_2$ is not included in our further studies.

The findings of this chapter can be summarized as follows:

- Adsorption probability:
  - CH > $CH_2$ > $CH_3$
  - Determined by the number of free electrons of the radical and the steric hindrance caused by the H-atom(s)
- Reactions after adsorption:
  - Limited for $CH_3$
  - High for $CH_2$ and CH
- Influence of the nickel surface structure:
  - Slightly increased reactivity of adsorbed $CH_3$ on Ni(100), $sNi_1$ and $sNi_2$
  - Different mechanisms for $CH_3$ and $CH_4$ formation after $CH_2$ impacts on Ni(100) compared to the other surfaces

The results of these reactive MD simulations are in agreement with previous studies, and give additional information concerning the interactions of the $CH_x$ radicals on the nickel surfaces. This demonstrates that this type of MD simulations can be a useful tool to study the interaction of plasma species on nickel surfaces, and eventually, help to improve the insight in complex reaction systems, such as plasma catalysis.

# Chapter 4:
# Temperature influence on the reactivity of $CH_x$ radicals on Ni(111)

In this chapter, the influence of the surface temperature on the reaction behavior of $CH_x$ radicals on a Ni(111) surface is investigated. The emphasis in this chapter lies on $H_2$ formation, in a temperature range of 400 – 1600 K. These simulations are carried out with the Bussi thermostat, instead of the combination of the NVE ensemble and the Berendsen thermostat which was used in the previous chapter. Because of this, the use of the Bussi thermostat is first validated, before turning to the actual temperature study.

It is shown that while some $H_2$ formation is already observed at lower temperatures, substantial $H_2$ formation is only obtained at elevated temperatures of 1400 K and above. At 1600 K, the $H_2$ molecules are even the most frequently formed molecules. In direct correlation with the increasing dehydrogenation at elevated temperatures, an increased surface-to-subsurface C-diffusivity is observed as well.

---

This chapter is based on the following publication: W. Somers, A. Bogaerts, A.C.T. van Duin, S. Huygh, K.M. Bal and E.C. Neyts, Temperature influence on the reactivity of plasma species on a nickel catalyst surface: an atomic scale study, Catal. Today 211 (2013) 131-136.

## 4.1. Introduction

As indicated in the previous chapter, some $H_2$ molecules are formed after $CH_x$ impacts on the various nickel surfaces, although the fraction at a temperature of 400 K is very small. However, it can be expected that the probability of $H_2$ formation increases at higher temperature, which has been suggested before [92]. Therefore, in this chapter, the temperature is increased to the region of the so-called warm plasmas [42,141,142], i.e. 1000-2000 K, in order to determine the temperature onset for $H_2$ formation.

In the first part of this chapter, we compare the results of consecutive $CH_x$ impacts at 400 K on Ni(111) employing the Bussi thermostat [116] and the Berendsen thermostat [115], in order to verify the equivalence of both methods to study this system. The Bussi thermostat is, in contrast to the Berendsen thermostat, capable to correctly generate the canonical ensemble. We specifically verify the equivalence of both thermostats, in order to demonstrate the validity of the comparison between the results obtained in this chapter and in the previous chapter. In the second part, consecutive $CH_x$ impacts are performed in a temperature range from 800 to 1600 K, again on the Ni(111) surface, with the focus on $H_2$ formation. The maximum temperature of 1600 K is chosen because Mueller et al. observed significant melting of the nickel surface in ReaxFF above 1800 K [93]. This is in agreement with the ambient melting temperature of nickel, i.e., 1728 K [143].

## 4.2. Description of the simulations

In this chapter, only consecutive impacts are performed, instead of both single and consecutive impacts. The setup of these impacts is very similar to the one used in Chapter 3. The difference is, as stated above, the use of the Bussi thermostat as an alternative for the combination of the NVE ensemble and the Berendsen thermostat.

Prior to the consecutive impacts, the Ni(111) surface is first equilibrated at the desired temperature using the Bussi thermostat with a coupling constant of 100 fs, in the range 400 K – 1600 K, with a 200 K interval. Again, periodic boundary conditions are applied in the {x,y} directions, in order to simulate a semi-infinite surface.

The impacting $CH_x$ radicals (x={1,2,3}) are added to the system at a *z* position of 10 Å above the top layer of the nickel surface. The initial {x,y} coordinates are randomized. The magnitude of the initial velocity vector is set to the root-mean-square velocity corresponding to the substrate temperature, i.e., 400 K – 1600 K. Each impact is followed for 6.25 ps, in which the radicals can be adsorbed, decomposed or reflected. In the case of reflection, the radicals are removed from the system. The resulting surface is subsequently used as the input configuration for the next impact. This sequence is repeated 150 times for the $CH_3$ impacts, and 250 times for the $CH_2$ and CH impacts. The larger number of simulated $CH_2$ and CH impacts compared to the previous chapter, i.e. 200 impacts, is due to a higher reactivity at elevated temperatures. After this number of impacts, clear trends in the reactivity after impact are observed. For each case, i.e., the sequence of impacts of each radical at the six different temperatures, three different simulations are performed and the results reported here are the averages over these three simulations with the associated standard deviations. Thus, in total, 54 simulations are carried out, accounting for a total of 11700 impacts.

It is essential to keep in mind that these simulations approach the effect of plasma on a catalyst only through the reactivity of the radicals. Experimentally, this increases the concentration of active species near the catalyst surface and may enhance the energy efficiency. It is also important to realize, however, that not all possible effects of plasma on the catalyst can be described in these simulations. For instance, the influence of electrons, and therefore the electron density, on carbon deposition through direct electron impact dissociation of methane cannot be taken into account in our simulations. This process would effectively and drastically reduce the catalytic

activity. However, note that the electron density of the transitional regime of a gliding arc discharge is $10^{12}$ $cm^{-3}$, while the value in a DBD is typically less than $10^{20}$ $cm^{-3}$ [41,42]. Furthermore, in the transitional regime of a gliding arc discharge $T_e \approx 1$ eV, which is a characteristic value for non-thermal plasmas. Since the electron energy is comparable for DBD and gliding arc discharges (in the transitional regime), and the electron density is lower for the latter discharge, we expect that the temperature will have the most substantial influence on a process such as carbon deposition.

Additionally, the plasma might alter the reactivity of the catalyst by changing the crystallinity. As discussed in Chapter 3, the type of nickel surface indeed influences the reactivity after impacts of plasma species. For this purpose, the next chapter will further focus on the reactivity on several nickel surfaces, ranging from polycrystalline to amorphous structures.

## 4.3. Results and Discussion

### 4.3.1. Comparison of the Berendsen and Bussi thermostat

Both the adsorption probability and the reactions after adsorption as obtained from the simulations with the Bussi thermostat are compared with the results from the previous chapter, which were obtained from simulations under the NVE ensemble in combination with the Berendsen thermostat [115].

As shown in Figure 4.1, the average adsorption probability after 150 consecutive $CH_3$ impacts is almost equal for both methods, with only a small difference of less than 0.5% between the two values. The difference between the average adsorption probabilities obtained with both methods slightly increases for the $CH_2$ impacts, i.e. up to 1%. However, when considering the standard deviations on these averages, both methods still give very similar results. Only in the case of the consecutive CH impacts, there is a noticeable

difference between the average adsorption probabilities obtained with both methods, even though it remains low (3%).

The progressing adsorption probability after each consecutive impact is determined by the reactivity of the incoming radical, i.e. the number of free radical electrons, as well as by the steric hindrance induced by the radicals that are already adsorbed on the surface. Since the reactivity of the incoming radicals does not change during the simulations, the difference between the adsorption probabilities obtained using both methods can be allocated to the different steric hindrance of the nickel surface and its adsorbed species towards the incoming radicals. As discussed in the previous chapter, the resulting nickel surface after the impacts is of a complex nature that consists of a large variety of adsorbed molecules (cf. Figure 3.12), due to the high reactivity of the CH radicals. As a consequence, there is more variance between the resulting surfaces of each complete CH impacting sequence compared to that of the $CH_3$ and $CH_2$ impacts. Keeping this in mind, we can conclude that the difference of 3% between both simulation methods is acceptable.

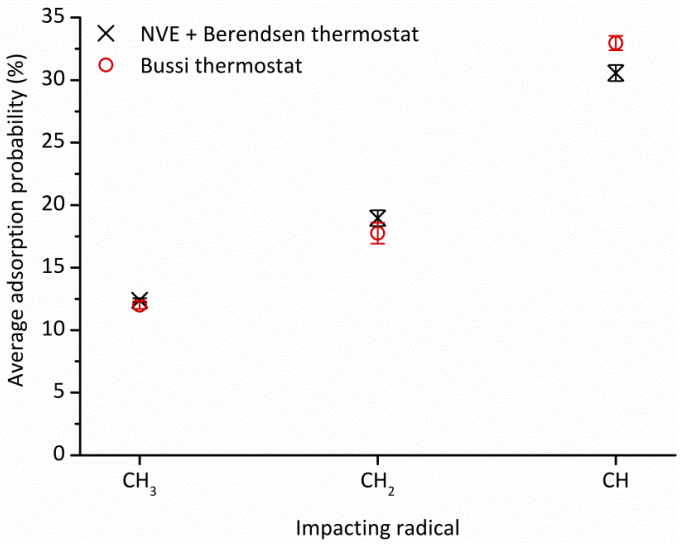


**Figure 4.1:** Comparison of the average adsorption probabilities and associated standard deviations of the $CH_x$ radicals on Ni(111) as determined from NVE simulations in combination with the Berendsen thermostat and NVT simulations employing the Bussi thermostat.

A comparison between the average numbers of formed non-adsorbed molecules can assist in further studying the accuracy of both simulation methods. The reactions after the adsorption of $CH_3$ radicals are very rare, resulting in only 2 broken C-H bonds on a total of 150 impacts for both methods. Both bond breaking events subsequently lead to the formation of a $CH_4$ molecule. In addition to the adsorption probability, the reactivity after adsorption is thus also equal for both methods.

The type of non-adsorbed molecules formed after $CH_2$ and CH impacts is the same for the simulations with the Berendsen and Bussi thermostat, as shown in Figures 4.2 and 4.3. Especially for the formation of $CH_4$ and $CH_3$ molecules, the differences are very small. Even for the formation of $CH_2$ radicals after the CH impacts, there is only a limited influence of the thermostat.

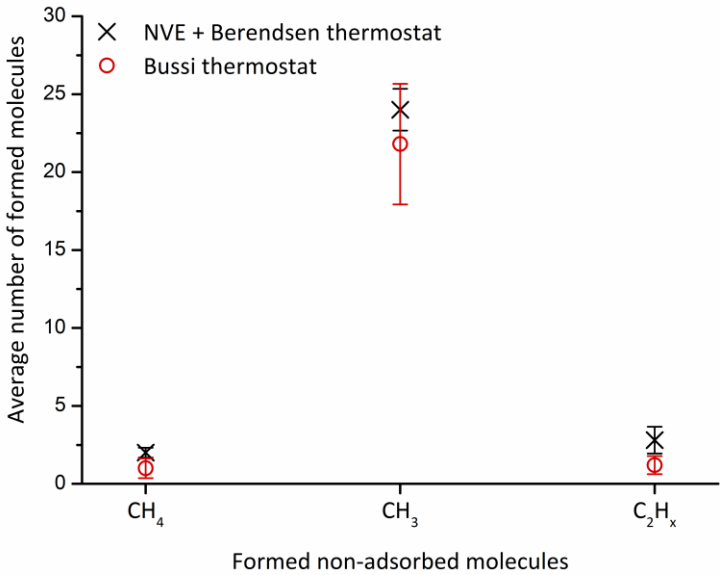


**Figure 4.2:** Comparison between the average number of formed non-adsorbed molecules and associated standard deviations, after 250 consecutive $CH_2$ impacts.

These results show that although the simulated ensemble is different, the use of the Bussi thermostat and the Berendsen thermostat in combination with NVE simulations result in the same reactivity of small hydrocarbons on a Ni(111) surface. Therefore, the use of the canonical Bussi thermostat for the temperature study is validated.

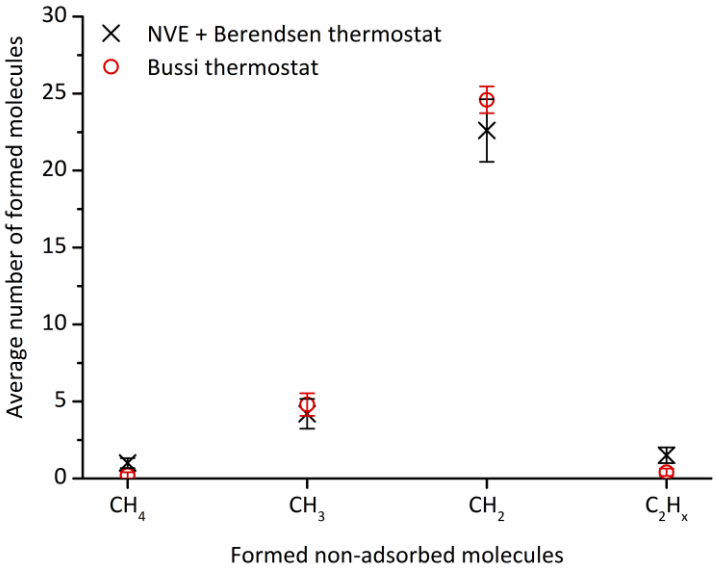


**Figure 4.3:** Comparison between the average number of formed non-adsorbed molecules and associated standard deviations, after 250 consecutive CH impacts

### 4.3.2. Temperature effect

a) $H_2$ formation

It is important to point out that in our previous simulations, at a temperature of 400 K, no $H_2$ formation was observed after consecutive $CH_x$ impacts on Ni(111). On the other nickel surfaces, only a small amount of $H_2$ was formed at the same temperature. So it is essential to know if $H_2$ formation can occur after $CH_x$ impacts on Ni(111), and, if so, what the threshold temperature of this reaction is.

*$CH_3$ impacts*

After 150 consecutive $CH_3$ impacts on Ni(111), no $H_2$ formation is observed up to a temperature of 1200 K (see Figure 4.4). It has been demonstrated by Mueller [92] that adsorbed $CH_3$ is kinetically stable on Ni(111) at low temperatures, and that higher temperatures are required to overcome the barrier for C-H bond breaking (0.80 eV). This is also observed in our simulations, where the number of broken C-H bonds, and thus the number of formed $CH_4$ molecules is increasing as a function of temperature. This implies

that the impacting radicals have enough energy to abstract a H-atom from the adsorbed molecules or from the nickel surface. However, the recombination of two hydrogen atoms to form $H_2$ requires much energy. Our simulation results indicate that a temperature of 1400 K is required to overcome this barrier, with an average of 2 $H_2$ molecules formed on a total of 150 impacts. The $H_2$ formation further increases to nearly 6 molecules on a total of 150 impacts, when increasing the temperature to 1600 K. This means that 4% of the $CH_3$ impacts are followed by $H_2$ formation. Additionally, there is a decrease in the number of formed $CH_4$ molecules, since the H-atoms adsorbed on the nickel surface now recombine into $H_2$.

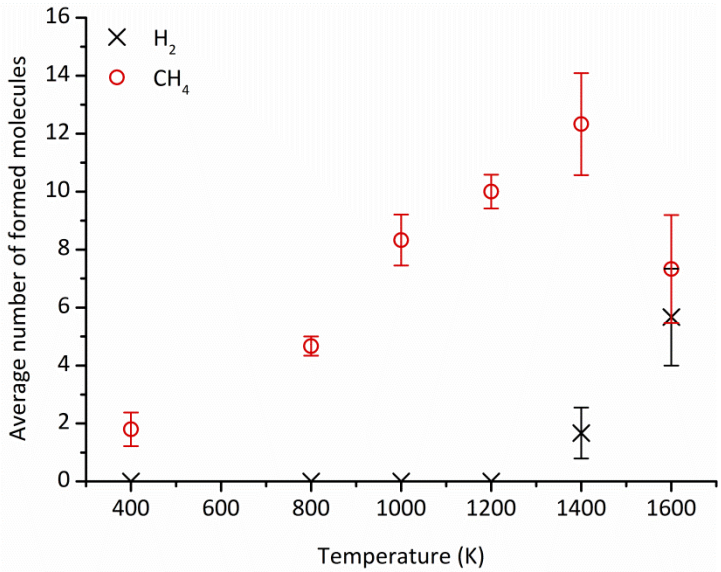


**Figure 4.4:** Average number of formed molecules, and associated standard deviations, as a function of temperature after 150 consecutive $CH_3$ impacts.

*$CH_2$ impacts*

Even at 400 K, the reactivity of $CH_2$ and CH is found to be much higher than the $CH_3$ reactivity, giving rise to formation of $CH_4$, reflected $CH_3$ and $CH_2$, and a small fraction of $C_2$ species. The molecules formed after 250 consecutive $CH_2$ and CH impacts can be divided into 3 groups: $H_2$, $CH_x$ and $C_2H_x$ molecules. As illustrated in Figure 4.5, a small number of $H_2$ molecules is formed at 800 K, 1000 K and 1200 K upon the $CH_2$ impacts. However, this number increases significantly at temperatures of 1400 K and 1600 K, with up to 41 $H_2$

molecules for the latter temperature. Thus, at 1600 K, 16% of the $CH_2$ impacts are followed by $H_2$ formation. This is even higher than the number of $CH_x$ molecules formed, in contrast to the results at lower temperatures, where the number of $CH_x$ molecules is larger than that of $H_2$. Furthermore, this result is in agreement with previous research on thermal methane cracking [144], where a temperature of more than 1600 K was needed to generate $H_2$ as the main component of the evolving gas.

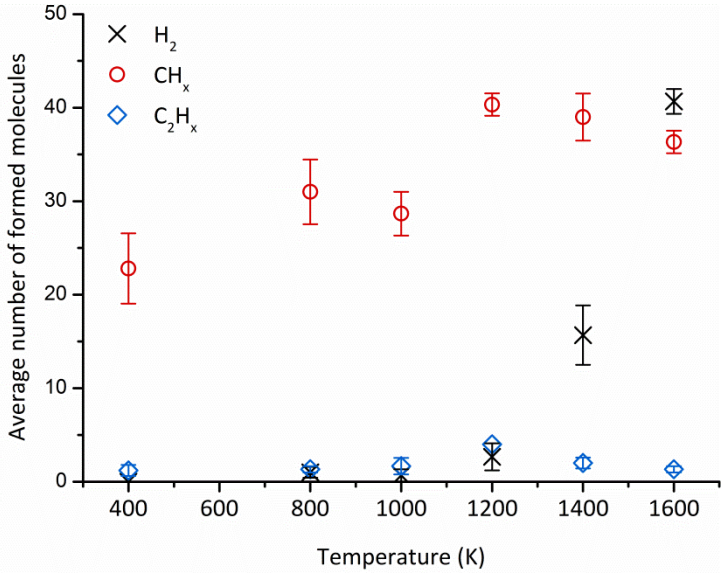


**Figure 4.5:** Average number of formed molecules, and associated standard deviations, as a function of temperature after 250 consecutive $CH_2$ impacts.

At temperatures up to 1200 K, most of the surface-bound H-atoms react with the impacting radicals to form $CH_x$ molecules. In some rare occasions, the H-atoms have enough energy to recombine into $H_2$. As is also the case for the $CH_3$ impacts, this process is activated at a temperature of 1400 K, and at even higher temperatures most H-atoms are found to recombine, thus causing a reduction in the number of formed $CH_x$ molecules. The energy barrier for the recombination of 2 H-atoms to $H_2$ is calculated with the nudged elastic band (NEB) method [145], and is found to be 1.66 eV. This is higher than the calculated barrier for H-diffusion over the nickel surface, which we calculated as 0.35 eV. The increase in temperature is thus essential for crossing the energy barrier for $H_2$ formation.

It is important to notice that the value of 1.66 eV should be used with caution. This value is of the same order as the one obtained with a DFT based study, i.e. 1.4 eV [146]. However, experimental values are considerably lower, i.e. between 0.5 eV and 0.9 eV [147,148]. The energy barrier for recombination of 2 H-atoms to $H_2$ is thus overestimated in our simulations. This value can still be used to make comparisons with other energy barriers in the same simulation setup, but a comparison with experiments or other simulations should be avoided.

In addition to the $CH_x$ and $H_2$ molecules, some $C_2H_x$ molecules are also formed, although their formation is hardly influenced by the temperature.

*CH impacts*

The $H_2$ formation due to CH impacts (Figure 4.6) is initiated at 800 K. As is the case for the $CH_2$ impacts, a significant increase in the $H_2$ formation is observed at temperatures of 1400 K and 1600 K. Furthermore, the trend concerning the number of $CH_x$ molecules formed as a function of the temperature is maintained. Indeed, at lower temperatures, the $CH_x$ molecules are the most occurring particles, while at 1600 K, the $H_2$ molecules are most dominantly formed. At this temperature, 12% of the CH impacts are followed by $H_2$ formation, corresponding to an average of 30 $H_2$ molecules formed after 250 consecutive impacts. This is lower than the number of $H_2$ molecules formed due to $CH_2$ impacts, as can be expected since there are less H-atoms in the CH-system.

The stability of H-atoms on Ni(111) has been investigated by Mueller [92]. It was found that at low temperatures, most hydrogen atoms are adsorbed on the surface. However, at higher temperatures the adsorbed H-atoms tend to recombine to $H_2$, as is the case in our simulations. In contrast to the results of the $CH_2$ impacts, the $C_2H_x$ formation is slightly dependent on the temperature, although the $C_2H_x$ fraction remains small. Furthermore, the ionization energy of these molecules is lower than that of $CH_x$ molecules, i.e. 11.56 eV for $C_2H_6$

versus 12.98 eV for $CH_4$ [22,149]. This implies that, in a plasma catalytic process, the $C_2H_x$ molecules are more likely to decompose in the plasma after they are formed at the catalyst surface than the more stable $CH_x$ molecules. The easier decomposition of these molecules in a plasma, as a function of residence time, has already been demonstrated in literature [150].

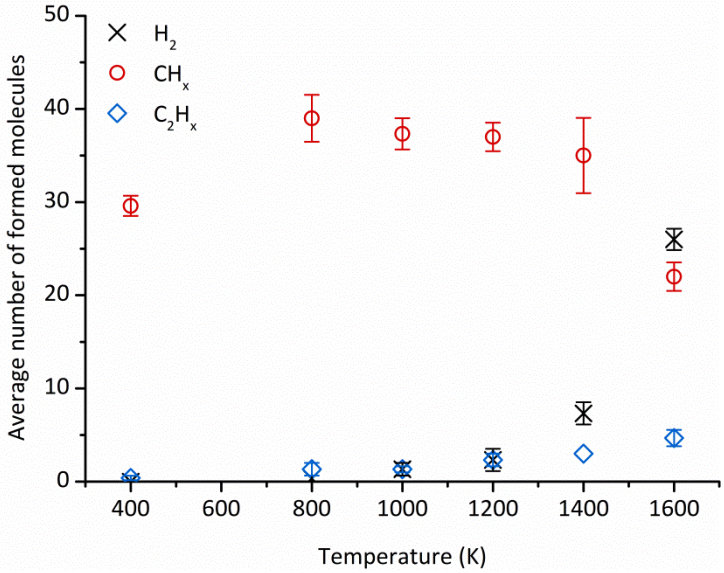


**Figure 4.6:** Average number of formed molecules, and associated standard deviations, as a function of temperature after 250 consecutive CH impacts.

Under experimental conditions corresponding to the simulation results, the $H_2$ formation occurs at temperatures that may lead to sintering of the catalyst. This increases the size of the nickel particles, and decreases the activity due to the reduced catalytic surface area [29]. It should be noted that in our simulations, sintering and thus this loss of catalytic surface area is not included, since we study the interactions on a semi-infinite surface. It is thus important to remark that while the total catalytic surface area may indeed be reduced at these temperatures (i.e., in the order of 1400 K), the simulated substantial $H_2$ formation corresponds to highly localized small-area surface patches.

As a final remark, the simulation time scale is also of importance. Longer simulations will almost certainly lead to enhanced $H_2$ formation, even at

temperatures lower than 1400 K. Extension of the typical nanosecond time scale of MD simulations is an essential step in improving the applicability of this simulation method. However, the trends obtained in the current simulations still give valuable information, i.e. the temperature influence is clearly observed.

b) Carbon diffusion into the nickel surface

The results discussed above indicate the positive effect of increasing the temperature on the $H_2$ formation. However, the temperature also influences the diffusion of carbon atoms into the nickel surface, which is not a desired effect. Indeed, in the steam methane reforming process, carbon deposition can reduce the performance of the catalyst, for example by blocking the active sites of the catalyst. As mentioned above, the reactivity in the case of the $CH_3$ impacts is rather low, especially when comparing these results with the reactivity of the other impacting radicals. Only a few $CH_3$ radicals become fully dehydrogenated after adsorption, and consequently, the resulting C-atoms can diffuse into the nickel surface. Up to 1400 K, the C-atoms only diffuse into the first subsurface layer, but at a temperature of 1600 K, the diffusion goes deeper into the nickel structure, i.e., until the third subsurface layer.

The same effect is also observed for the dehydrogenated C-atoms originating from $CH_2$ and CH impacts. Little diffusion, i.e., in the range of 16 diffused C-atoms on a total of 250 $CH_2$ impacts, is observed up to temperatures of 1000 K, while more extensive diffusion, i.e., in the range of 91 diffused C-atoms, occurs at a temperature of 1600 K. Since many C-H bonds are broken to form $H_2$, the number of dehydrogenated C-atoms is much larger than in the case of $CH_3$ impacts, where 24 C-atoms diffused into the nickel surface after 150 $CH_3$ impacts. Figure 4.7 illustrates the carbon diffusion into the nickel surface for $CH_2$ impacts at various temperatures. It is observed that the C-atoms only diffuse to the first subsurface layer up to a temperature of 1000 K. At higher temperatures, the C-atoms reach lower-lying Ni-layers, even the lowest layer.

As mentioned before (cf. §2.4.), the Ni-atoms in the lowest layer are fixed, to prevent the entire nickel surface from moving in the *z* direction. Because of these fixed positions, further diffusion of C-atoms through the lowest layer is less likely to occur. It is shown in Figure 4.7 that a large number of C-atoms already reached the lowest layer. It is expected that, if the nickel surface would be thicker, the C-atoms will even diffuse further into the surface.

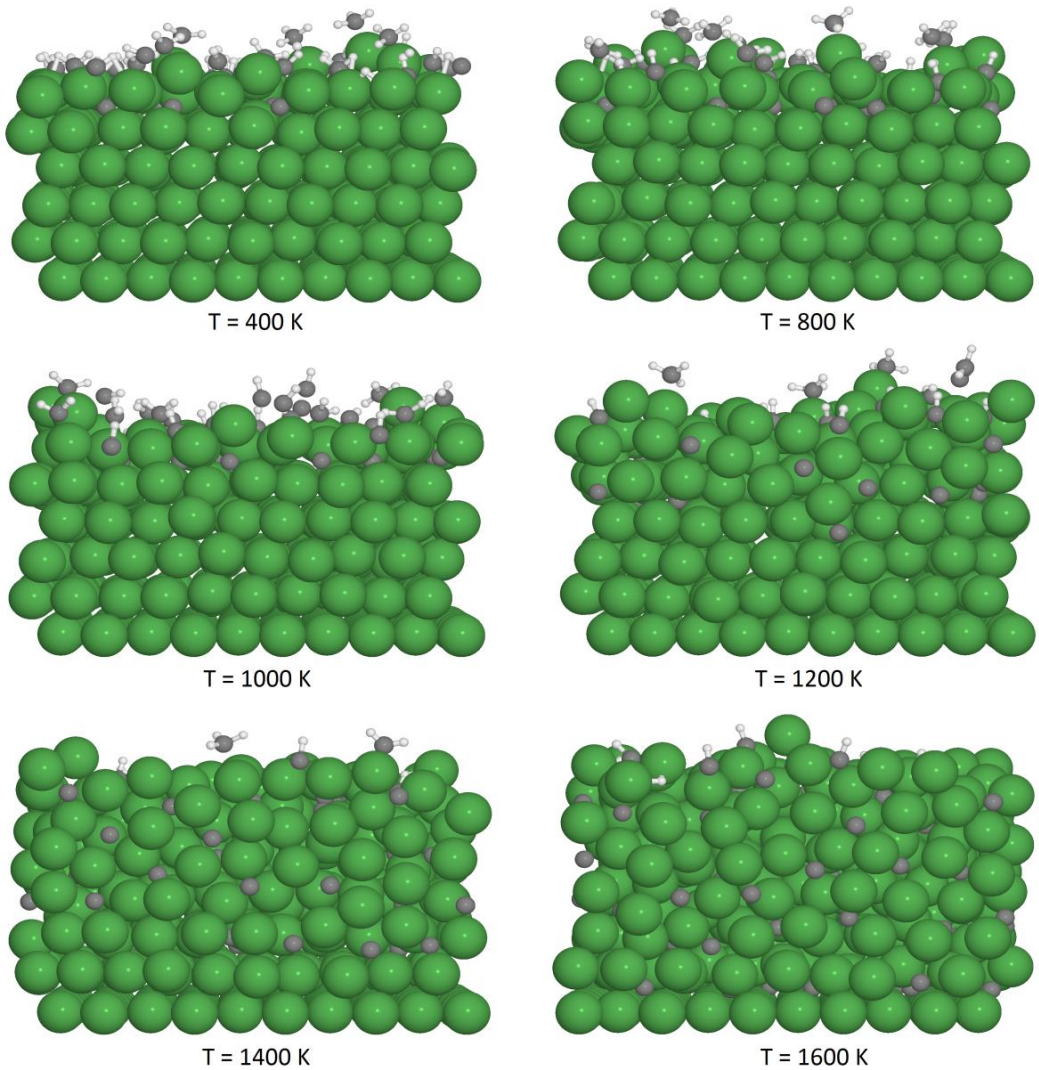


**Figure 4.7:** Side view of the Ni(111) surface after 250 consecutive $CH_2$ impacts at different temperatures.

The same temperature effect on the diffusion is observed after the CH impacts, indicating that the C-atoms gain enough energy to diffuse to lower layers at temperatures above 1000 K. The energy barrier for the diffusion of a C-atom from the $\mu_3$ hcp site to an octahedral site in the first subsurface layer is calculated with the NEB method, and is found to be 1.16 eV. This is significantly lower than the energy required for further diffusion into the surface. For instance, the diffusion from an octahedral site in the first subsurface layer to a tetrahedral site in the second subsurface layer requires 2.76 eV. The same type of diffusion from the third to the fourth subsurface layer also needs a similar amount of energy, namely 2.26 eV. Thus, as observed in Figure 4.7, high temperatures are required to overcome the energy barrier of diffusion to lower subsurface layers. The diffusion pathways of C-atoms on a Ni(111) surface have been extensively investigated by Abild-Pedersen [151]. It was found that for the diffusion of a C-atom from the top layer of a clean surface to the first subsurface, an energy of about 1.00 eV was needed, which is in agreement with our findings.

The results discussed above show that an optimal operating condition is at a temperature around 1400 K, since at higher temperatures, the diffusion of C-atoms into the nickel surface becomes too dominant, and at lower temperatures the $H_2$ formation is limited. A similar general conclusion was reached by Nikoo et al. [152]. These authors concluded that a high temperature (> 1173 K) was required for the optimal production of syngas ($H_2$ + CO) during the dry reforming of methane. Furthermore, Nozaki [51] discussed the dominance of thermal reactions on the catalyst surface at temperatures exceeding 973 K. Such thermal activation is also observed in our results. Note that in these studies oxidative species were also present, such as $H_2O$ or $CO_2$, in contrast to our simulations. These species will oxidize the adsorbed C-atoms, and release them from the surface as CO. In combination with the $H_2$ formation, this is the general mechanism for syngas production during steam methane reforming.

## 4.4. Conclusion

The influence of the temperature on the reactivity of $CH_x$ radicals on a Ni(111) surface was investigated, with a specific emphasis on $H_2$ formation.

First, we compared the use of two different ensembles for the simulation of this system, viz. the microcanonical ensemble in combination with the Berendsen thermostat, and the canonical Bussi thermostat, to validate the comparison with our previous results. It is demonstrated that there are no significant differences in the results as obtained from both methods, indicating that the obtained processes and mechanisms are not sensitive to the exact temperature control method.

Second, it is shown that $H_2$ formation can occur after $CH_x$ impacts on Ni(111), and it increases with temperature. The reactivity towards $H_2$ formation is the lowest in the case of the $CH_3$ impacts. Only at a temperature of 1400 K and 1600 K, the recombination of 2 H-atoms into a $H_2$ molecule is observed. At lower temperatures, the H-atoms react with impacting $CH_3$ radicals to form $CH_4$. The same high temperatures of 1400 K and 1600 K are also required to obtain a significant amount of $H_2$ formation after $CH_2$ and CH impacts. Again, at lower temperatures, most surface-adsorbed H-atoms will react with the impacting radicals, instead of forming $H_2$. At 1600 K, about 4%, 16% and 12% of the $CH_3$, $CH_2$ and CH impacts, respectively, are followed by $H_2$ formation.

Finally, it is also illustrated, in agreement with experimental observations, that the high temperatures do not only lead to an increase in $H_2$ formation, but also promote the diffusion of C-atoms into the subsurface region of the crystal. At temperatures of 1400 K and 1600 K, the diffusion barrier to lower subsurface layers can be overcome, reducing the possibility to oxidize the adsorbed C-atoms into CO, if oxidative species are present.

Overall, the results imply that an optimal temperature for an efficient $H_2$ formation on Ni(111) should not exceed 1400 K. At higher temperatures, the

diffusion of C-atoms into the nickel surface becomes overly dominant, while at lower temperatures the $H_2$ formation is limited. The temperature of 1400 K is reached in warm plasmas, which are also characterized by the high number of reactive excited species. Therefore, a synergistic effect might be obtained, which makes it an interesting technology for the methane reforming process.

The findings of this chapter can be summarized as follows:

- Temperature < 1400 K
    - Limited $H_2$ formation
    - C-diffusion to the first subsurface layer up to 1000 K, at higher temperatures to the second subsurface layer
- Temperature ≥ 1400 K
    - $H_2$ formation becomes the dominant reaction
    - C-diffusion into the lower-lying subsurface layers

# Chapter 5:
# Temperature and surface structure influence on the $CH_x$ reactivity

In this chapter, the study on the influence of surface temperature on the reactivity is extended towards different nickel surfaces. First, we focus on the $H_2$ formation as a function of temperature and surface structure. Second, we also investigate to what extent the species adsorbed on the catalyst surface can participate in surface reactions more in general.

It is shown that substantial $H_2$ formation is obtained at 1400 K and above, while the role of the surface structure seems limited after multiple impacts. In the initial stage, the type of nickel surface does influence the C-H bond breaking efficiency of adsorbed radicals; however, the continuous carbon diffusion into the surface gradually diminishes the surface crystallinity and therefore reduces the effect of surface structure on the $H_2$ formation probability. Furthermore, it is illustrated that only on Ni(111) surfaces, the adsorbed H-atoms rarely react with incoming radicals at a temperature of 400 K. Increasing the temperature to 800 K overcomes this limitation.

---

This chapter is based on the following publication: W. Somers, A. Bogaerts, A.C.T. van Duin and E.C. Neyts, Interactions of plasma species on nickel catalysts: a reactive molecular dynamics study on the influence of temperature and surface structure, Appl. Catal. B: Environ. 154-155 (2014) 1-8.

## 5.1. Introduction

In the previous chapters, it is shown that hardly any $H_2$ is formed after $CH_x$ impacts at a temperature of 400 K, regardless the type of nickel surface on which the radicals impinge (cf. Chapter 3). Further studies on Ni(111) showed that a temperature increase towards 1400 K or higher is required for substantial formation of $H_2$ within the simulation time scale (cf. Chapter 4). However, these high temperatures also induce diffusion of C-atoms into the nickel surface, which is more desired for e.g. (plasma-)growth of carbon nanotubes [153] or graphene [154] than for a reforming reaction. It would be more interesting to obtain significant $H_2$ formation, with less carbon diffusion. In Chapter 3, it is shown that at 400 K, the surface type does influence the C-H bond breaking and the reactivity towards formation of $CH_x$ and $C_2H_x$ molecules. If this dependency between reactivity and surface type is maintained at high temperatures, this might influence the number of formed $H_2$ molecules after impacts on the different nickel surfaces. Therefore, we consider the role of the nickel surface on the $H_2$ formation and carbon diffusion at higher temperatures in this chapter.

First, the direct $H_2$ formation on the catalyst surface is investigated for five different nickel surfaces in the temperature range of 400 – 1600 K. For this, single $CH_x$ impacts are performed to obtain the C-H bond breaking probability on the nickel surfaces. These results give an indication of the number of free H-atoms on the surface that might recombine into $H_2$. In addition, consecutive $CH_x$ impacts are performed, to determine if the $H_2$ formation is directly linked to the C-H bond breaking probability, or if other factors are of importance.

Second, we investigated the extent in which adsorbed H-atoms can participate in reactions with incoming radicals or other adsorbed species and subsequently desorb from the catalyst surface.

## 5.2. Description of the simulations

A set of five different nickel structures is used in this study, namely: Ni(111), Ni(100), a step-edged Ni(111) surface (denoted as $sNi_1$), an amorphous surface (aNi) and a polycrystalline surface (pNi). The first three surfaces were already used in Chapter 3 to study the influence of surface energy and step-edges in the surface on the adsorption probability of the radicals and the reactions after adsorption. However, the crystallinity of the surface might change due to the interactions with the plasma. Consequently, this can alter the reactivity of the catalyst. For this reason, aNi and pNi are included in this study, to elucidate this effect of change in crystallinity.

Similar to the previous simulations, the surfaces are first equilibrated to the desired temperature, in the range of 400 – 1600 K, employing the Bussi thermostat with a coupling constant of 100 fs. Subsequently, both single and consecutive impacts of $CH_x$ radicals on the nickel surfaces are performed, again applying the Bussi thermostat. The results of the impacts performed in Chapter 3, i.e. by employing the Berendsen thermostat, are also used in this chapter. In the previous chapter, we illustrated that a comparison between the Bussi and Berendsen thermostat is valid.

The single impacts provide information concerning the C-H bond breaking after adsorption, while the consecutive impacts mimic a continuous hydrocarbon flux towards the surface, and describe the formation of new species as a consequence of bond breaking and recombination reactions. For both type of impacts, the same conditions as before are applied, i.e. the radicals are added to the system at a *z* position of 10 Å above the top layer of the nickel surface, with randomized initial {x,y} coordinates and velocities, and periodic boundary conditions in the {x,y} directions.

Each single impact is performed on a pristine nickel surface, for a total simulation time of 5 ps, at temperatures of 400 K, 800 K, 1200 K and 1600 K.

Within this time, the radical is reflected or adsorbed, and after the latter case C-H bond breaking can occur. The single impact of each type of radical on each of the five surfaces at each of the four different temperatures, i.e. a total of 60 simulations cases, is repeated 500 times, to obtain statistically reasonable results.

In the case of the consecutive impacts, each impact is followed for 6.25 ps, at temperatures of 400 K, 800 K, 1000 K, 1200 K, 1400 K and 1600 K. The resulting surface is subsequently used as input configuration for the next impact. Therefore, the impacting radicals are not only adsorbed or reflected, but they can also react with previously adsorbed radicals. As a result, new species are formed, which are removed from the system if they desorb from the surface. Additionally, H-atoms that diffused through the nickel structure to the lowest layer are also removed. This procedure is repeated 150 times for the $CH_3$ impacts, and 250 times for the $CH_2$ and CH impacts. For each case, i.e., for each sequence of impacts of each type of radical on each of the five surfaces at each of the six different temperatures, three simulations are performed, leading to a total of 270 consecutive impacts simulations (each consisting of 150 impacts for $CH_3$ and 250 impacts for $CH_2$ and CH). The reported results are the averages over the three simulations per case, with the associated standard deviations.

In order to clarify the obtained trends, the diffusion of H-atoms over pristine nickel surfaces is also simulated for a time of 6.25 ps (i.e. the simulation time of one consecutive impact). These simulations are carried out for Ni(111) and Ni(100), with 4 H-atoms on each surface, and repeated 30 times for both cases. From these simulations, the average distance the H-atoms moved over the surface is calculated.

## 5.3. Results and Discussion

### 5.3.1. Effect of temperature and nickel surface structure on $H_2$ formation

a) C-H bond breaking probability

The influence of both temperature and the specific nickel surface structure on the average number of broken C-H bonds after adsorption of a $CH_x$ radical is shown in Figures 5.1 and 5.2. The temperature influence on the C-H bond breaking is the largest for adsorbed $CH_3$ radicals. At 400 K, adsorbed $CH_3$ radicals remain kinetically stable and only rarely a C-H bond is broken. As the temperature increases towards 800 K, the bond breaking starts to occur more often. Further heating has even a greater effect, as illustrated in Figure 5.1. However, the reactivity is still low, since at the highest temperature of 1600 K, maximum 1.14 out of three C-H bonds are broken after adsorption.

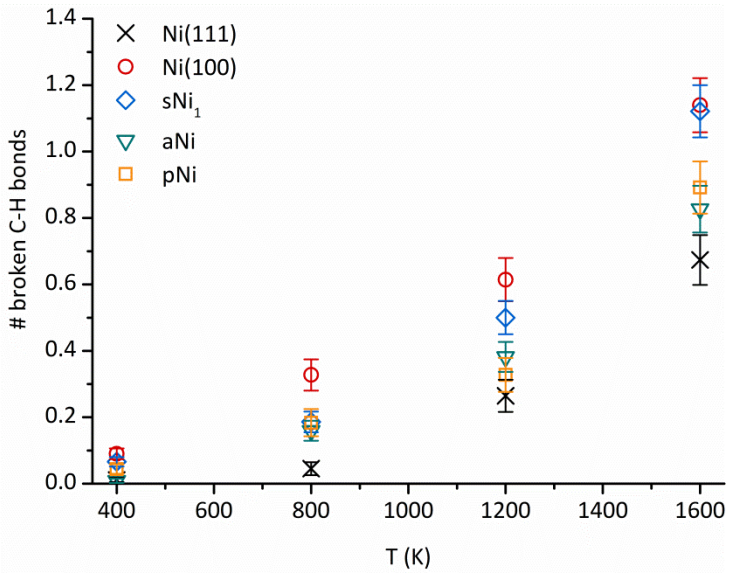


**Figure 5.1:** Average number of broken C-H bonds after adsorption of a single $CH_3$ radical (i.e., after non-consecutive impacts) as a function of temperature and for various surface structures. The error bars represent the standard deviation of the average, calculated over 500 simulations.

For the $CH_2$ and CH radicals, there is already sufficient bond breaking at 400 K and 800 K (see Figure 5.2). This is still promoted by increasing the

temperature, but not to the same extent as for the $CH_3$ radicals. The highest reactivity is obtained for the CH radicals, since about 65% - 85% of the adsorptions are followed by breaking of the one C-H bond at 400 K, and up to 80% – 95% at 1600 K. The reactivity of the $CH_2$ radicals lies between that of CH and $CH_3$, with a maximum number of broken C-H bonds varying from about 0.75 – 1.00 at 400 K to around 1.15 – 1.40 out of 2 C-H bonds at 1600 K.

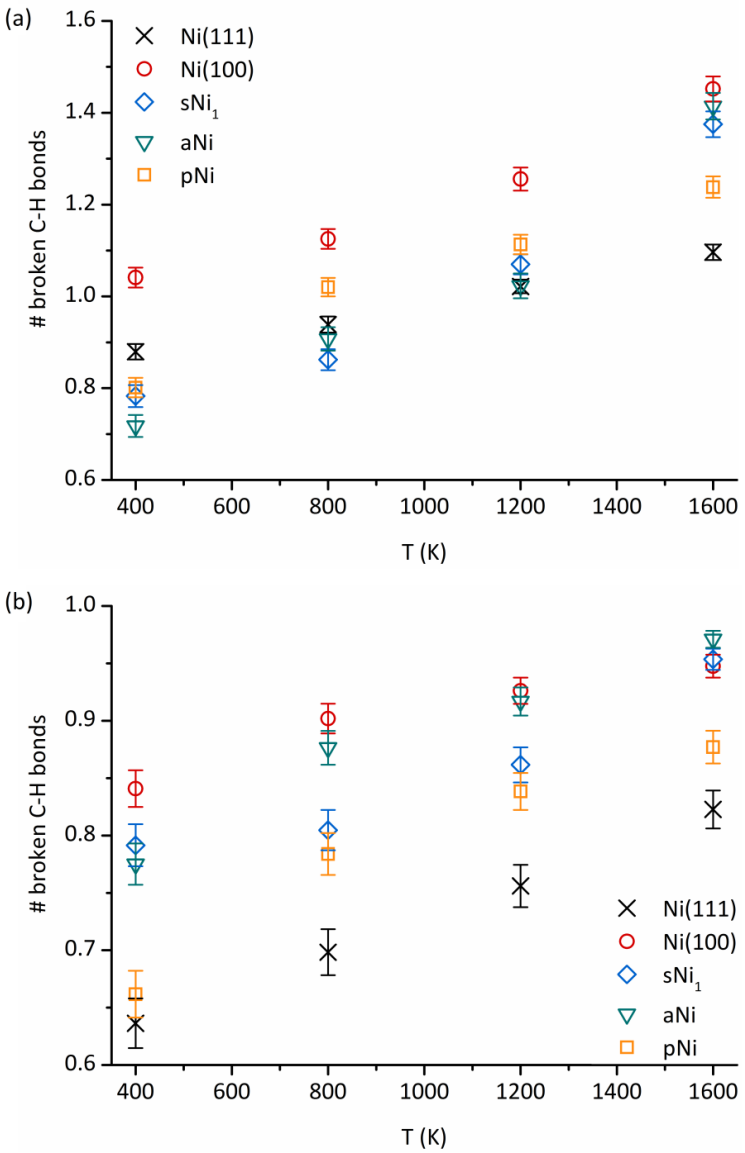


**Figure 5.2:** Average number of broken C-H bonds after adsorption of a single (a) $CH_2$ and (b) CH radical (i.e., after non-consecutive impacts) as a function of temperature and for various surface structures. The error bars represent the standard deviation of the average, calculated over 500 simulations.

If we now consider the role of the nickel surface, clear differences between the five surfaces are observed. The Ni(111) surface, which is the most stable Ni-surface, has the lowest reactivity over the investigated temperature range for each type of radical. In contrast, the higher energy Ni(100) surface clearly promotes C-H bond breaking. Furthermore, the results for the polycrystalline structure are as expected, namely between those of Ni(100) and Ni(111), since pNi contains both structures. As discussed in Chapter 3, the presence of step-edges on Ni(111) improved the reactivity at 400 K; the same is now observed at higher temperatures, for which $sNi_1$ is amongst the most reactive surfaces. Finally, the number of broken C-H bonds on aNi is mostly located between the results of the other surfaces. This implies that a surface with a reduced crystallinity can give a high reactivity. A similar conclusion on the high reactivity of amorphous structures has been made before [155].

Overall, the influence of the surface on C-H bond breaking is the most significant for the $CH_3$ radicals, where the number of broken C-H bonds per impact rises from 0.67 on Ni(111) to 1.14 on Ni(100) at 1600 K, hence a difference of 0.47 broken C-H bonds per impact. For the same temperature, this difference is 0.36 and 0.12 broken C-H bonds for the $CH_2$ and CH radicals, respectively. Although the influence of temperature and surface structure is the highest for the $CH_3$ radicals, the reactivity is still the lowest compared to the other radicals.

b) $H_2$ formation

These results indicate the role of the surface structure in creating H-atoms bound to the nickel surface. During consecutive impacts, these H-atoms can react with other incoming radicals or recombine with each other into $H_2$. Since most C-H bond breaking occurs on Ni(100), we would expect that more $H_2$ is formed after impacts on this surface. However, the expected trend is not observed in the results of the consecutive impacts, as shown in Figures 5.3 and 5.5.

*$CH_3$ impacts*

In case of the $CH_3$ radicals (see Figure 5.3), roughly two $H_2$ molecules are formed after 150 impacts on Ni(100), with hardly any temperature dependency. Furthermore, the difference between the surfaces remains small, at least at temperatures up to 1200 K. The first significant difference between the surfaces is obtained at 1400 K, while at 1600 K, a clear separation between the values is obtained. For this latter temperature, $sNi_1$ has the highest selectivity towards $H_2$ and Ni(100) the lowest selectivity. While the stepped Ni(111) surface yields a similar number of broken C-H bonds after adsorption of a $CH_3$ radical as the Ni(100) surface (see Figure 5.1), five times more $H_2$ molecules are formed on the $sNi_1$ surface. Therefore, there must be other factors that affect the $H_2$ formation.

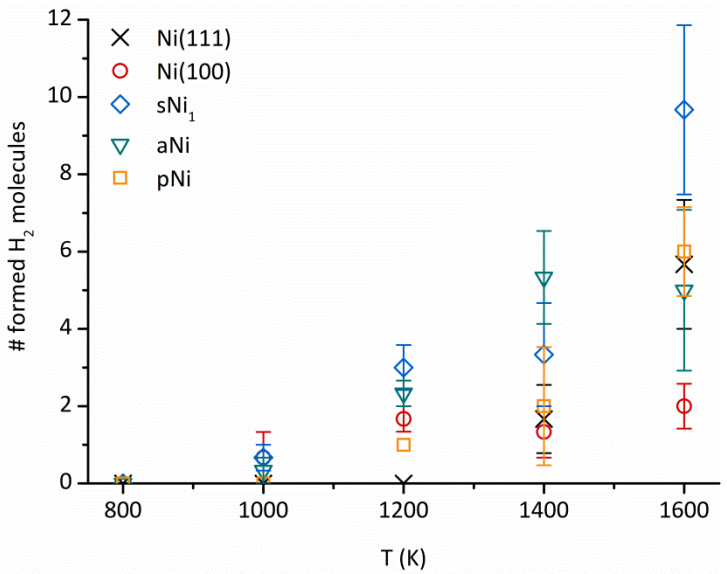


**Figure 5.3:** Average number of formed $H_2$ molecules, and associated standard deviations over the three simulations, after consecutive impacts of 150 $CH_3$ radicals as a function of temperature and for various surface structures.

Indeed, besides recombining to $H_2$, the adsorbed H-atoms can also react with incoming $CH_3$ radicals, or diffuse into the surface. The interaction with incoming $CH_3$ is found to be very similar on all investigated surfaces. The diffusion of H-atoms into the surface, on the other hand, turns out to be surface dependent, as shown in Figure 5.4. The H-diffusivity is the highest for

Ni(100), and hence less H-atoms remain available on this surface to form $H_2$. Since both Ni(111) and $sNi_1$ have the same orientation, they also have a similar H-diffusivity. These observations are consistent with the more open surface packing of the Ni(100) surface in comparison with the close-packed Ni(111) surface structure (cf. Figure 2.1), rendering H-diffusion into Ni(100) more favorable. The difference in $H_2$ formation on the Ni(111) and $sNi_1$ surfaces is therefore determined by the C-H bond breaking probability, which is indeed higher on $sNi_1$, as illustrated in Figure 5.1.

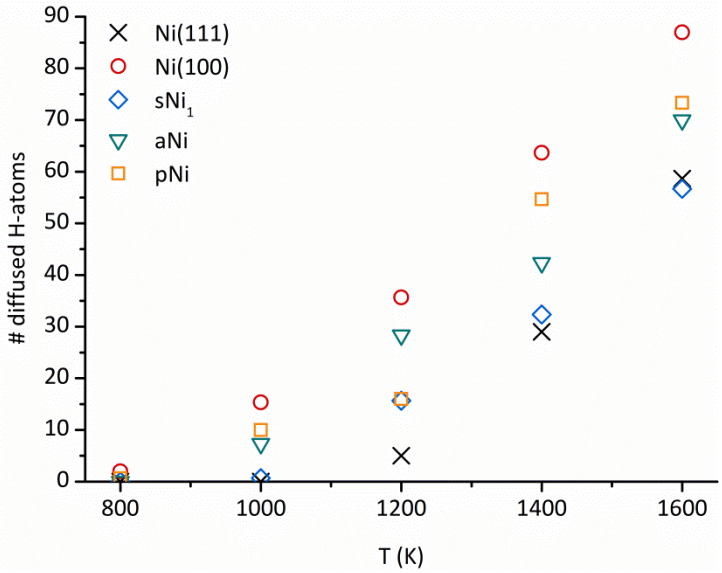


**Figure 5.4:** The number of H-atoms that diffuse into the surface after consecutive $CH_3$ impacts as a function of temperature and for the various surface structures.

The H-diffusion into the surface of pNi and aNi, as well as the number of broken C-H bonds after adsorption, is a little higher than on Ni(111) at 1600 K. Hence, the combination of these two opposite factors results in a similar number of $H_2$ molecules formed on pNi, aNi and Ni(111).

*$CH_2$ and CH impacts*

In case of the $CH_2$ and CH impacts, the difference in $H_2$ formation between the surfaces is again observed mainly at higher temperatures, i.e. starting from 1400 K for $CH_2$, or 1200 K for CH (see Figure 5.5a-b). Remarkably, $sNi_1$ is the surface with the lowest selectivity towards $H_2$ formation after 250 $CH_2$ and CH

impacts under these conditions, although it still has a relatively large number of broken C-H bonds and the lowest H-diffusivity. Furthermore, the $H_2$ formation at 1600 K is almost equal on Ni(111) and Ni(100), although the difference between both surfaces in C-H bond breaking and H-diffusivity into the surface is comparable to that after the $CH_3$ impacts. From these values, it should be expected that Ni(100) has a lower $H_2$ selectivity, as it was the case for the $CH_3$ impacts. However, this is in contrast to the observed results.

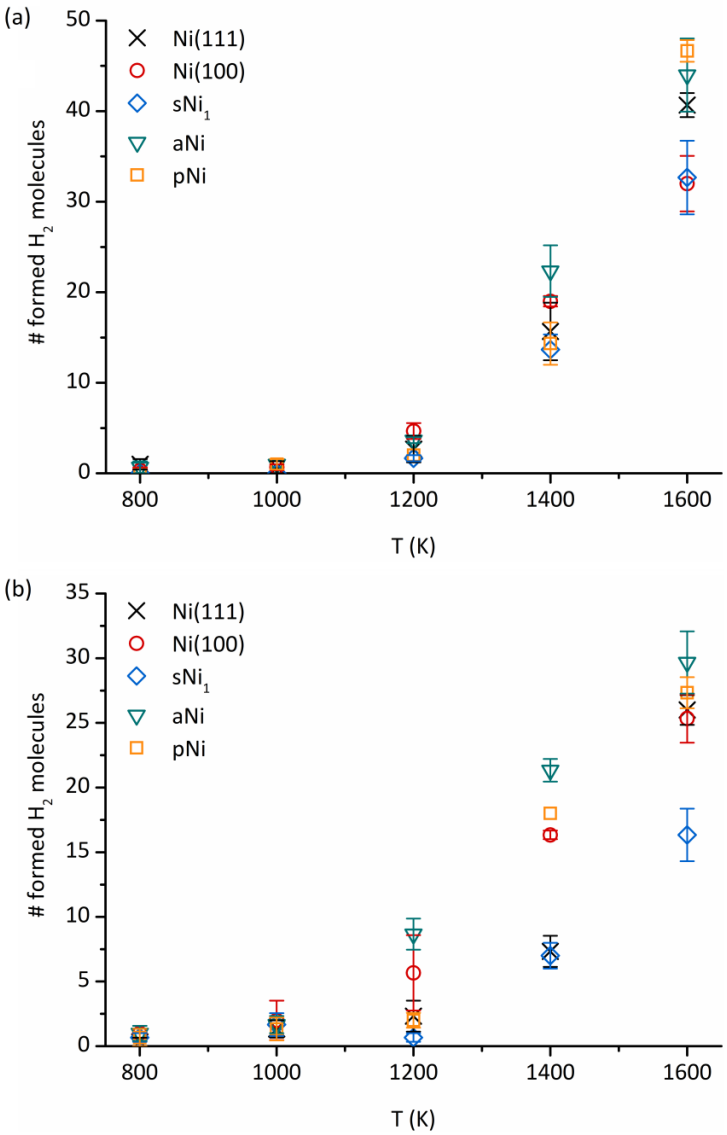


**Figure 5.5:** Average number of formed $H_2$ molecules, and associated standard deviations over the three simulations, after consecutive impacts of (a) 250 $CH_2$ and (b) 250 CH radicals as a function of temperature and for various surface structures.

Apparently, analysis of the C-H bond breaking and H-diffusivity is not sufficient to explain the observed differences after $CH_2$ and CH impacts, and other aspects need to be taken into account.

One of these aspects is the formation of other $CH_x$ and $C_2H_x$ molecules, which also reduces the number of H-atoms on the surface available for $H_2$ formation. However, there is no clear dependency between this aspect and the $H_2$ formation. For instance, both Ni(111) and $sNi_1$ show the most abundant $CH_x$ formation and a similar H-diffusivity during the consecutive $CH_2$ impacts, but the $H_2$ formation seems more probable on Ni(111) than on $sNi_1$, in spite of the lower C-H bond breaking probability on Ni(111).

Another factor that is taken into account is the diffusion rate of the H-atoms over the surface. If the diffusion rate is indeed surface dependent, the H-atoms will cover different distances over the different surfaces within the same simulation time. The longer the distance travelled by the H-atoms, the larger the probability of encountering another H-atom and recombining to $H_2$. Comparison of the diffusion rate over the entire temperature range, however, shows that the differences between Ni(111) and Ni(100) are too small to explain the dissimilarities in $H_2$ selectivity between both surfaces, as illustrated in Figure 5.6. Especially at temperatures of 1400 K and above, the covered distance on both surfaces is in the order of 220 Å, with a maximum difference of 10 Å (i.e. less than 5% deviation between both surfaces).

It should be noted that these diffusion distances are calculated on pristine nickel surfaces, so the deviation between the surfaces might increase after consecutive impacts. However, because of the similar order of magnitude on the pristine surfaces, we do not expect large differences after consecutive impacts.

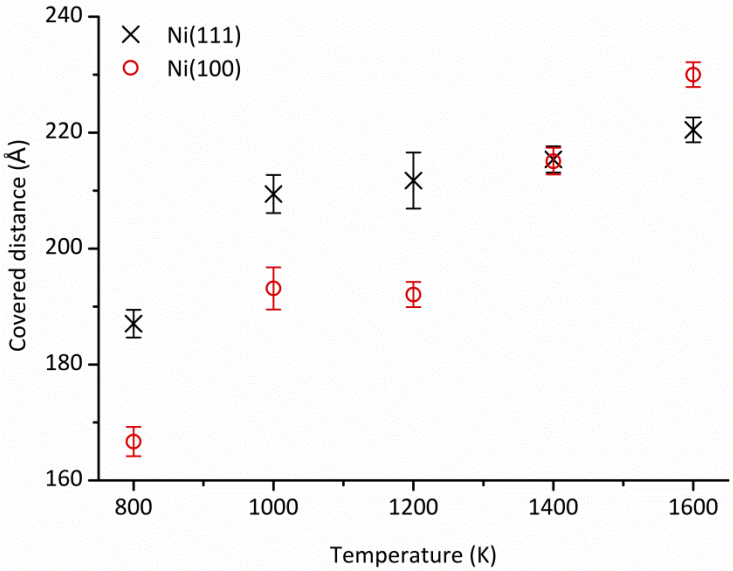


**Figure 5.6:** Covered diffusion distance of an adsorbed H-atom and the associated standard deviation as a function of temperature on Ni(111) and Ni(100).

Finally, the role of the number of adsorbed C-atoms is considered. Each adsorbed C-atom can undergo C-H bond breaking; therefore, more adsorptions can lead to more H-atoms on the surface. After 250 consecutive $CH_2$ and CH impacts, no correlation between $H_2$ formation and the number of adsorbed C-atoms is found for most cases. However, the low $H_2$ selectivity of $sNi_1$ during the $CH_2$ and CH impacts (see Figure 5.5) can be a consequence of the much smaller number of adsorbed C-atoms on this surface compared to the other surfaces. Indeed, there are about 7 and 14 adsorbed C-atoms less on $sNi_1$, after the $CH_2$ and CH impacts, respectively. Furthermore, the influence of steps in the surface on the C-H bond breaking is the largest for the adsorbed $CH_3$ radicals, while the difference with the other surfaces is much smaller for the $CH_2$ and CH radicals, as shown in Figures 5.1 and 5.2. This decrease in difference between the surfaces on C-H bond breaking probability, together with the decrease in the number of adsorbed C-atoms leads to the lower $H_2$ formation. This correlation between $H_2$ formation and the number of adsorbed C-atoms, however, is only observed for $sNi_1$.

Since there are no clear explanations for the different $H_2$ selectivities at temperatures of 1400 K and higher in the case of $CH_2$ and CH impacts, we need to consider whether it is still correct to distinguish the surfaces from each other at these temperatures. In Chapter 4, we already illustrated that at such temperatures, carbon diffusion in Ni(111) becomes a dominant process, with diffusion into the lower-lying Ni-layers. The same is observed for the other surfaces, especially after the $CH_2$ and CH impacts. This diffusion eventually leads to a loss of crystallinity in the top layers of the surface, since more and more C-atoms are positioned between the Ni-atoms. At this point, the formation of new $H_2$ molecules cannot be fully allocated to the initial surface structure, since the latter is not maintained anymore.

In Figure 5.7, the $H_2$ formation at 1400 K is followed on the different surfaces as a function of the number of $CH_2$ impacts. As illustrated already in Figure 5.5a, there is a considerable difference in the number of $H_2$ molecules formed after 250 impacts. However, after approximately 100 – 125 impacts, the maximum difference is only 5 $H_2$ molecules.

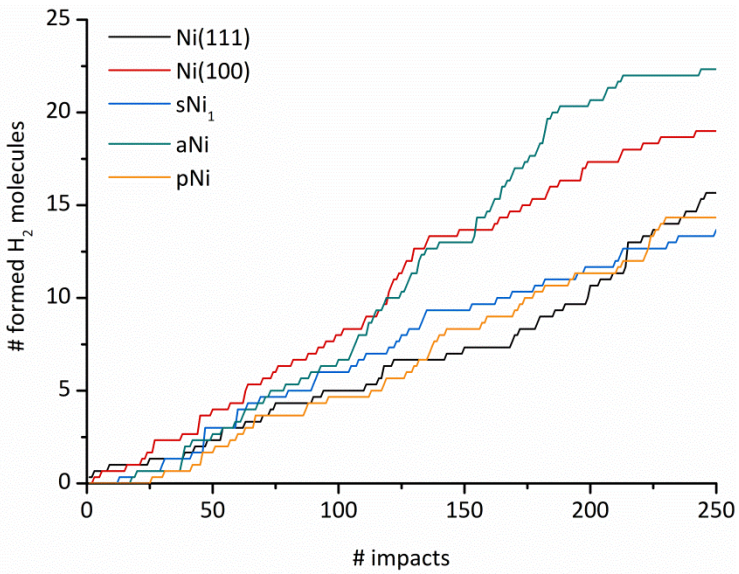


**Figure 5.7:** Average number of formed $H_2$ molecules as a function of the number of $CH_2$ impacts on the various nickel surfaces at 1400 K.

Note that these $CH_2$ impacts are followed by C-diffusion, but certain regions of the top layer still maintain their crystallinity. This is illustrated for Ni(111) in Figure 5.8, for which the top layer exists mostly out of the (111) facet after 50 $CH_2$ impacts.

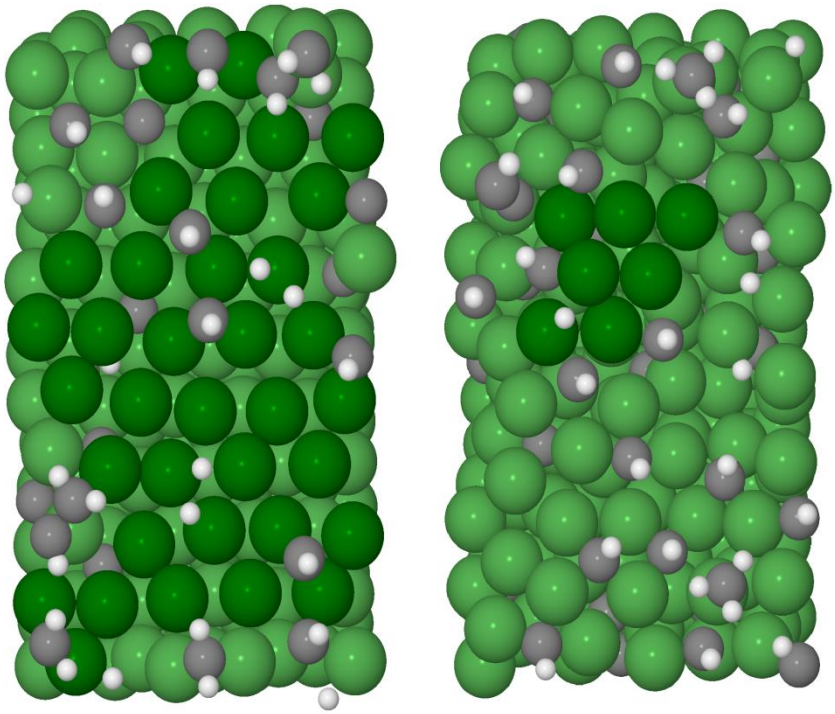


**Figure 5.8:** Top view of the Ni(111) surface after (a) 50 and (b) 125 consecutive $CH_2$ impacts at 1400 K. The dark green spheres represent the (111) facet in the top layer.

This crystallinity gradually decreases during the following impacts, resulting in only a small (111) facet after 125 impacts. However, up to this point, the observed differences in $H_2$ formation can still be explained by the C-H bond breaking probability and the H-diffusivity, combined with the total number of adsorbed C-atoms and the loss of H-atoms in reactions (excluding $H_2$ formation). While these last two factors did not show an obvious dependency with the $H_2$ formation after 250 impacts, except for the adsorbed C-atoms on $sNi_1$, their role is more clear for the first 125 impacts. After 125 $CH_2$ impacts, both Ni(100) and aNi have the same number of adsorbed C-atoms, and the same loss of H-atoms due to diffusion or reactions. However, the C-H bond

breaking after adsorption is slightly higher for Ni(100), hence the slightly higher $H_2$ formation for the first 100 – 125 impacts. For pNi, both the total number of adsorbed C-atoms as the C-H bond breaking probability are lower than for Ni(100) and aNi, while the same number of H-atoms are lost. This results in the lower number of formed $H_2$ molecules. The Ni(111) surface has the lowest C-H bond breaking probability, and the lowest number of adsorbed C-atoms, hence this explains its low $H_2$ selectivity after 125 impacts. The only difference between Ni(111) and $sNi_1$ at this point is the higher C-H bond breaking for $sNi_1$, therefore, more $H_2$ is formed on this surface than on Ni(111).

However, during the next 125 impacts more carbon is added to the surface, and the continued diffusion of C-atoms into the subsurface and bulk reduces the crystallinity in the top layers. As a consequence, the correlation between $H_2$ formation and the type of nickel surface becomes unclear, since the trends of the first 125 impacts are not maintained anymore. Gradually, aNi becomes the most $H_2$ selective surface, and the reactivity of Ni(111) starts to increase more rapidly. Especially the latter case is curious, since less C-atoms are adsorbed on Ni(111) than on aNi, and the C-H bond breaking after adsorption is the lowest for Ni(111). However, this C-H bond breaking is determined with single, non-consecutive impacts on a pristine nickel surface. During the consecutive impacts, the bond breaking occurs on a less crystalline surface with adsorbed C- and H-atoms on it, which will influence the initial bond breaking probability.

Additionally, the increased diffusion during the last 125 impacts also influences the C-H bond breaking, since it further changes the crystallinity. Therefore, the C-H bond breaking probability might alter during the impacts, dependent of surface structure and C-diffusion. This makes it difficult to estimate which surface has the highest C-H bond breaking probability. Furthermore, the alteration in C-H bond breaking probability and surface structure is different for each simulation, hence giving rise to deviations between the simulations, which are difficult to define. This implies that,

despite the fact that all surfaces are amorphous after 250 impacts; each surface still has a particular (amorphous) structure, different from the other surfaces. Therefore, each of these amorphous surfaces has its own reactivity, which results in different hydrogen formation rates for the various surfaces. We conclude that the nickel surface structure initially (strongly) influences the reactivity after adsorption. However, the effect on long-term reactivity, i.e., after more than 125 consecutive impacts, is limited due to loss of crystallinity and change of the C-H bond breaking probability.

### 5.3.2. Effect of temperature and nickel surface structure on the reactivity of adsorbed H-atoms

In the previous section, we focused on the influence of the nickel surface structure on the $H_2$ formation. As shown in Figures 5.3 and 5.5, and as described in Chapter 4, substantial $H_2$ formation is obtained at temperatures of 1400 K and above at all Ni surfaces. For processes focusing on the catalytic synthesis of $H_2$, our simulations predict that this is the required temperature regime. However, in plasma systems, $H_2$ is also formed through several reactions in the gas (plasma) phase, involving radicals, electrons and ions. This includes the three-body recombination reaction among two H-atoms, with a gas molecule as third body, as well as several other chemical reactions of H-atoms with hydrocarbons [82]. Moreover, besides the formation of $H_2$, the reactions between H-atoms and hydrocarbons can also form other hydrocarbon species [82]. In plasma catalysis, H-atoms are not only present in the gas phase, but they are also adsorbed on the catalyst surface. Therefore, it is important to know in general to what extent adsorbed H-atoms can participate in reactions with incoming radicals or other adsorbed species and subsequently desorb from the catalyst surface.

In Chapter 3, we demonstrated that at a temperature of 400 K, the H-atoms adsorbed on Ni(111) after $CH_2$ impacts rarely react with incoming radicals, while this reaction does occur on the other surfaces. As shown in Figure 5.9, a temperature increase to 800 K is already sufficient to activate the adsorbed H-

atoms on Ni(111) to react with incoming radicals and form new molecules (i.e. mostly hydrocarbons and little $H_2$). Indeed, at first, the impacts lead to adsorption and dissociation of $CH_2$, which generates adsorbed H-atoms. Subsequently, the number of adsorbed H-atoms decreases as they react with the incoming radicals. This is in contrast to the behavior at 400 K for Ni(111), where the number of surface-bound H-atoms remains constant, indicating that the H-atoms do not react with incoming radicals to form new products (such as hydrocarbons or $H_2$ molecules). However, the incoming radicals do react with other species adsorbed on the Ni(111) surface, such as $CH_2$ and CH, which can still lead to the formation of hydrocarbons. For the other surfaces investigated, the surface bound H-atoms already participate in recombination reactions at 400 K, and a temperature increase has less effect, as illustrated for Ni(100) in Figure 5.9.

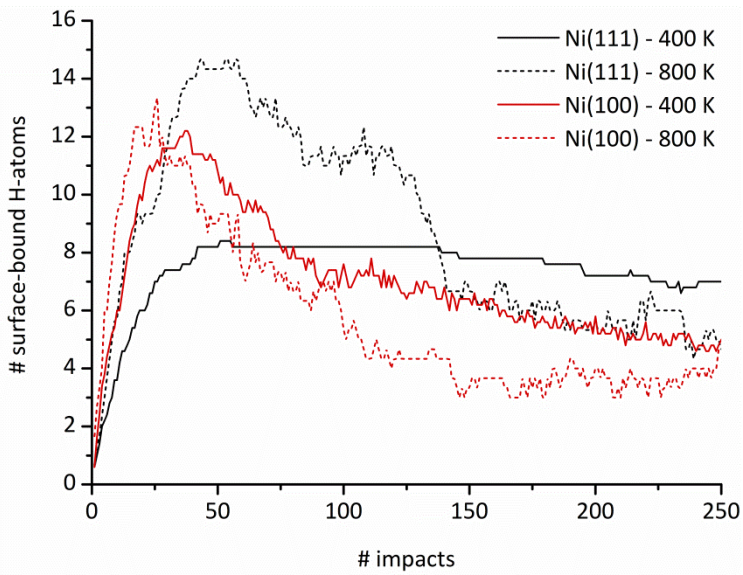


**Figure 5.9:** Average number of surface-bound H-atoms as a function of the number of $CH_2$ impacts for Ni(111) and Ni(100) at 400 and 800 K.

Furthermore, performing the impacts at a temperature of 800 K instead of 400 K hardly influences the total number of adsorbed C-atoms after the $CH_x$ impacts, and the diffusion of C-atoms into the nickel surface remains low, as illustrated in Figure 5.10. Therefore, we expect a similar (limited) amount of coke formation at 400 and 800 K. Further increasing the temperature leads to

additional adsorption of C-atoms, as shown for Ni(100) in Figure 5.11. This is due to the promoted diffusion of C-atoms into the surface at such high temperatures (cf. previous section), which regenerates areas for adsorption in the top layer.

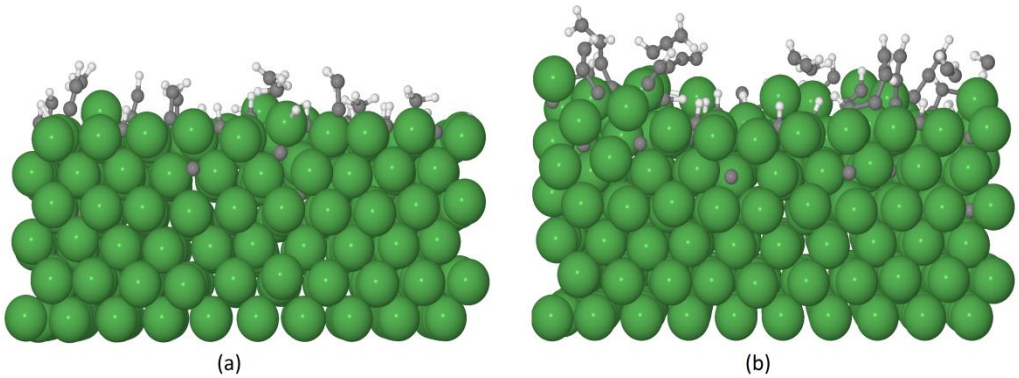


**Figure 5.10:** Side view of Ni(100) after 250 (a) $CH_2$ and (b) CH impacts at 800 K to illustrate the low number of diffused C-atoms into the surface.

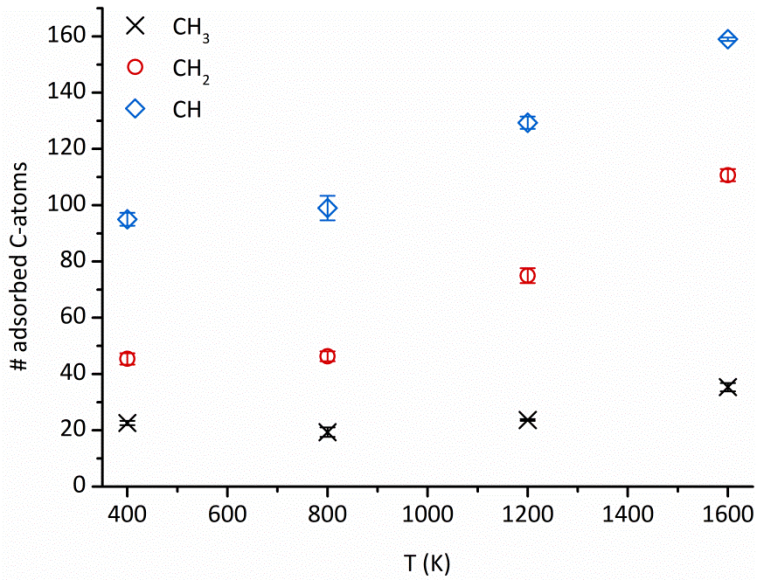


**Figure 5.11:** Average number of adsorbed C-atoms on Ni(100) after consecutive impacts of the three radicals as a function of temperature.

As discussed earlier, carbon deposition can reduce the performance of the catalyst in the reforming process. If the focus lies on the catalytic synthesis of $H_2$ or the growth of carbon nanotubes, temperatures of 1400 K and above are appropriate. However, for optimizing the reforming process, and more

specifically the catalyst lifetime, lower temperatures are preferred to avoid catalyst deactivation by coke deposition and sintering [156].

At temperatures of 1200 K and above, a large number of adsorbed C-atoms diffuse into the nickel surfaces. Within the current time scale, no accumulation of the C-atoms or polymerization of $C_nH_m$ radicals on the surface is observed. Such processes deactivate the catalyst and are most likely to occur at high temperatures. However, the fact that these processes are not observed is most probably related to the short time scales of the simulations. As stated before, the carbon diffusion into the surface is low in the range of 400 – 800 K, so a limited amount of coke formation is expected. Furthermore, the results discussed above indicate that a temperature of 800 K is sufficient to induce interactions between plasma species and H-atoms adsorbed on the various nickel surfaces studied in this work. Even at 400 K, these interactions already occur, although less frequently on Ni(111).

In view of this observation, and keeping in mind the multiplicity of reactions in the plasma, the combination of plasma technology and catalysis for methane reforming seems already promising in the temperature range of 400 – 800 K. The carbon diffusion, and possible coke formation, remains low in this temperature range, while all the adsorbed species interact with the incoming radicals. Obviously, in a plasma system, additional species besides the studied $CH_x$ radicals are present (e.g. other radicals, excited species,…), which can further enhance the reactivity in this temperature range.

## 5.4. Conclusion

The interactions of impacting $CH_x$ radicals on nickel catalyst surfaces were investigated as a function of temperature and surface structure.

After adsorption of a single $CH_x$ radical, the subsequent C-H bond breaking depends on both the temperature and exact surface structure. At higher temperatures, more C-H bonds get broken upon impact of $CH_x$ radicals. The

temperature influence on the bond breaking process after adsorption is the highest for $CH_3$, which is kinetically stable at low temperatures (i.e. 400 K), followed by $CH_2$ and CH.

Furthermore, there is an increased C-H bond breaking for each type of radical on Ni(100) and sNi, compared to Ni(111). These two surfaces have a higher surface energy or presence of step-edges in the structure compared to the Ni(111) surface. The results for pNi, which is partially (111) and (100) oriented, are between those of Ni(111) and Ni(100), as expected. More importantly, an amorphous structure gives a high reactivity, which is located between those of the other surfaces. Remarkably, the surfaces that promote the C-H bond breaking are not necessarily the most selective towards $H_2$ formation after consecutive impacts of the radicals at high temperatures, i.e., 1400 K and above.

For the $CH_3$ impacts, the observed differences can be attributed to the H-diffusivity into the surface. This diffusivity is the highest for Ni(100), and hence less H-atoms are available to recombine into $H_2$. However, for the $CH_2$ and CH radicals, for which the reactivity after adsorption is much higher, no clear correlation between surface structure and $H_2$ formation is found after 250 impacts. This is attributed to a loss of crystallinity induced by diffusion of multiple C-atoms into the surface. The top layer of the different surfaces loses its initial structure; hence a proper distinction between the surfaces cannot be made anymore. We therefore conclude that the nickel surface structure initially influences the C-H bond breaking, and therefore the $H_2$ formation, but as the carbon diffusion in the surface increases, the role of the surface structure seems to become limited.

It is demonstrated that the $H_2$ formation at the catalyst surface requires temperatures in the order of 1400 K. However, in plasma catalysis, the plasma also contributes to the $H_2$ (and hydrocarbon) formation, by reactions involving radicals, electrons and ions. Since reactions with H-atoms in the plasma can lead to the formation of $H_2$ or hydrocarbons, the extent to which adsorbed H-

atoms at the catalyst surface desorb and further react in the plasma can also be of importance.

Only on Ni(111), the adsorbed H-atoms rarely react with incoming radicals at a temperature of 400 K. Increasing the temperature to 800 K overcomes this limitation. On the other surfaces, the adsorbed H-atoms can already react with incoming radicals at 400 K as well. Furthermore, the total number of adsorbed C-atoms remains almost the same at 400 K and 800 K for all surfaces.

We conclude that methane reforming by plasma catalysis seems promising in this temperature range, since the reactivity of the adsorbed species is already fairly high, and the diffusion of C-atoms into the surface remains low.

The findings of this chapter can be summarized as follows:

- Influence of temperature:
  - Increased C-H bond breaking at higher temperatures
  - Significant $H_2$ formation at 1400 K and above
  - Increased C-diffusion into the surface at high temperatures
- Influence of surface structure:
  - Initially influences C-H bond breaking and $H_2$ formation
  - Continuous C-diffusion at high temperatures reduces the crystallinity and the influence of the surface structure on the $H_2$ formation
- Reactivity of adsorbed H-atoms:
  - Temperature of 400 K – 800 K is optimal for interactions of adsorbed H-atoms with incoming radicals

# Chapter 6:
# Addition of vibrationally excited $CH_4$ to reactive molecular dynamics simulations

In this chapter, the scope of our research is expanded to the reactivity of vibrationally excited molecules. Vibrational excitation should normally be described with a quantum mechanical approach, while our classical MD simulations do not properly address quantization of energy. Therefore, in this chapter, we explore the possibility and limitations to describe vibrational excitation with a classical approach.

In practice, vibrational excitation can be incorporated by either increasing the initial potential energy (by stretching the bonds to an appropriate length), or by calculating the vibrational velocities, which contribute to the kinetic energy. The latter method is the most interesting, since the atomic velocities can be linked to the normal coordinates of each vibrational mode. Therefore, each vibrational mode can be addressed.

Subsequently, the stability of the vibrational motions in the MD simulations is studied. It is shown that the symmetric vibrational modes remain stable for a simulation time of 6.25 ps (i.e., sufficient for a single impact). Beyond this time scale, deviations in the vibrational motion start to develop. The antisymmetric vibrational modes induce rotational motion. This can be corrected for the antisymmetric stretch vibration, but not for the antisymmetric bending vibration.

## 6.1. Introduction

As described in the first chapter, a plasma consists of a large variety of species, including electrons, ions, photons, radicals, and also electronically, vibrationally and rotationally excited species. After having studied the interactions of $CH_x$ radicals on nickel surfaces in the previous chapters, we now focus on the reactivity of vibrationally excited $CH_4$. However, it is not straightforward to describe such excitations in MD simulations.

In order to describe vibrational excitation, specific quanta of energy should be added to the molecule, to shift the molecule from its ground state to a higher vibrational state. Simply adding such energy quanta to the MD simulation is not sufficient, since the extra energy can be distributed over the translational, rotational and vibrational degrees of freedom. Furthermore, even if the extra energy is fully allocated to the vibrational motion of the molecule, the vibration will be random, i.e., a superposition of all vibration modes. This is because in a classical force field, the potential energy landscape does not describe the specific vibrational modes that require specific energy quanta. For instance, from the quantum chemical point of view, $CH_4$ is excited from the ground state to the fundamental of the symmetric C-H stretch vibration if 34.89 kJ/mol is added [113]. If, on the other hand, 36.11 kJ/mol is added, the fundamental of the anti-symmetric stretch is reached. The addition of a random amount of energy that does not correspond to an energy quantum of a vibrational mode will not lead to vibrational excitation. However, if these energies are added in the MD simulations, even a random amount, the vibrational motion will increase, but not mode specific. It is thus necessary to specify which vibrational mode is excited and which level is reached, instead of just adding the extra energy.

In the first part of this chapter, it is described how we added vibrational excitation to the simulations, in a mode-specific way. Our approach starts by increasing the initial potential energy by increasing the bond length(s), to

verify if such an increase in energy is maintained over the length of the simulation and whether it influences the vibrational motion. Subsequently, the vibrational motion is added to the simulation by calculating the vibrational kinetic velocities. For a simple vibration, such as the C-H stretch of the CH radical, these velocities can be easily calculated by solving the appropriate equations describing the kinetic energy. However, for more complex vibrations, such as those that occur in $CH_4$, additional information regarding the vibration is required in order to calculate the vibrational kinetic velocities. This issue is solved by calculating the normal coordinates of each vibrational mode. These coordinates describe the position of each atom in a certain vibrational mode, away from its equilibrium position in the ground state. We then specify the relative contribution of each normal coordinate to its vibrational mode, and link this to the vibrational kinetic velocities of this mode. With this method, we are able to describe the vibrational excitations of $CH_4$.

In the second part of this chapter, the stability of the vibrational motions in the MD simulations is followed for a simulation time of 50 ps.

## 6.2. Description of the simulations

It is essential that the added vibrational energy is maintained during the simulation; the simulations are therefore carried out in the NVE ensemble. In a NVT simulation, either the atomic velocities are rescaled or the equations of motion are modified in order to maintain a constant temperature. Obviously, this effect is not desired if the vibrational motion is to be monitored. Initially, a simulation time of 6.25 ps is chosen, identical to the simulation time for each consecutive impact in the previous chapter. Subsequently, also a longer simulation time of 50 ps is investigated, to study the stability of the vibrational motions in more detail.

In these simulations, the simulation box only contains a single CH radical or a single $CH_4$ molecule. We either increase the potential energy or add the

vibrational kinetic energy at the beginning of the simulation. If the potential energy is increased, no initial velocities are given to the atoms. This guarantees that at the start of the simulation, no translational, rotational or vibrational motion is present. Every "type" of motion, corresponding to a specific degree of freedom that is observed during the simulation, is directly induced by the added potential energy.

If vibrational kinetic energy is added to the system, only vibrational velocities are given to the atoms. Random velocities – which are normally generated for each atom in a typical MD simulation – are thus not included, since they induce a priori unspecified translational and rotational motion of the molecule.

## 6.3. Addition of vibrationally excited motion

### 6.3.1. Addition of vibrational energy to the initial potential energy

In a regular NVE simulation, the total energy of the molecule is distributed over the potential and kinetic energy. Both energy terms will fluctuate during the simulation, such that the total energy remains constant. If we add extra energy at the start of the simulation, the molecule will stay at that increased energy level for the rest of the simulation. In this section, we increase the initial potential energy, and thus total energy, by increasing the maximum bond length of CH and $CH_4$.

a) CH radical, stretch vibration

The CH radical is chosen to test the effect of the increase in potential energy because of its simplicity. The starting configuration of the simulation is the CH radical with a manually fixed maximum bond length of 1.2 Å, corresponding to an excited state, as shown in Figure 6.1.

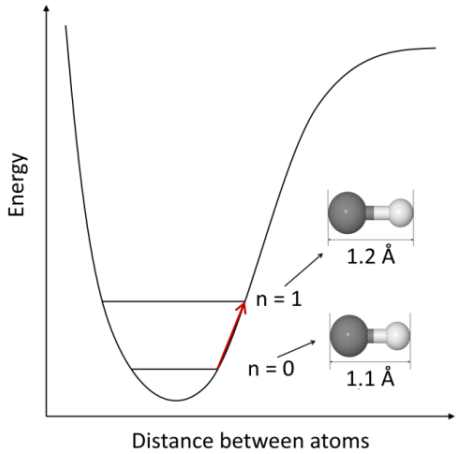


**Figure 6.1:** Representation of the potential energy curve of CH. By increasing the C-H bond length, the energy level is moved from the ground state to the excited state.

During the simulation, the potential energy only exchanges energy with the vibrational component of the kinetic energy, since no translational or rotational motion is observed. Hence, the added energy is fully allocated to the vibrational motion and the maximum C-H bond length of 1.2 Å is maintained over the entire simulation time (see Figure 6.2). This shows that a vibrationally excited state can be reached by increasing the initial potential energy.

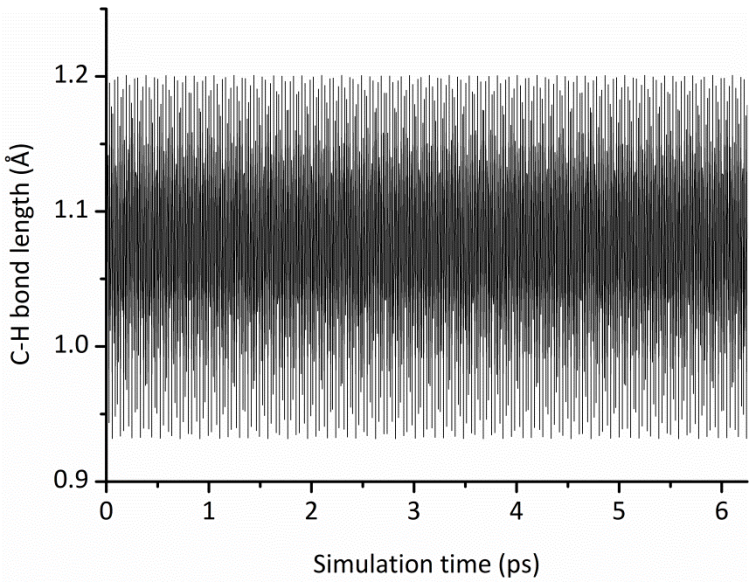


**Figure 6.2:** C-H bond length of the CH radical as a function of simulation time after increasing the initial potential energy.

b) $CH_4$, symmetric C-H stretch vibration

In case of $CH_4$, altering the initial atom positions requires an adjustment of 12 to 15 coordinates, dependent on whether the C-atom moves or not. For the symmetric C-H stretch vibration, however, this number of unknown coordinates can be lowered to just one, by making some simplifications. In this vibrational mode, all four C-H bonds are stretched to the same maximum bond length, while the H-C-H bond angle remains fixed at 109.47°.

The bond length, $r_{CH}$, is calculated as follows:

$$r_{CH} = \sqrt{(x_H - x_C)^2 + (y_H - y_C)^2 + (z_H - z_C)^2} \tag{6.1}$$

Because of the fixed bond angle, the absolute movement in the *x*, *y* and *z* direction is the same, so $|x_H| = |y_H| = |z_H|$. Furthermore, by placing $CH_4$ at the center of the 3D coordinate system, the C-atom coordinates are equal to zero. If $r_{CH}$ is known, the absolute coordinates of the H-atoms can be calculated through equation 6.2:

$$r_{CH} = \sqrt{3 \cdot x_H^2} \Rightarrow x_H = \sqrt{\frac{{r_{CH}}^2}{3}} \tag{6.2}$$

The atom coordinates of the $CH_4$ molecule with a bond length of 1.09 Å, can then be increased to represent $CH_4$ with a maximum bond length of 1.2 Å.

Coordinates for $r_{CH}$ = 1.09 Å:

$$\begin{matrix} C \\ H_1 \\ H_2 \\ H_3 \\ H_4 \end{matrix} \begin{pmatrix} 0.00000 & 0.00000 & 0.00000 \\ 0.63000 & 0.63000 & 0.63000 \\ -0.63000 & -0.63000 & 0.63000 \\ 0.63000 & -0.63000 & -0.63000 \\ -0.63000 & 0.63000 & -0.63000 \end{pmatrix}$$

Coordinates for $r_{CH}$ = 1.2 Å:

$$\begin{pmatrix} 0.00000 & 0.00000 & 0.00000 \\ 0.69282 & 0.69282 & 0.69282 \\ -0.69282 & -0.69282 & 0.69282 \\ 0.69282 & -0.69282 & -0.69282 \\ -0.69282 & 0.69282 & -0.69282 \end{pmatrix}$$

Just as for the excited CH radical, the increased C-H bond length of $CH_4$ is maintained over the simulation, as shown in Figure 6.3. Furthermore, the H-C-H bond angles remain fixed at 109.47°.

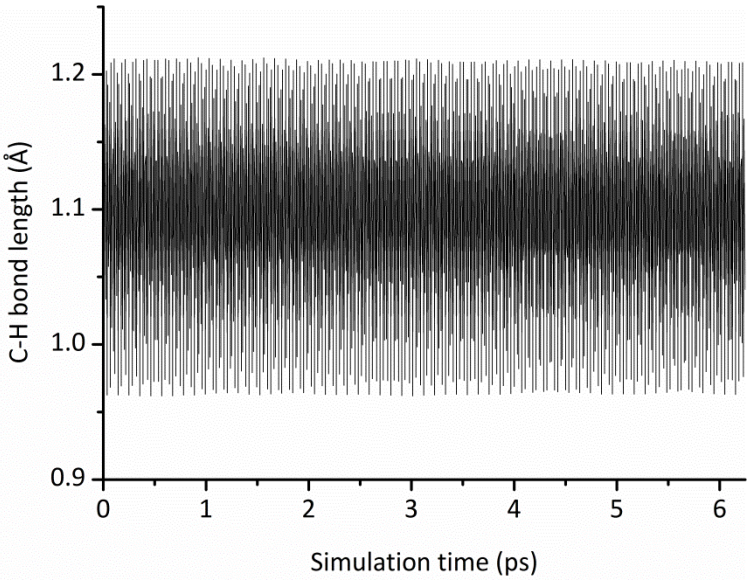


**Figure 6.3:** C-H bond length of $CH_4$ as a function of simulation time after increasing the initial potential energy. All four C-H bonds have the same increased bond length in the symmetric stretch mode.

c) $CH_4$, other vibrational modes

Although the symmetric C-H stretch vibration can be simulated for $CH_4$ simply by changing the initial potential energy, this approach has some limitations for more generic cases.

First, the exact positions of all atoms should be known. In case of the symmetric C-H stretch, these positions are easily calculated. However, for the other symmetric modes, especially the bending modes, too little information is available about the exact positions. Any deviation in the atomic positions results in a wrong description of the vibrational mode.

Second, it is only during the simulation that the added vibrational energy is determined. As described before, each vibrational mode has a specific

vibrational energy. In order to obtain the correct vibrational energy, the atoms need to be positioned very precisely, which can only be reached by a trial-and-error based sequence.

Because of these limitations, a different approach is desirable. In the next section, the vibrational energy is added to the kinetic energy. With this method, it is possible to add a specific amount of energy to the simulation.

### 6.3.2. Direct calculation of the vibrational kinetic velocities

The vibrational energy is calculated with the following equation:

$$E_{vibr} = h\nu\left(n + \frac{1}{2}\right) \tag{6.3}$$

Here, ν is the vibrational frequency and *n* a quantum number that can take values of {0, 1, 2, …}. The vibrational energy is divided over a potential and kinetic energy term. When the vibrational kinetic energy reaches its maximum value, the vibrational potential energy is at its minimum, and vice versa. The vibrational kinetic energy is one of the components of the total kinetic energy, which also consists of translational and rotational energy:

$$E_{kin} = E_{tra} + E_{rot} + E_{vibr} \tag{6.4}$$

Note that the coupling between translational and rotational motion is not taken into account. At the start of the simulations, the molecule is at rest, so it has no initial velocities. Then the maximum vibrational kinetic energy, i.e., the total vibrational energy, is given to the molecule. The maximal vibrational kinetic energy is calculated as follows:

$$E_{vibr} = \sum_{i=1}^{na} \frac{1}{2} m_i v_{i,t}^2 \tag{6.5}$$

Here, *na* is the number of atoms, $m_i$ the mass of atom *i* and $v_{i,t}$ the total vibrational velocity of this atom. This total velocity is determined by the velocity components in the *x*, *y* and *z* directions.

$$v_{i,t} = \sqrt{v_{i,x}^2 + v_{i,y}^2 + v_{i,z}^2} \tag{6.6}$$

By combining equations 6.5 and 6.6, the velocities for a specific vibrational energy can be calculated. Thus, by only adding these velocities to the molecule, $E_{tra}$ and $E_{rot}$ remain zero, and the molecule will only display vibrational motion.

In the next sections, equation 6.5 is first solved for the C-H stretch of the CH radical. Subsequently, the symmetric C-H stretch of $CH_4$ is described, taking into the account the vibrational energy of 52.33 kJ/mol, i.e., the total energy including the zero-point energy. Finally, the applicability of this method for all vibrational modes of $CH_4$ is discussed.

a) <u>CH radical, stretch vibration</u>

The vibrational frequency of the stretch vibration of the C-H bond in the CH radical is 2860 $cm^{-1}$ [157,158]. Therefore, the total vibrational energy of a CH radical excited to the fundamental of this mode is 51.32 kJ/mol. In the previous section, increasing the C-H bond length of the radical to 1.2 Å corresponded to an added vibrational energy of 33 kJ/mol. Because of the higher added vibrational energy in this section, we therefore expect a slight increase in the maximum bond length for this test. The CH radical is aligned with the *z* axis, such that equation 6.5 can be written as:

$$E_{vibr} = \sum_{i=1}^{na} \frac{1}{2} m_i v_{i,t}^2 = \frac{1}{2} m_C v_{C_z}^2 + \frac{1}{2} m_H v_{H_z}^2 \tag{6.7}$$

In this equation, there are two unknowns, i.e., $v_{C_z}$ and $v_{H_z}$. Since both atoms have a different mass, the two velocities cannot be equal. Therefore, an additional independent equation containing both velocities is needed to solve the system. This is provided through equation 6.8, in which the center of mass velocity in the *z* direction, $v_{COM_z}$, is calculated.

$$v_{COM_z} m_T = m_C v_{C_z} + m_H v_{H_z} = 0 \tag{6.8}$$

Since there is no translational motion, $v_{COM_z}$ is equal to zero, and $v_{H_z}$ can be written as a function of $v_{C_z}$:

$$v_{H_z} = -\frac{m_C v_{C_z}}{m_H} \tag{6.9}$$

Equation 6.7 can now be solved by using this formula for $v_{H_z}$:

$$2 \cdot E_{vibr} = m_C v_{C_z}^2 + m_H \cdot \left(-\frac{m_C v_{C_z}}{m_H}\right)^2 \tag{6.10}$$

$$2 \cdot E_{vibr} = m_C v_{C_z}^2 + \frac{m_C^2 v_{C_z}^2}{m_H} = m_C v_{C_z}^2 \cdot \left(1 + \frac{m_C}{m_H}\right) \tag{6.11}$$

$$v_{C_z} = \sqrt{\frac{2 \cdot E_{vibr}}{m_C \cdot \left(1 + \frac{m_C}{m_H}\right)}} \tag{6.12}$$

The velocities of the C- and H-atom can now be calculated as a function of $E_{vibr}$ with equations 6.9 and 6.12. This is done for a vibrational energy of 51.32 kJ/mol, and the resulting C-H vibration is shown in Figure 6.4.

The C-H vibration is maintained during the entire simulation, which is in agreement with the previous test with the increased initial potential energy (cf. Figure 6.2). However, the shape of the curve is much more symmetric, and a clear pattern can be distinguished. Possibly, the exchange in potential and kinetic energy is more fluent, because the kinetic component already has velocities indicating the correct motion. In the case of the increased potential energy, there is no initial kinetic energy, and thus no indication of how the kinetic energy should be distributed over the velocities during the simulation. As expected, the maximum C-H bond length is larger compared to Figure 6.2, due to the higher vibrational energy.

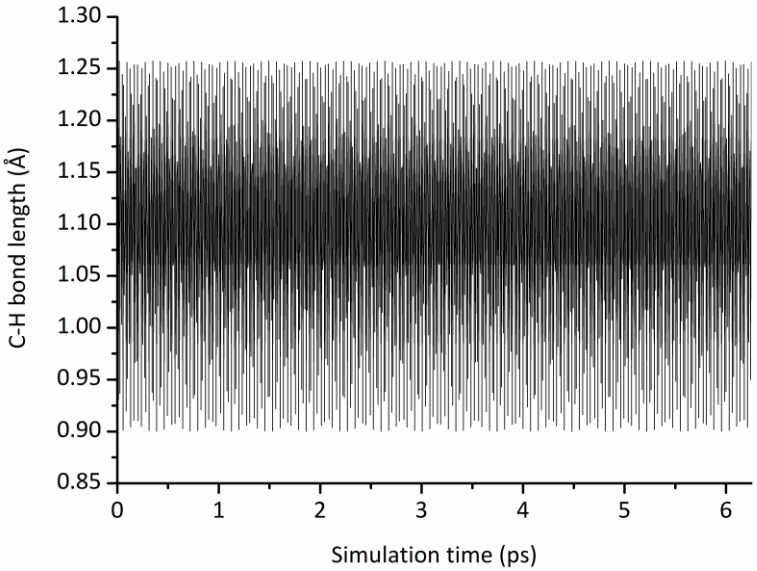


**Figure 6.4:** C-H bond length of the CH radical as a function of simulation time after addition of 51.32 kJ/mol of vibrational kinetic energy.

b) $CH_4$, symmetric C-H stretch

The vibrational frequency of the symmetric C-H stretch of $CH_4$ is 2916 $cm^{-1}$. Therefore, the total vibrational energy of a $CH_4$ molecule excited to the fundamental of this mode is 52.33 kJ/mol.

In order to add this energy as kinetic vibrational energy to the molecule, equation 6.7 is used to calculate the velocities. Because the C-atom does not move in this vibrational mode, this equation can be rewritten as follows:

$$\mathrm{E_{vibr}} = \sum_{\mathrm{i=1}}^{\mathrm{nH}} \frac{1}{2} \mathrm{m_H v_{H_{i,t}}^2} \tag{6.13}$$

Here, *nH* is the number of H-atoms. Again, the total velocity $\mathrm{v_{H_{\mathit{i,t}}}}$ is partitioned over the *x*, *y*, and *z* directions (see equation 6.6). For the symmetric stretch, the total velocity of each atom is the same. Furthermore, the velocity of each atom in each of the three directions is equal for the chosen orientation of $CH_4$ (see atom coordinates in §6.3.1.b):

$$\mathrm{v_{H_{1,x}}} = \mathrm{v_{H_{1,y}}} = \mathrm{v_{H_{1,z}}} = \mathrm{v_{H_{2,x}}} = \cdots = \mathrm{v_{H_{4,z}}} = \mathrm{v_H} \tag{6.14}$$

Therefore, equation 6.13 can be simplified, and subsequently $v_H$ can be calculated with the following equation:

$$E_{vibr} = \frac{1}{2} m_H \left(12 v_H^2\right) \Rightarrow v_H = \sqrt{\frac{E_{vibr}}{6 \cdot m_H}} \tag{6.15}$$

For a vibrational energy of 52.33 kJ/mol, all four C-H bonds fluctuate between 0.99 Å and 1.17 Å, as shown in Figure 6.5. The H-C-H bond angles are constant at 109.47°, as expected for this vibrational mode.

Again, the curve shows a more regular pattern compared to the one obtained by increasing the initial potential energy (cf. Figure 6.3). This approach of calculating the vibrational velocities to obtain a specific vibrational energy seems more accurate than the first approach. Indeed, the change in the C-H bond length resembles more the classical harmonic oscillator approximation of vibrational motion.

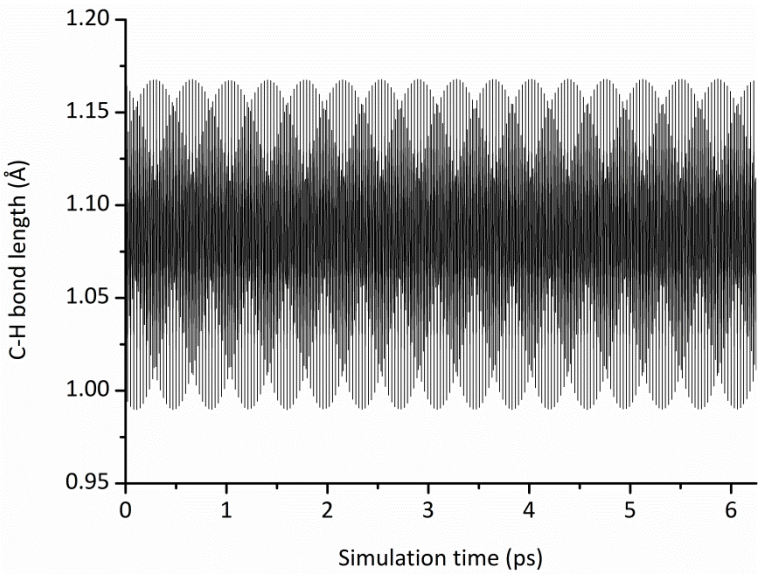


**Figure 6.5:** C-H bond length of $CH_4$ as a function of simulation time after addition of 52.33 kJ/mol of vibrational kinetic energy. All four C-H bonds have the same increased bond length in the symmetric stretch mode.

c) $CH_4$, other vibrational modes

For the other vibrational modes, equation 6.5 cannot be simplified to the same extent as was done for the symmetric C-H stretch vibration. Especially for the antisymmetric vibrations, in which the C-atom also moves, the system cannot be solved because the precise directions of the velocities are unknown. This is comparable with the issue of the first approach, for which the atom positions during the vibration are unknown.

However, the current approach did prove that the vibrational motion is correctly described by adding the vibrational velocities. Furthermore, these velocities are directly calculated from the vibrational energy, which is a more efficient procedure than stepwise changing the atom coordinates until the correct (potential) vibrational energy is finally reached. Therefore, adding the vibrational energy to the kinetic energy instead of the potential energy is the most suitable option.

### 6.3.3. Calculation of the vibrational kinetic velocities by using the normal coordinates

Now, the main issue to solve is to obtain more information about the directions of the vibrational modes. This information is provided by the normal coordinates of a vibrational mode, which describe the position of each atom in a vibrational mode, away from its equilibrium position. In this section, it is first described how the normal coordinates are calculated. Then the normal coordinates of $CH_4$ are summarized before deriving the link between the normal coordinates and the vibrational kinetic velocities. Finally, a correction factor is introduced to keep the center of mass velocity equal to zero.

a) Calculating the normal coordinates

The normal coordinates are the eigenvectors obtained by diagonalization of the mass-weighted Hessian matrix, also known as the matrix of force

constants. This matrix is obtained by considering the vibrational motion as a harmonic oscillator. Before turning to the vibrational motion of a molecule, we first start with a simple harmonic oscillator. For such a system, the force restoring the extension *x* is given by Hook's law:

$$\mathrm{F} = -\mathrm{k} \cdot \mathrm{x} \tag{6.16}$$

In MD simulations, the force constant *k* is the second derivative of the potential energy with respect to position as shown in equation 6.17.

$$\mathrm{k} = \left(\frac{\mathrm{d}^2\mathrm{V}}{\mathrm{dx}^2}\right)_{\mathrm{c}} \tag{6.17}$$

Furthermore, the force in equation 6.16 can be inserted in Newton's second law of motion.

$$-\mathrm{k} \cdot \mathrm{x} = \mathrm{F} = \mathrm{m} \cdot \mathrm{a} \tag{6.18}$$

The acceleration *a* is equal to the second derivative of the position with respect to time. The position during the harmonic oscillation is determined as follows:

$$\mathrm{x(t)} = \mathrm{A} \cdot \sin(2\pi\nu\mathrm{t}) \tag{6.19}$$

Therefore, the acceleration is equal to:

$$\mathrm{a} = \frac{\mathrm{d}^2\mathrm{x}}{\mathrm{dt}^2} = -4\pi^2\nu^2 \cdot \mathrm{A} \cdot \sin(2\pi\nu\mathrm{t}) = -4\pi^2\nu^2 x \tag{6.20}$$

Substituting this formula of *a* into equation 6.18 gives:

$$-\mathrm{k} \cdot \mathrm{x} = -m \cdot 4\pi^2\nu^2 x \tag{6.21}$$

This formula is now used in the calculation of the normal modes of a molecule. For a molecule with *na* atoms, there is not one force constant but a total of (3na)x(3na) force constants. For example, the force constant $\mathrm{k}_{\mathrm{xy}}^{12}$, see equation 6.22, represents the change of the force on atom 1 in the *x* direction due to the movement of atom 2 in the *y* direction.

$$\left(\frac{\partial^2 \mathrm{V}}{\partial \mathrm{x}_1 \, \partial \mathrm{y}_2}\right)_{\mathrm{c}} = \mathrm{k}_{\mathrm{xy}}^{12} \tag{6.22}$$

In total, for a molecule with *na* atoms, the force on atom 1 in the *x* direction is influenced by the movement of *na* atoms, in three directions. Thus, there are *3·na* force constants for describing the total change of the force on atom 1 in the *x* direction. Doing this for all *na* atoms in the three directions, results in the (3na)x(3na) matrix of force constants, i.e. the Hessian matrix, which is shown in Figure 6.6.

$$\begin{bmatrix} \mathrm{k}_{\mathrm{xx}}^{11} & \mathrm{k}_{\mathrm{xy}}^{11} & \mathrm{k}_{\mathrm{xz}}^{11} & \mathrm{k}_{\mathrm{xx}}^{12} & \cdots & \mathrm{k}_{\mathrm{xz}}^{1,\mathrm{na}} \\ \mathrm{k}_{\mathrm{yx}}^{11} & \mathrm{k}_{\mathrm{yy}}^{11} & \mathrm{k}_{\mathrm{xz}}^{11} & & & \vdots \\ \mathrm{k}_{\mathrm{zx}}^{11} & \mathrm{k}_{\mathrm{zy}}^{11} & \vdots & \ddots & & \vdots \\ \mathrm{k}_{\mathrm{xx}}^{21} & \mathrm{k}_{\mathrm{xy}}^{21} & \vdots & & \ddots & \vdots \\ \vdots & \vdots & \vdots & & & \vdots \\ \mathrm{k}_{\mathrm{zx}}^{\mathrm{na},1} & \mathrm{k}_{\mathrm{zy}}^{\mathrm{na},1} & \mathrm{k}_{\mathrm{zz}}^{\mathrm{na},1} & \cdots & \cdots & \mathrm{k}_{\mathrm{zz}}^{\mathrm{na,na}} \end{bmatrix}$$

**Figure 6.6:** Representation of the Hessian matrix for a molecule with *na* atoms.

Combining all these force constants with equation 6.21 gives 3 *na* equations to describe the vibrational motion. For example, equation 6.23 describes the motion of atom 1 in the *x* direction:

$$-4\pi^2\nu^2 m_1 x_1 = -\mathrm{k}_{\mathrm{xx}}^{11} x_1 - \mathrm{k}_{\mathrm{xy}}^{11} y_1 - \mathrm{k}_{\mathrm{xz}}^{11} z_1 - \mathrm{k}_{\mathrm{xx}}^{12} x_2 - \cdots - \mathrm{k}_{\mathrm{xz}}^{1,\mathrm{na}} z_{na} \tag{6.23}$$

In this equation, $x_1$ denotes the extension in the *x* direction of atom 1. All 3 *na* equations should be solved to obtain the values for $x_1$, $x_2$, …, $z_{na}$. However, the matrix is not symmetric, and therefore diagonalization is not always possible. This issue is solved by using mass-weighted coordinates and force constants:

$$x'_1 = x_1 \cdot \sqrt{m_1} \quad \text{and} \quad \mathrm{k'}_{\mathrm{xy}}^{12} = \frac{\mathrm{k}_{\mathrm{xy}}^{12}}{\sqrt{m_1} \cdot \sqrt{m_2}} \tag{6.24}$$

Now, the mass-weighted Hessian matrix is a symmetric matrix and the eigenvalues and eigenvectors can be calculated. The eigenvectors are the mass-weighted normal coordinates, thus the normal coordinates can be

determined. Furthermore, the eigenvalues are used to calculate the vibrational frequencies of the vibrational modes. The eigenvalues correspond to $k/m$, and equation 6.21 can be written as a function of this value:

$$\nu^2 = \frac{k}{4\pi^2 \cdot m} \Rightarrow \nu = \frac{1}{2\pi} \cdot \sqrt{\frac{k}{m}} \tag{6.25}$$

With this formula, the vibrational frequencies are calculated from the eigenvalues.

b) Normal coordinates of $CH_4$

In case of $CH_4$, the Hessian is a 15x15 matrix, and calculating the eigenvectors of this matrix results in 15 sets of normal coordinates. Besides the 9 sets of normal coordinates that describe the vibrational modes, there are also 3 for the translational and 3 for the rotational motion of the molecule. The sets of normal coordinates of $CH_4$ calculated with ReaxFF are shown in this section. The normal coordinates are calculated for a $CH_4$ molecule with an orientation as illustrated in Figure 6.7.

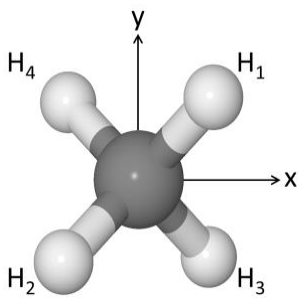


**Figure 6.7:** Orientation of the $CH_4$ molecule for which the normal coordinates are calculated.

The following two sets of normal coordinates represent translational and rotational motion, respectively:

$$\begin{matrix} \mathrm{C} \\ \mathrm{H_1} \\ \mathrm{H_2} \\ \mathrm{H_3} \\ \mathrm{H_4} \end{matrix} \begin{pmatrix} -0.05811 & 0.15189 & 0.18955 \\ -0.05811 & 0.15189 & 0.18955 \\ -0.05811 & 0.15189 & 0.18955 \\ -0.05811 & 0.15189 & 0.18955 \\ -0.05811 & 0.15189 & 0.18955 \end{pmatrix} \quad \begin{pmatrix} 0.00000 & 0.00000 & 0.00000 \\ -0.26579 & 0.17446 & 0.09133 \\ -0.31392 & 0.22259 & -0.09133 \\ 0.26579 & -0.22259 & 0.48838 \\ 0.31392 & -0.17446 & -0.48838 \end{pmatrix}$$

Clearly, the left set of normal coordinates is for the molecular translation of $CH_4$, since all atoms are moved in the same direction to the same extent. The rotational motion of the right set is characterized by the non-moving C-atom, while the H-atoms have two different absolute values in each direction. Furthermore, the sum of the normal coordinates in each direction is zero, indicating that $\nu_{COM}$ is equal to zero. For both degrees of freedom, there are two additional sets of normal coordinates. These are similar to the ones shown above, and therefore not shown.

Our main interest is the normal coordinates of the vibrational modes. The following normal coordinates represent the symmetric C-H stretch vibration, $\nu_1$:

$$\begin{pmatrix} 0.00000 & 0.00000 & 0.00000 \\ 0.28753 & 0.28753 & 0.28753 \\ -0.28753 & -0.28753 & 0.28753 \\ 0.28753 & -0.28753 & -0.28753 \\ -0.28753 & 0.28753 & -0.28753 \end{pmatrix}$$

As discussed earlier, the magnitude of the velocity is the same for each H-atom in each direction, which is also observed in the normal coordinates of this vibrational mode.

The normal coordinates for the double degenerate symmetric bend vibration, $\nu_2$, are shown below:

$$\begin{pmatrix} 0.00000 & 0.00000 & 0.00000 \\ -0.27699 & 0.39631 & -0.11932 \\ 0.27699 & -0.39631 & -0.11932 \\ -0.27699 & -0.39631 & 0.11932 \\ 0.27699 & 0.39631 & 0.11932 \end{pmatrix} \quad \begin{pmatrix} 0.00000 & 0.00000 & 0.00000 \\ 0.29770 & 0.09103 & -0.38872 \\ -0.29770 & -0.09103 & -0.38872 \\ 0.29770 & -0.09103 & 0.38872 \\ -0.29770 & 0.09103 & 0.38872 \end{pmatrix}$$

The C-atom does not move, because of the symmetric motion of the H-atoms. Furthermore, $\nu_{COM}$ will also be equal to zero, as the mass-weighted sum of the normal coordinates in each direction is equal to zero.

There are three sets of normal coordinates for the antisymmetric C-H stretch vibration, $\nu_3$:

$$\begin{pmatrix} 0.10080 & -0.00372 & 0.00808 \\ -0.31085 & -0.25992 & -0.26567 \\ -0.27063 & -0.21970 & 0.21757 \\ -0.28913 & 0.24182 & 0.23607 \\ -0.32935 & 0.28204 & -0.28416 \end{pmatrix} \quad \begin{pmatrix} -0.00396 & -0.10107 & 0.00291 \\ 0.25610 & 0.30342 & 0.25275 \\ 0.27056 & 0.31789 & -0.27005 \\ -0.23253 & 0.28371 & 0.23304 \\ -0.24700 & 0.29818 & -0.25034 \end{pmatrix}$$

$$\begin{pmatrix} 0.00796 & -0.00321 & -0.10082 \\ 0.23523 & 0.24067 & 0.28824 \\ -0.26664 & -0.26120 & 0.31190 \\ -0.28263 & 0.28031 & 0.32788 \\ 0.21924 & -0.22156 & 0.27226 \end{pmatrix}$$

The slight deviation between the normal coordinates of the H-atoms indicates that there will be differences between all the C-H bond lengths and H-C-H bond angles. Furthermore, the C-atom also moves, which normally should keep $v_{COM}$ equal to zero. However, the mass-weighted sum of the normal coordinates in each direction is not equal to zero. For instance, for the *x* direction of the first normal coordinates set this sum is:

$$\sum_{i=1}^{na} m_i \cdot nc_{i,x} = 0.00115$$

This is only slightly higher than zero, but after linking the normal coordinates to the vibrational velocities (see below), this leads to a slight translational motion of $CH_4$. It is unclear if this translational motion is due to errors within ReaxFF or due to rounding errors in the calculation of the normal coordinates. In any case, this type of motion is unwanted and therefore, a correction factor will be introduced to keep $v_{COM}$ equal to zero. This is thoroughly discussed in §6.3.3.d.

Finally, the three sets of normal coordinates that represent the antisymmetric bending vibration, $\nu_4$, are shown on the next page.

$$\begin{pmatrix} -0.04347 & 0.06011 & -0.07223 \\ 0.10057 & -0.45394 & 0.25451 \\ 0.44398 & -0.11053 & 0.17540 \\ 0.15818 & -0.24725 & 0.46120 \\ -0.18523 & 0.09616 & -0.03129 \end{pmatrix} \quad \begin{pmatrix} -0.05110 & -0.08190 & -0.03741 \\ -0.13155 & 0.03334 & -0.20489 \\ 0.04630 & 0.21120 & 0.42754 \\ 0.43574 & 0.27633 & 0.03810 \\ 0.25789 & 0.45418 & 0.18455 \end{pmatrix}$$

$$\begin{pmatrix} -0.07885 & 0.01995 & 0.06406 \\ 0.43439 & -0.09454 & -0.33070 \\ 0.12981 & -0.39912 & -0.05060 \\ 0.03498 & 0.28039 & 0.04423 \\ 0.33956 & -0.02419 & -0.42553 \end{pmatrix}$$

This vibrational mode has the most complex motion. Again, a correction will be required to keep $v_{COM}$ fixed at zero (see §6.3.3.d).

The eigenvalues of the mass-weighted Hessian matrix are used to derive the vibrational frequencies of the vibrational modes, as mentioned previously. The vibrational frequencies obtained with ReaxFF are compared with literature [113] in Table 6.1. The shown energy difference is for the fundamental of each vibration.

**Table 6.1:** Comparison between the calculated vibrational frequencies and values found in literature [113]. The energy difference is for the fundamental of the vibration.

| vibr. mode | $\nu_{ReaxFF}$ ($cm^{-1}$) | $\nu_{lit.}$ ($cm^{-1}$) | $E_{ReaxFF} - E_{lit.}$ (kJ/mol) |
|---|---|---|---|
| $\nu_1$ | 3211 | 2916 | 5.29 |
| $\nu_2$ | 2136 | 1533 | 10.82 |
| $\nu_3$ | 3260 | 3019 | 4.32 |
| $\nu_4$ | 1895 | 1311 | 10.48 |

The values shown above indicate that ReaxFF correctly reproduces the order of frequencies in terms of their magnitude, but also that there is a significant difference in absolute values between calculated values and literature values. The effect of this difference is further discussed in Chapter 7.

c) Link between the normal coordinates and the vibrational kinetic velocities

The total vibrational energy of equation 6.5 can be subdivided into multiple terms, in which each term represents the vibrational energy of the movement of atom *i* in direction *j* (j = x, y, z):

$$E_{vibr} = \sum_{i=1}^{na} E_{vibr_{i,j}} \tag{6.26}$$

$$E_{vibr_{i,j}} = \frac{1}{2} m_i v_{i,j}^2 \tag{6.27}$$

Each of these partial vibrational energies is related to the total vibrational energy as follows:

$$E_{vibr_{i,j}} = E_{vibr} \cdot f_{i,j} \tag{6.28}$$

Here, $f_{i,j}$ is a relative contribution factor for the vibrational energy of atom *i* in the *j* direction. Next, equations 6.27 and 6.28 are combined to calculate the velocity $v_{i,j}$:

$$v_{i,j} = \sqrt{\frac{2 \cdot E_{vibr}}{m_i} \cdot f_{i,j}} \tag{6.29}$$

With this equation, the velocity can be calculated if $f_{i,j}$ is known. This factor will be determined from the normal coordinates.

For a molecule with *na* atoms, a set of normal coordinates has the following structure:

$$\begin{pmatrix} nc_{1,x} & nc_{1,y} & nc_{1,z} \\ nc_{2,x} & nc_{2,y} & nc_{2,z} \\ \vdots & \vdots & \vdots \\ nc_{na,x} & nc_{na,y} & nc_{na,z} \end{pmatrix}$$

The sum of all the normal coordinates, multiplied with the corresponding atomic masses, $NC_T$, is calculated with equation 6.30.

$$NC_T = \sum_{i=1}^{na} m_i \cdot \left(|nc_{i,x}| + |nc_{i,y}| + |nc_{i,z}|\right) \tag{6.30}$$

Each term of this sum is related to $NC_T$ by another relative contribution factor $f_{i,j}^*$:

$$m_i \cdot |nc_{i,j}| = NC_T \cdot f_{i,j}^* \tag{6.31}$$

This calculation is similar to the calculation of the partial vibrational energy in equation 6.28. Furthermore, the partial vibrational energy is written as a function of the velocity, while equation 6.31 is written as a function of the normal coordinates. The velocity of an atom is the derivative of the position of the atom with respect to time. If the atomic coordinates are multiplied with a constant factor, such as $f_{i,j}^*$, this factor is retained over differentiation of the product with respect to time. Therefore, the factor used in equation 6.29 (velocity formula) and 6.31 (coordinates formula) is the same.

$$f_{i,j} = f_{i,j}^* = \frac{m_i \cdot |nc_{i,j}|}{NC_T} \tag{6.32}$$

Substituting this formula for $f_{i,j}$ in equation 6.29 gives the following equation for calculating the vibrational velocity:

$$v_{i,j} = \sqrt{\frac{2 \cdot E_{vibr}}{m_i} \cdot \frac{m_i \cdot |nc_{i,j}|}{NC_T}} \tag{6.33}$$

This is reduced to:

$$v_{i,j} = \sqrt{\frac{2 \cdot E_{vibr} \cdot \left|nc_{i_j}\right|}{NC_T}} \tag{6.34}$$

The last adjustment that needs to be made is to give the velocity $v_{i,j}$ the same sign as $nc_{i,j}$, since this gives the correct direction to the velocity.

With equation 6.34, it is possible to calculate the vibrational velocities of all atoms, for each vibrational mode, for a specific vibrational energy, once the

normal coordinates are known. This is illustrated in Figure 6.8, in which the initial motions of the four vibrational modes of $CH_4$, calculated with ReaxFF, are shown. This method can also be used for other molecules, since normal coordinates can be determined as described in §6.3.3.a.

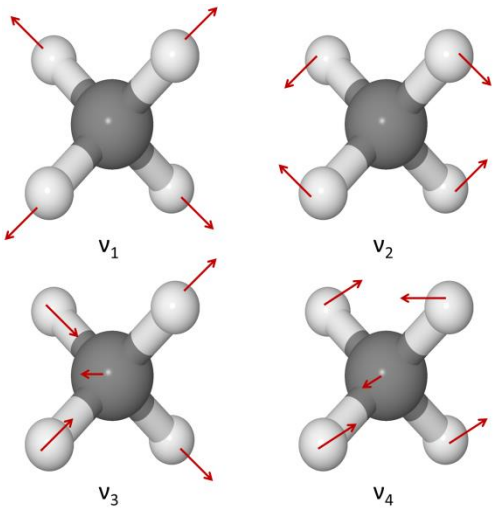


**Figure 6.8:** Motions of the vibrational modes of $CH_4$ obtained with ReaxFF.

d) Velocity correction

It was mentioned in §6.3.3.b that the center of mass velocity is not equal to zero for the antisymmetric vibrational modes. As a consequence, the added energy is not fully allocated to vibrational motion, but also to translational motion. In order to prevent this, the velocities of the C-atom are corrected to have a $v_{COM}$ equal to zero.

The center of mass velocity in direction *j* is calculated as follows:

$$v_{COM_j} = \frac{\sum_{i=1}^{na} m_i \cdot v_{i,j}}{\sum_{i=1}^{na} m_i} = 0 \qquad (6.35)$$

If $v_{COM_j}$ is equal to zero, the sum over all the atomic masses (i.e. the denominator of the division) can be neglected in equation 6.35. The equation is then rearranged to determine $v'_{C_j}$, which is the new velocity of the C-atom in the *j* direction.

$$m_C v'_{C_j} + m_H \sum_{i=1}^{nH} v_{H_{i,j}} = 0 \Rightarrow v'_{C_j} = -\frac{m_H}{m_C} \sum_{i=1}^{nH} v_{H_{i,j}} \quad (6.36)$$

With this new velocity, $v'_{C_j}$, the C-atom moves in such a way that $v_{COM_j}$ is equal to zero. However, this new velocity also leads to a new value for the added vibrational energy:

$$E'_{vibr} = \frac{1}{2} m_C v'^2_{C_t} + \sum_{i=1}^{nH} \frac{1}{2} m_H v^2_{H_{i,t}} \quad (6.37)$$

This $E'_{vibr}$ does not correspond to the vibrational energy calculated from the vibrational frequency (see equation 6.3). Therefore, the correction factor $f_2$ is introduced:

$$f_2 = \sqrt{\frac{E_{vibr}}{E'_{vibr}}} \quad (6.38)$$

Finally, all the velocities are rescaled with this factor to obtain the correct $E_{vibr}$ and a $v_{COM_j}$ of zero:

$$v'_{i,j} = f_2 \cdot v_{i,j} \quad (6.39)$$

## 6.4. Stability of the vibrational motions in the MD simulations

In the previous section, the vibrational motions of the first approaches were simulated for 6.25 ps, i.e. the simulation time of one impact. In this section, the simulation time is increased to 50 ps, to study the long-term stability of the vibrational motions.

### 6.4.1. Symmetric C-H stretch

In the symmetric C-H stretch vibrational mode, all the C-H bonds are equal for the entire vibration. The difference between the bond length of $r_{CH_1}$ and $r_{CH_2}$ should be equal to zero. This is initially the case, as shown in Figure 6.9.

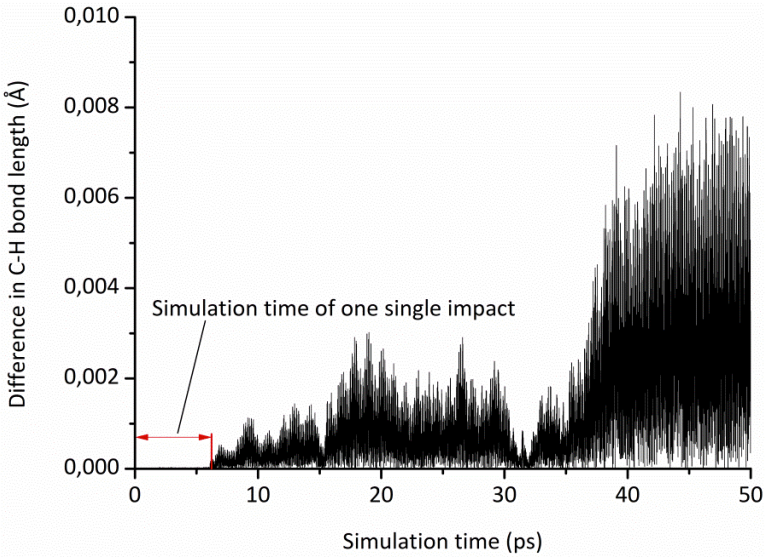


**Figure 6.9:** Difference in C-H bond length between $r_{CH_1}$ and $r_{CH_2}$ in the symmetric C-H stretch vibration as a function of simulation time.

However, small differences start to occur after about 7 ps. The deviation then increases towards 0.008 Å at the end of the simulation, which is still acceptable. More importantly, for the simulation time of a single impact, no deviation is observed. The same conclusions are made for the difference in the H-C-H bond angles (see Figure 6.10). Again, the deviation first occurs only after 7 ps, and the maximum deviation remains lower than ± 0.3°.

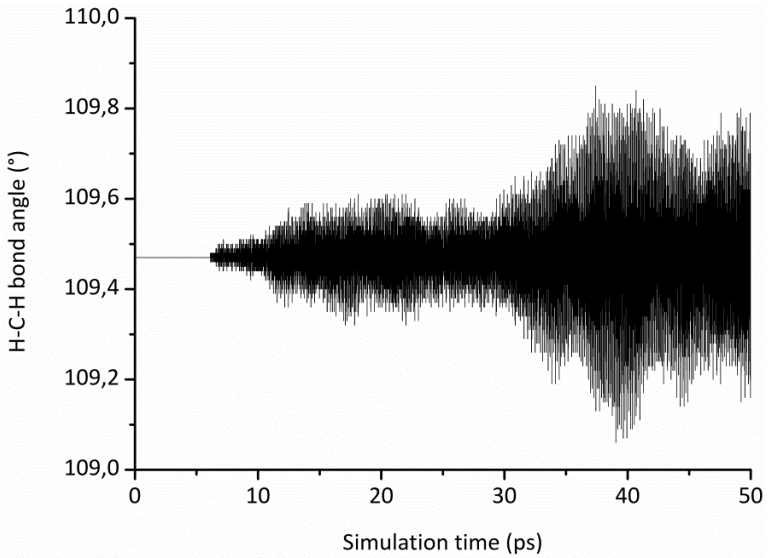


**Figure 6.10:** H-C-H bond angle in the symmetric C-H stretch vibration as a function of simulation time.

### 6.4.2. Symmetric bend

In the symmetric bend vibration, the four C-H bond lengths are equal. This is maintained for the first part of the simulation, but then the difference between the bond lengths increases rapidly, as shown in Figure 6.11.

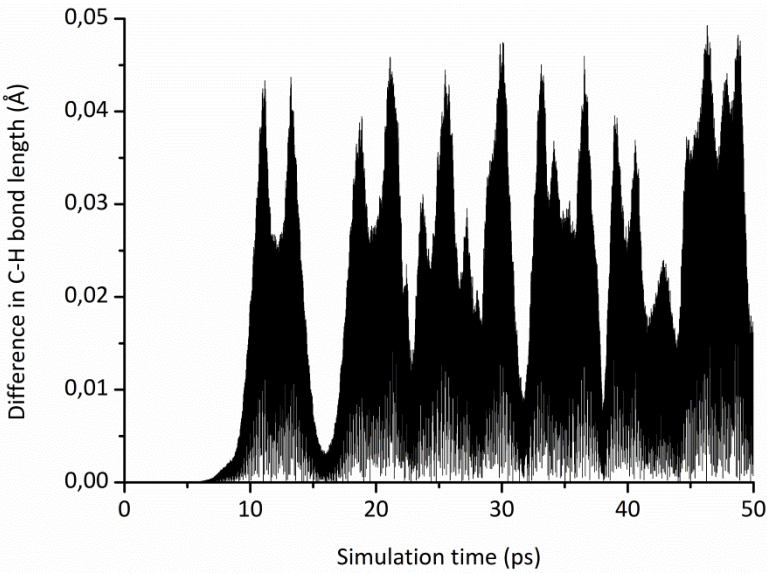


**Figure 6.11:** Difference in C-H bond length between $r_{CH_1}$ and $r_{CH_2}$ in the symmetric bend vibration as a function of simulation time.

Furthermore, the difference is much larger compared to the one observed during the symmetric C-H stretch, i.e. 0.045 Å against 0.008 Å, respectively. Again, the same is observed for the bond angles. The six bond angles are divided in three sets of two, in which the bond angles have the same value (see Table 6.2). Thus, there are a total of three different bond angles at a certain simulation time.

Initially, there is no deviation between the bond angles in each of the three sets. However, after about 8 ps, a deviation develops, with a maximum of 1.8° over the entire simulation time (see Figure 6.12).

**Table 6.2:** H-C-H bond angles in the symmetric bend vibration after 0.01 ps and 6.25 ps (see Figure 6.7 or first image of Figure 6.13 for the numbering of the atoms).

| **bond angle (∠) of** | **∠ after 0.01 ps (°)** | **∠ after 6.25 ps (°)** |
|---|---|---|
| $H_1$-C-$H_2$ | 105.50 | 110.37 |
| $H_1$-C-$H_3$ | 102.41 | 107.43 |
| $H_1$-C-$H_4$ | 121.18 | 110.64 |
| $H_2$-C-$H_3$ | 121.18 | 110.63 |
| $H_2$-C-$H_4$ | 102.41 | 107.43 |
| $H_3$-C-$H_4$ | 105.50 | 110.37 |

It is important to notice that both symmetric vibrational modes are stable for the simulation time of a single impact, i.e. 6.25 ps. Afterwards, a deviation in the vibrational motion develops. From the moment that such a deviation occurs, it propagates further as a function of the simulation time. The symmetric motions are less complex than the antisymmetric motions, so it is most likely that deviations occur at a faster rate for the latter. Because of this, forced corrections on the initial velocities might be necessary to obtain a stable vibration for at least 6.25 ps.

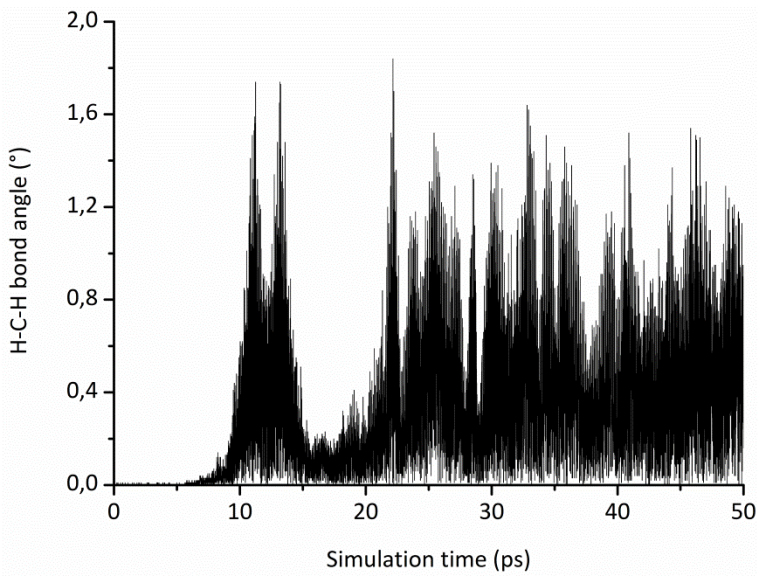


**Figure 6.12:** Difference between the bond angles of ∠$H_1$-C-$H_3$ and ∠$H_2$-C-$H_4$ in the symmetric bend vibration as a function of simulation time.

### 6.4.3. Antisymmetric C-H stretch

a) Uncorrected vibrational motion

In the antisymmetric C-H stretch vibration, the H-atoms move in pairs, i.e. when two C-H bonds elongate simultaneously, the other two C-H bonds shorten, and vice versa. However, as already mentioned in §6.3.3.b, none of the C-H bonds lengths are equal to each other at any given simulation time. The difference in the C-H bond length between the first pair of H-atoms is about 0.01 Å, and that of the second pair 0.04 Å. In contrast to the symmetric vibrational modes, this difference already occurs in the beginning of the simulation.

The H-C-H bond angles are expected to remain close to 109.47°, since it is a stretching vibration. Remarkably, four of the six H-C-H bond angles only vary slightly, while the other two have a larger variation, as shown in Table 6.3.

**Table 6.3:** Minimum and maximum H-C-H bond angles in the antisymmetric C-H stretch vibration (see Figure 6.7 or first image of Figure 6.13 for the numbering of the atoms).

| bond angle ($\angle$) of | minimum angle (°) | maximum angle (°) |
|---|---|---|
| $H_1$-C-$H_2$ | 108.90 | 110.00 |
| $H_1$-C-$H_3$ | 108.91 | 109.98 |
| $H_1$-C-$H_4$ | 106.46 | 113.07 |
| $H_2$-C-$H_3$ | 106.49 | 113.07 |
| $H_2$-C-$H_4$ | 108.91 | 109.98 |
| $H_3$-C-$H_4$ | 108.91 | 109.98 |

The differences in the C-H bond lengths and the H-C-H bond angles are part of the antisymmetric motion. These differences already occur at the start of the simulation, but they do not increase, i.e., there is no deviation in the vibrational motion. Therefore, this vibrational mode can be used in the single impacts. However, rotation of the $CH_4$ molecule is observed during the simulation, as illustrated in Figure 6.13. Even after 6.25 ps, the rotation is

already observed, and this can be an issue when studying e.g. processes involving this vibrational mode.

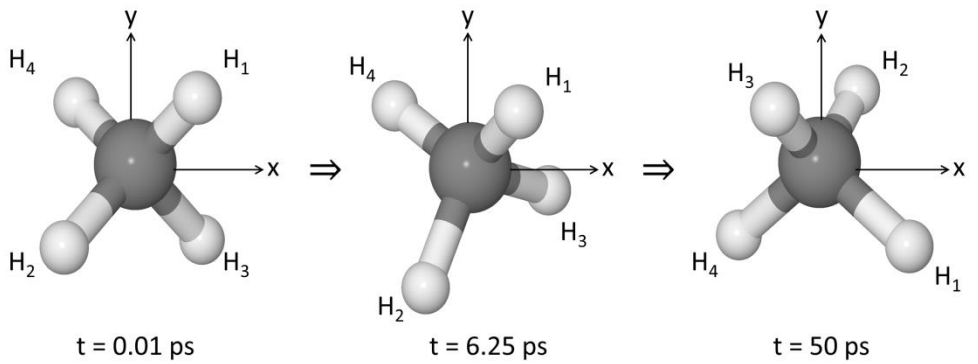


**Figure 6.13:** Orientation of the $CH_4$ molecule in the antisymmetric vibrational mode after simulation times of 0.01 ps, 6.25 ps and 50 ps.

Thus, the added energy is distributed over a vibrational and a rotational component. Even though the influence of the rotational component on the reactivity is expected to be low, a corrected vibration without rotational motion is desired.

b) Corrected vibrational motion

In order to remove the rotational motion, the normal coordinates of the H-atoms are replaced by the average value of these normal coordinates. This gives the following set:

$$\begin{pmatrix} -0.00396 & -0.10107 & 0.00291 \\ 0.26795 & 0.26795 & 0.26795 \\ 0.26795 & 0.26795 & -0.26795 \\ -0.26795 & 0.26795 & 0.26795 \\ -0.26795 & 0.26795 & -0.26795 \end{pmatrix}$$

The normal coordinates of the C-atom are not adjusted. This is automatically done in the computational code to obtain a $v_{COM}$ of zero (see §6.3.3.d).

There is no rotational motion associated with this set of normal coordinates. The C-H bond lengths of the paired H-atoms are now equal, with a maximum difference of 0.00015 Å, even after 50 ps (see Figure 6.14). The correction of

the normal coordinates does not influence the H-C-H bond angles, since the same variation in these angles is observed compared to the uncorrected vibration (cf. Table 6.3).

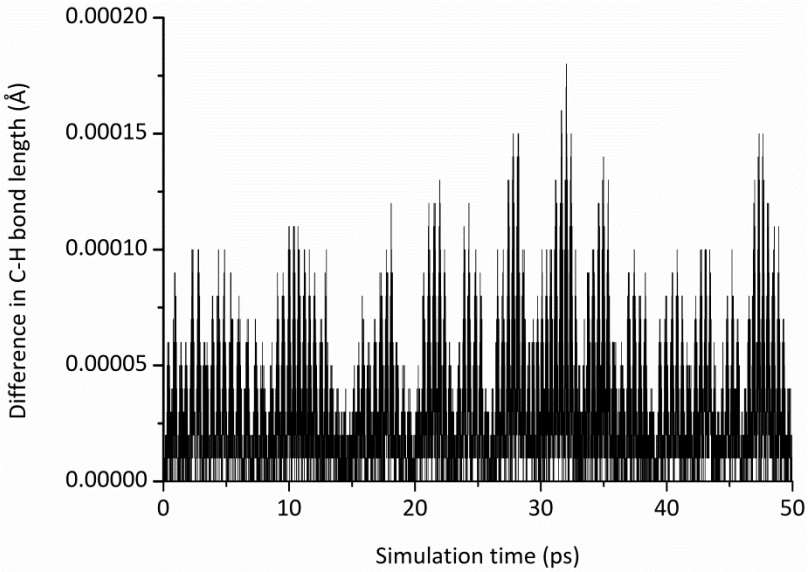


**Figure 6.14:** Difference in C-H bond length between $r_{CH_2}$ and $r_{CH_3}$ in the corrected antisymmetric C-H stretch vibration as a function of simulation time.

To summarize, the main difference between the uncorrected and corrected vibration is the C-H bond length, which is equal for the paired H-atoms in the latter case. The difference between the corrected and uncorrected vibrational motion on the reactivity is discussed in Chapter 7.

### 6.4.4. Antisymmetric bend

The last vibrational mode is the most complex to describe. In contrast to the other vibrations, no links between different C-H bond lengths or H-C-H bond angles is found. From the start of the simulation, each of these has a different value.

More importantly, there is also rotational motion observed during the simulations. However, due to the complexity of this vibrational mode, no corrections are made to the normal coordinates. The reactivity of this

vibrational mode will be studied in the next chapter, keeping into account that a part of the added energy is converted to rotational motion.

## 6.5. Conclusion

The addition of the motions of vibrationally excited $CH_4$ to reactive MD simulations was investigated in this chapter.

The first approach consisted of increasing the initial potential energy of the molecule, resulting in vibrational motion, while the total added energy is maintained. However, the exact atom positions of the vibrational mode are required, and this is only known for the symmetric C-H stretch vibration. Furthermore, a trial-and-error based sequence of slightly moving the atoms until the correct energy is obtained should be followed in order to obtain a specific vibrational energy.

As an alternative to the first approach, the vibrational energy can also be added through setting the atomic vibrational velocities. The increased energy is then a part of the kinetic energy at the start of the simulation. This method results in a harmonic oscillation of the C-H bond lengths of $CH_4$ in the symmetric C-H stretch vibration. An additional advantage of this method is that the velocities are calculated to obtain a specific vibrational energy. However, the vibrational velocities can only be directly calculated for the symmetric C-H stretch vibration. Without additional information of the precise directions of the velocities in the other vibrational modes, these modes cannot be described.

This issue is solved by calculating the normal coordinates of the vibrational modes. These describe the position of each atom in a vibrational mode, away from its equilibrium position. The normal coordinates are linked to the vibrational velocities, which makes it possible to describe all vibrational modes, keeping into account the mode specific vibrational energy. For the antisymmetric vibrational modes, the velocities of the C-atom are corrected

to have a center of mass velocity of zero. As a consequence, all the velocities are subsequently rescaled to regain the original vibrational energy.

Both symmetric vibrational modes remain stable for the first 6.25 ps of the simulation. Afterwards, slight deviations in the vibrational motion of the symmetric C-H stretch are observed. This also occurs in the symmetric bend vibration, but the deviations are larger.

The motion of the antisymmetric C-H stretch vibration is maintained during the entire simulation. It is important to notice that there is also rotational motion of the $CH_4$ molecule. This can be removed by correcting the normal coordinates of the H-atoms. This correction does not influence the H-C-H bond angles, in contrast to the C-H bond length, which is now equal for the paired H-atoms.

There is also rotational motion in the simulations of the antisymmetric bend vibration. This is the most complex of the four vibrational modes, and therefore, no corrections to the set of normal coordinates can be made.

The findings of this chapter can be summarized as follows:

- Addition of vibrational energy to the initial potential energy:
    - Induces vibrational motions
    - No harmonic but random oscillation of the C-H bond length
    - Trial-and-error based sequence to obtain specific vibrational energy
    - Only applicable to the symmetric C-H stretch vibration
- Direct calculation of the vibrational kinetic velocities:
    - Harmonic oscillation of the C-H bond length
    - Specific vibrational energy is obtained
    - Only applicable to the symmetric C-H stretch vibration

- Calculation of the vibrational velocities with the normal coordinates:
  - All vibrational modes are described
  - Procedure can also be used for other molecules
  - Correction is required to keep $v_{COM}$ equal to zero
- Stability of the vibrational motions:
  - Symmetric C-H stretch: no deviations in first 6.25 ps
  - Symmetric bending: no deviations in first 6.25 ps
  - Antisymmetric C-H stretch: rotational motion is observed, but this can be corrected
  - Antisymmetric bending: rotational motion is observed, and this cannot be corrected

# Chapter 7:
# Validation of the reactivity of vibrationally excited $CH_4$ in MD simulations

In this chapter, the research on vibrationally excited $CH_4$ introduced in the previous chapter is continued. After having illustrated that the vibrational motion can be described with a classical approach, the objective is now to validate whether the reaction behavior of the vibrational modes is simulated correctly. For this purpose, single impacts of vibrationally excited $CH_4$ on Ni(111) are performed.

Most experimental studies focus on the $\nu_3$ and $3\nu_4$ vibration, while little data is available about the other vibrational states. Hence, this chapter also focuses on these two modes.

It is shown that the reaction behavior does not correspond to reactivity values mentioned in literature. The addition of a correction factor to all vibrational states and the use of the experimental vibrational frequencies increase the accuracy of the simulations for the $\nu_3$, $2\nu_3$ and $3\nu_4$ vibrational states. However, these corrections are insufficient, since the reactivity of the $\nu_1$ state is much lower than predicted. This is caused by the absence of (1) the localization of vibrational energy in the C-H bond that is directed towards the surface, and (2) the non-adiabatic coupling of the vibrational mode to the ground state or lower vibrational states.

## 7.1. Introduction

The reactivity of a vibrationally excited molecule is higher than that of the molecule in the ground state, when both molecules have the same translational energy. However, this does not directly indicate whether vibrational excitation is more efficient or not, because the molecule in the ground state has a lower total energy. If the vibrational energy is added as translational energy to the molecule in the ground state, and this molecule then has a higher reactivity than the vibrationally excited molecule, the excitation is inefficient. Experimentally, the vibrational efficiency of $CH_4$, $\eta_{vibr}$, is calculated by obtaining the adsorption curves of the molecule in both the ground state and the excited state, both as a function of the translational energy [97–103]. The energy difference $\Delta E$ between both curves is determined, as shown in Figure 7.1, and compared with the vibrational energy that is added to the ground state (i.e. $\Delta E_{vibra}$) in order to calculate $\eta_{vibr}$:

$$\eta_{vibr} = \frac{\Delta E}{\Delta E_{vibra}} \tag{7.1}$$

If $\eta_{vibr}$ is greater than 1, it is more beneficial to add energy to the vibrational motion of the molecule. For $\eta_{vibr}$ lower than 1, the highest reactivity is obtained by adding energy to the translational motion.

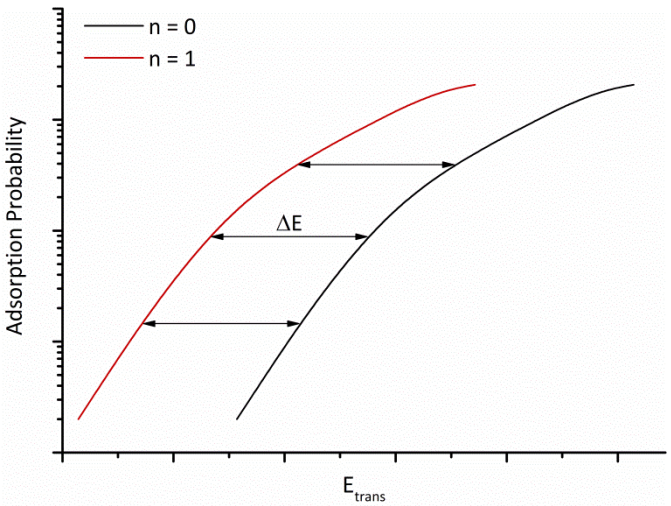


**Figure 7.1:** Representation of the adsorption curves of a molecule in the ground state and vibrationally excited state, with the corresponding energy difference $\Delta E$.

In this chapter, the same procedure will be used to calculate $\eta_{vibr}$ for the different vibrational modes of $CH_4$ on Ni(111), with a surface temperature of 475 K, i.e., the same as used in literature reports. First, the validity of the correction made to the normal coordinates set of $\nu_3$ to prevent rotation of $CH_4$ is investigated.

Subsequently, the adsorption curves of $CH_4$ excited to the fundamental and first overtone of the antisymmetric C-H stretch vibration are calculated. This is done by performing single impacts of the excited $CH_4$ molecule at different translational energies. As mentioned in Chapter 1, most data in literature deals with the $\nu_3$ (and $3\nu_4$) vibration (cf. Table 1.2) [98]. Therefore, $\eta_{vibr}$ calculated in our simulations can be compared with these data. If the reaction behavior of the $\nu_3$ vibration in the MD simulations is similar to the experimental data, an attempt can be made to use the simulations to predict the reactivity of the other vibrational modes. However, it is found that there is a discrepancy between the values obtained in the MD simulations and those found in literature.

Therefore, the final part of this chapter is focused on investigating possible solutions for this discrepancy.

## 7.2. Description of the simulations

The setup for the single impacts is in part similar to the one used in Chapters 3 and 5. Again, the molecule is added to the system at a *z* position of 10 Å above the top layer of the pristine Ni(111) surface. This surface is first equilibrated at 475 K, employing the Bussi thermostat with a coupling constant of 100 fs. Periodic boundary conditions are applied in the {x,y} directions.

In contrast to the previously described single impact simulations, the initial velocity of the added molecule is not randomly generated. First, the vibrational velocities corresponding to the desired vibrational state are added.

Then, the molecule is rotated randomly. The velocities are recalculated with this rotational matrix, so that the vibrational motion is maintained. Finally, translational energy is added to the molecule as a velocity in the *z* direction, towards the nickel surface. Therefore, each impact consists of a randomly rotated $CH_4$ molecule, excited to a certain vibrational state, moving straight to the surface.

In order to maintain the vibrational motion, the impacts are performed in the NVE ensemble. Each impact of each case, i.e., for a certain vibrational state and translational energy, is followed for 6.25 ps and repeated 5000 up to 10000 times. This is significantly higher than the number of single impacts we performed before, because the adsorption probabilities at low translational energies are quite low, i.e., in the order of 1 %. Therefore, a reliable result requires many impacts.

## 7.3. Results and Discussion

### 7.3.1. Corrected vs uncorrected antisymmetric C-H stretch vibration

In the previous chapter, the normal coordinates set of the antisymmetric C-H stretch vibration was corrected to remove the rotational motion of the molecule. In this section, the influence of this correction is determined. This is of importance since for the $\nu_4$ vibration, rotation is also observed. If the results for the corrected and uncorrected $\nu_3$ vibration are similar, we can conclude that:

1. the rotational motion has little effect, and both the corrected and the uncorrected normal coordinates set can be used;
2. simulations of the $\nu_4$ vibration also can be performed, even if there is rotational motion.

There is almost no difference between the corrected and uncorrected normal coordinates set, as shown in Table 7.1.

**Table 7.1:** Adsorption probability of $CH_4$ excited in the corrected and uncorrected $\nu_3$ state as a function of $E_{trans}$.

| $E_{trans}$ (kJ/mol) | Adsorption probability of corrected $\nu_3$ | Adsorption probability of uncorrected $\nu_3$ |
|---|---|---|
| 50 | 0.0071 | 0.0070 |
| 75 | 0.0760 | 0.0815 |
| 100 | 0.3018 | 0.2982 |
| 125 | 0.5547 | 0.5588 |

As expected, the rotational motion has no significant effect on the reactivity. Therefore, impacts of $CH_4$ excited in the $3\nu_4$ vibrational state can be performed.

### 7.3.2. Validation of the reactivity of the antisymmetric C-H stretch vibration

In order to assess the accuracy of the results obtained with the MD simulations, these results are compared with data found in literature. This is first done for the $\nu_3$ vibration, and the results are shown in Figure 7.2 [102]. The lowest $E_{trans}$ that is used in our simulations is 25 kJ/mol, but no adsorptions are observed for this energy. Experimentally, hardly any adsorptions occur at this $E_{trans}$, so more than 10000 simulations are necessary.

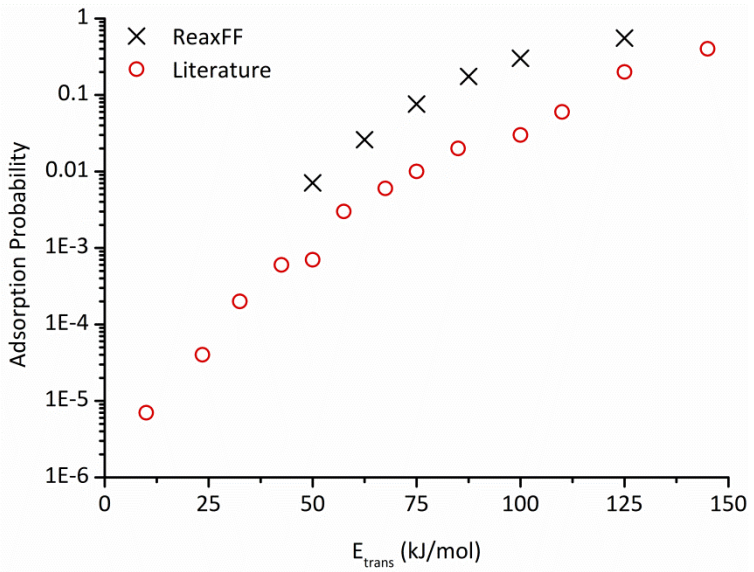


**Figure 7.2:** Adsorption curves of $CH_4$, in the $\nu_3$ vibrational state, on Ni(111) obtained with ReaxFF and found in literature [102], as a function of $E_{trans}$.

The results obtained with the MD simulations are initially a factor of 7 to 10 higher than the experimental data [102]. Only at $E_{trans}$ of 125 kJ/mol, when the maximum adsorption probability is almost reached, the difference is smaller, i.e., a factor of 2.5. However, it should be noted that the shape of both curves is similar.

In order to determine $\eta_{vibr}$, impacts of non-excited $CH_4$ are performed, as a function of $E_{trans}$. Comparison of the results with experimental data indicates that the simulation again predicts higher adsorption probabilities, as shown in Figure 7.3 [102]. The difference varies between a factor of 8 to 25, while the shape of both curves is similar.

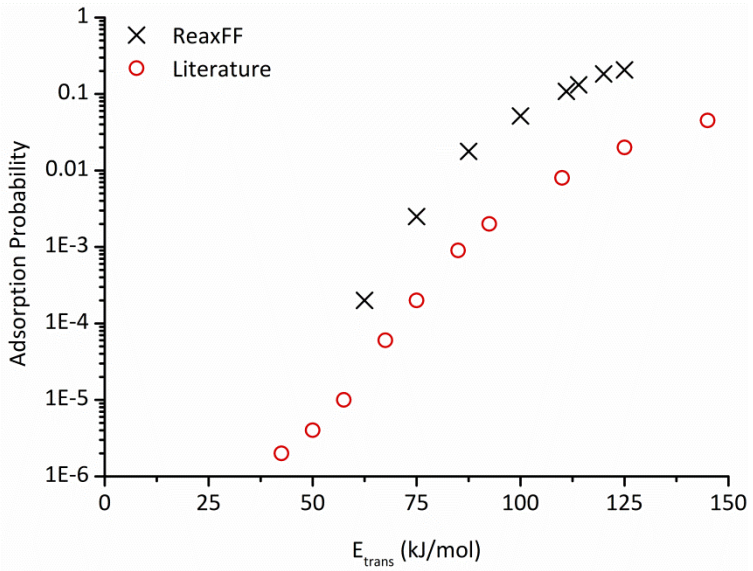


**Figure 7.3:** Adsorption curves of $CH_4$, in the ground state, on Ni(111) obtained with ReaxFF and found in literature [102], as a function of $E_{trans}$.

It is clear that the simulations cannot be used for an exact measurement of the adsorption probability. However, of greater importance is the value found for $\eta_{vibr}$. If the same energy shift ($\Delta E$) between the curve of the ground state and vibrationally excited state is found in both the simulations and experiments, $\eta_{vibr}$ can be calculated correctly. To clarify this, both calculated curves are shown together in Figure 7.4.

The horizontal distance between the curves remains almost equal as a function of $E_{trans}$, i.e., $\Delta E$ is nearly constant. The energy shift between both curves varies between 30 kJ/mol (dashed arrows) and 32 kJ/mol (full arrows). Experimentally, the energy shift is 45 kJ/mol, while the fundamental of the $\nu_3$ vibration has 36 kJ/mol additional energy compared to the ground state [102]. This results in $\eta_{vibr}$ = 1.25, so the $\nu_3$ vibrational mode is more beneficial than adding the energy to the translational motion.

In the MD simulations, $\eta_{vibr}$ is found to be equal to 0.82. This lower value is due to the lower $\Delta E$ in the simulations compared to the experiments. Furthermore, the vibrational frequency calculated in the simulations is also higher, i.e. 3260 $cm^{-1}$ vs 3019 $cm^{-1}$ (cf. Table 6.1). As a consequence, the energy difference between the $\nu_3$ fundamental and the ground state is 39 kJ/mol, which is 3 kJ/mol more than the experimental value.

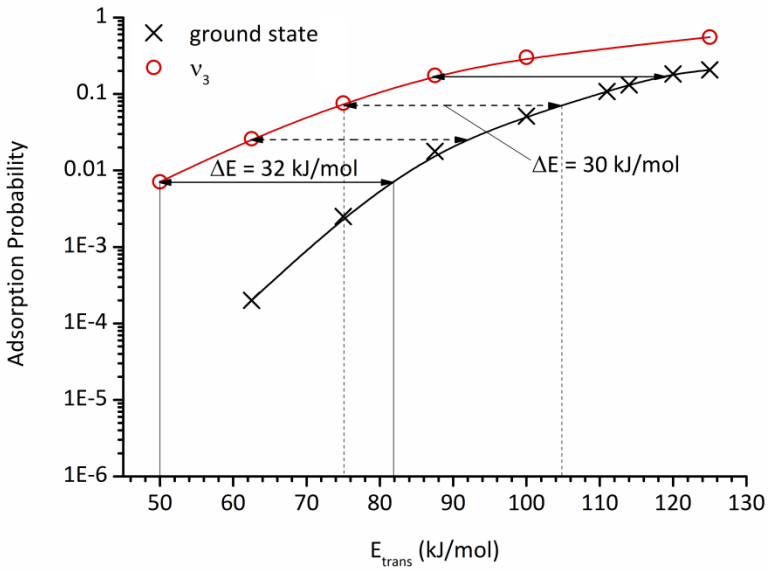


**Figure 7.4:** Adsorption curves of $CH_4$ on Ni(111) obtained with ReaxFF. The full arrows have the same energy shift of 32 kJ/mol, while the dashed arrows have an energy shift of 30 kJ/mol between the ground state and the $\nu_3$ fundamental vibration.

The main issue is that the MD simulations significantly underestimate $\eta_{vibr}$. The value of 0.82 implies that it is more efficient to add the energy to translational motion instead of to the $\nu_3$ fundamental vibration, even though the opposite is found in literature.

As a final test, the adsorption curve of the first overtone of the $\nu_3$ vibration ($2\nu_3$) is calculated in order to determine if $\eta_{vibr}$ of this vibrational state is again underestimated. Similar to our previous comparisons of the adsorption curves between the simulations and experiments (cf. Figures 7.2 and 7.3), the values are higher for the simulations. In this case, however, the difference varies between a factor of 2 to 4, which is smaller than before.

The energy shift between the ground state and the $2\nu_3$ vibration on the other hand, is much lower than the experimental value. Indeed, the experimental value is 65 kJ/mol [103], while in the simulations $\Delta E$ varies between 33.5 kJ/mol and 43 kJ/mol, as shown in Figure 7.5. The $\Delta E$ of 33.5 kJ/mol is obtained in the lower region of $E_{trans}$, where only limited adsorption is observed. At higher $E_{trans}$, the variance of $\Delta E$ is comparable with the one of the fundamental vibration. In the simulations, the energy difference between the first overtone of the $\nu_3$ vibration and the ground state, $\Delta E_{vibra}$, is 78 kJ/mol, so $\eta_{vibr}$ is maximal 0.55. Once more, the simulation underestimates $\eta_{vibr}$, since the experimental value is 0.90.

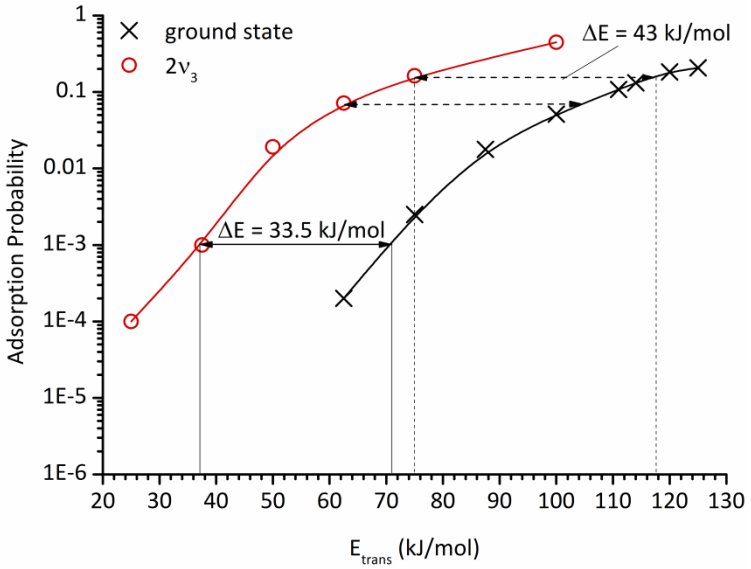


**Figure 7.5:** Adsorption curves of $CH_4$ on Ni(111) obtained with ReaxFF. The full arrow indicates an energy shift of 33.5 kJ/mol, while the dashed arrows have an energy shift of 43 kJ/mol between the ground state and the $2\nu_3$ vibration.

Despite the fact that the shape of the adsorption curves is similar to the experimentally obtained curves, the position of the curves is always higher in the simulations. Obviously, these deviations influence $\eta_{vibr}$. The greatest deviation is observed for the ground state, for which the adsorption probability is a factor of 8 to 25 higher for the simulations. However, no adjustments in the simulation are possible on the ground state. If corrections are made, it should be done on the vibrationally excited states.

### 7.3.3. Corrections to increase the accuracy of the simulations

Before we discuss the possible corrections, it should be emphasized that the corrections are only valid if these are the same for each vibrational state. If for a certain correction, the values of $\eta_{vibr}$ of the $\nu_3$, $2\nu_3$ and $3\nu_4$ vibration are in agreement with the experimental data, this correction is also applicable for the $\nu_1$ and $\nu_2$ vibration. Otherwise, if a separate correction is made for each vibrational mode, each of these modes is actually fitted to the experimental results. This is easily done, but limited to vibrations for which experimental data is available. Obviously, this is inadequate, since the objective of this study is to predict the reactivity of all possible vibrational modes.

a) Correction factor $c_f$

There are two possibilities to adjust the adsorption curves of the vibrationally excited states:

1. Lower the added vibrational energy so that the adsorption curves of the simulations resemble that of the experiments. Consequently, this adsorption curve can be compared with the experimental adsorption curve of the ground state to determine $\Delta E$.
2. Increase the added vibrational energy so that $\Delta E$ calculated from the adsorption curves of the simulations resembles the experimental values.

Subsequently, $\eta_{vibr}$ is calculated with the corrected $\Delta E$ and the uncorrected $E_{vibr}$, i.e., the energy difference between the ground and excited state that

was used before, not taking into account the increased or lowered amount of added energy. Clearly, this approximation requires thorough validation before applying the corrections to the other vibrational modes.

The added vibrational energy is changed by including the correction factor, $c_f$, in the calculation of $E_{vibr}$, as shown in equation 7.2.

$$\mathrm{E_{vibr}} = \mathrm{h\nu}\left(\mathrm{c}_f \cdot \mathrm{n} + \frac{1}{2}\right) \tag{7.2}$$

The correction factor is placed in front of *n* because we noticed that $\Delta\mathrm{E}$ of $2\nu_3$ resembles the value that is expected for $\nu_3$, i.e. 43 kJ/mol while 45 kJ/mol is mentioned in literature. By setting $c_f$ to 2, the adsorption curve of $\nu_3$ is shifted upwards so that $\Delta\mathrm{E}$ nearly fits to the experimental value. This corresponds to the second possibility mentioned above to adjust the adsorption curves.

If $c_f$ is given a value lower than 1, the curve moves down, and the first possibility is followed. However, test simulations indicated that $c_f$ should be smaller than 0.05 to come close to the experimental adsorption curve of $\nu_3$. For this value, the energy is almost equal to that of the ground state, which implies that vibrational motion is hardly included. Therefore, this method does not seem suitable, and the second possibility to adjust the adsorption curves is used in this chapter.

Instead of calculating the adsorption probability at several translational energies to obtain the adsorption curves, we only used specific values of $E_{trans}$ for the following sections, since the focus is on $\Delta\mathrm{E}$. Indeed, it is shown in Figures 7.4 and 7.5 that for high values of $E_{trans}$, $\Delta\mathrm{E}$ is almost constant, so it can be determined from a single data point and does not require the entire adsorption curve to be calculated.

As mentioned above, an energy shift of 43 kJ/mol is observed for the $\nu_3$ vibration if $c_f$ is equal to 2. The energy difference between the $\nu_3$

fundamental and the ground state is 39 kJ/mol, so $\eta_{vibr}$ is equal to 1.10. This is still lower than the experimental value of 1.25, but the correct order (i.e. > 1) is now obtained.

With the same $c_f$, $\Delta E$ between the $2\nu_3$ vibration at a translational energy of 50 kJ/mol and the ground state is equal to 53 kJ/mol. The resulting $\eta_{vibr}$ is 0.68, while the experimental value is 0.90. It is clear that a higher $c_f$ is required for both vibrational states of the $\nu_3$ mode to increase $\eta_{vibr}$ to the experimental value. However, before turning attention towards optimizing the correction factor, it is important to determine if the influence of $c_f$ on the other vibrational modes is the same. If this is not the case, there is no point in optimizing $c_f$.

Therefore, the influence of $c_f$ on the vibrational efficiency of the $3\nu_4$ vibration is determined. Without this correction factor, $\eta_{vibr}$ is equal to 0.26 for this vibrational state, at an $E_{trans}$ of 75 kJ/mol, whereas the experimental value is 0.72 [98]. With the correction, the adsorption probability significantly increases from 0.0274 to 0.3246. Such a value is not obtained in the studied range of $E_{trans}$ of the ground state, so $\Delta E$ is certainly greater than 50 kJ/mol. An additional calculation at $E_{trans}$ = 50 kJ/mol resulted in an accurate $\Delta E$ of 55 kJ/mol. The corresponding $\eta_{vibr}$ is 0.81, which is not only higher than the experimental value, but also higher than $\eta_{vibr}$ of the $2\nu_3$ vibration. This is in contrast with experiments, since the antisymmetric stretch vibration should be more reactive than the antisymmetric bend vibration.

This large deviation is a consequence of the difference in the vibrational frequencies between our simulations and experiments. The calculated vibrational frequencies were already summarized and compared with the experimental data in Table 6.1. It was shown that the vibrational energy of the fundamental was higher for the simulations. At higher vibrational states, the difference between simulations and experiments further increases, as illustrated in Table 7.2. Indeed, the energy difference between the ground

state and the $3\nu_4$ vibration is 23 kJ/mol higher in the simulations. This is a substantial difference, hence the higher reactivity.

**Table 7.2:** Comparison of the energy difference between the ground state and different vibrational states between the simulations and experiments.

| vibr. state | $\Delta E_{vibr}$, simulations (kJ/mol) | $\Delta E_{vibr}$, experimental (kJ/mol) |
|---|---|---|
| $\nu_3$ | 39 | 36 |
| $2\nu_3$ | 78 | 71 |
| $3\nu_4$ | 68 | 45 |

The difference between simulations and experiments is smaller for the $\nu_3$ and $2\nu_3$ vibration, i.e., 3 kJ/mol and 7 kJ/mol, respectively. Therefore, the influence of the vibrational frequency in the simulations on the reactivity is less obvious for these vibrational states. Nevertheless, the results for the $3\nu_4$ vibration demonstrate the deviation with experiments due to the calculated vibrational frequencies. In order to remove this deviation, the experimental values are used in the following section.

b) Corrected vibrational frequencies

The experimental values of the vibrational frequencies are combined with $c_f$ (equal to 2) to calculate the adsorption probability of $CH_4$ excited to the $\nu_3$, $2\nu_3$ and $3\nu_4$ vibrational states. The results are shown in Figure 7.6, in which $\Delta E$ for each vibrational state can be determined. These values of $\Delta E$ are summarized in Table 7.3, together with the corresponding $\eta_{vibr}$.

**Table 7.3:** Calculated values of $\eta_{vibr}$ for the $\nu_3$, $2\nu_3$ and $3\nu_4$ vibrational state. These values are obtained with the correction factor $c_f$ and by using the experimental vibrational frequencies.

| vibr. state | $\Delta E$ (kJ/mol) | $\Delta E_{vibr}$ (kJ/mol) | $\eta_{vibr}$, simulations | $\eta_{vibr}$, experimental |
|---|---|---|---|---|
| $\nu_3$ | 41 | 36 | 1.14 | 1.25 |
| $2\nu_3$ | 53 | 71 | 0.75 | 0.90 |
| $3\nu_4$ | 32 | 45 | 0.71 | 0.72 |

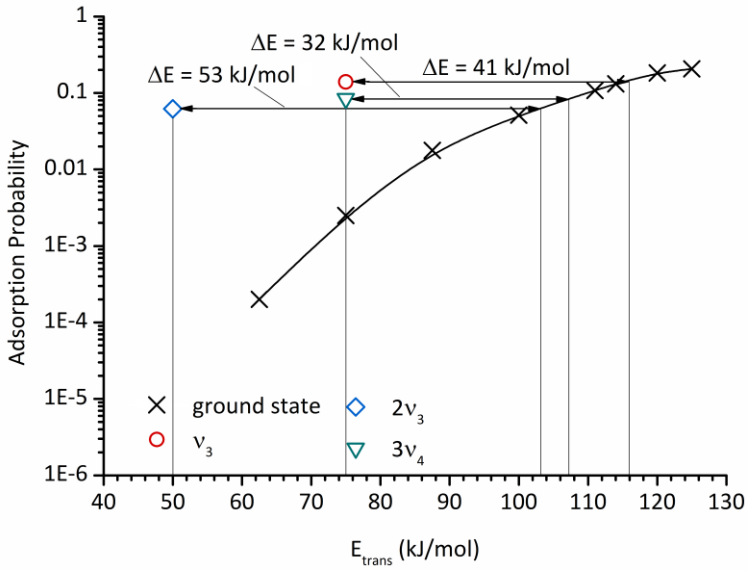


**Figure 7.6:** Adsorption probability of $CH_4$ excited to the $\nu_3$, $2\nu_3$ and $3\nu_4$ vibrational state, compared to the adsorption curve of the ground state.

The results of the simulations are now in better agreement with the experiments. First, the simulations now correctly describe whether excitation to a specific vibrational state is more ($\eta_{vibr} > 1$) or less ($\eta_{vibr} < 1$) efficient than adding energy to the translational motion. Second, excitation to the $3\nu_4$ vibrational state is less efficient than excitation to the $2\nu_3$ vibrational state, as is also observed experimentally. It should be noted that $\eta_{vibr}$ of $\nu_3$ and $2\nu_3$ is still lower than the experimental value. As mentioned before, optimization of $c_f$ is required to further mimic these values.

Before describing the optimization of $c_f$, it is useful to determine if the reactivity of the $\nu_1$ vibration is as expected. No experimental values of $\eta_{vibr}$ for this vibrational state on Ni(111) are available, however on Ni(100), this vibration is the most reactive [100]. This is also found with computational studies on Ni(100) [108]. Furthermore, the same computational setup predicts that the reactivity on Ni(111) is higher for the $\nu_1$than for the $\nu_3$ vibrational state [107].

Remarkably, the high reactivity of the $\nu_1$ vibration is not observed in the MD simulations, despite the use of $c_f$ and the experimental vibrational frequencies (see Figure 7.7).

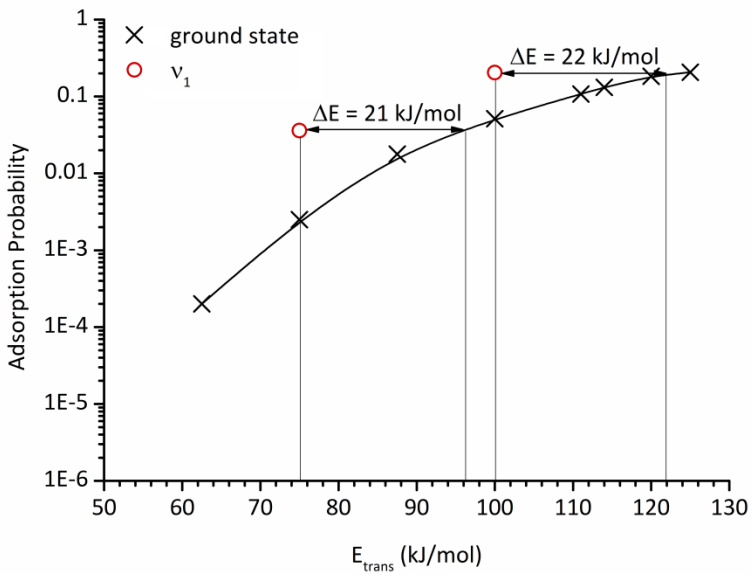


**Figure 7.7:** Adsorption probability of $CH_4$ excited to the $\nu_1$ vibrational state at $E_{trans}$ of 75 kJ/mol and 100 kJ/mol, and the corresponding $\Delta E$ with the adsorption curve of the ground state.

The energy difference between the ground state and the excited state is 35 kJ/mol, but $\Delta E$ is only 22 kJ/mol. Hence, $\eta_{vibr}$ of the $\nu_1$ vibration is 0.63. According to the MD simulations, this vibrational state is less efficient than just adding the energy to the translational motion. Furthermore, it is even less reactive than the $3\nu_4$ vibrational state. Both observations are the opposite of the predictions of previous studies.

This much lower reactivity of the $\nu_1$ state cannot be corrected, since any correction made to this vibrational state, also has to be made for the other vibrational states. Each increase in reactivity of the $\nu_1$ state, will also increase the reactivity of the $3\nu_4$ state. Therefore, the expected reactivity sequence, i.e. $\nu_1 > \nu_3 > 3\nu_4$, will not be obtained.

The same setup is used for some simulations of the single impact of $CH_4$, excited to the $\nu_1$ and $\nu_3$ state, on Ni(100). Again, the $\nu_1$ state is less reactive than the $\nu_3$ state, while the opposite should be observed.

### 7.3.4. Limitations of the MD simulations

The results of our MD simulations do not fully correspond to the experimental observations, especially for the $\nu_1$ state. It is likely, however, that during the experiments, a part of the $CH_4$ molecules is not excited to the correct state so the molecules are actually distributed over several states. Nevertheless, both experimental [100] and computational studies [107,108] conclude that the $\nu_1$ state is the most reactive, while it has the lowest reactivity in the MD simulations.

Another remark is that the vibrational excitation in the simulations corresponds to a harmonic oscillator, while it actually has an anharmonic character. However, even when using the experimental vibrational frequencies, which describe the correct energy levels of the vibrational states, the correction factor $c_f$ is still necessary to obtain good results for the $\nu_3$, $2\nu_3$ and $3\nu_4$ vibrational states. By using the correction factor, the maximum C-H bond length or H-C-H bond angle obtained during the vibration is increased. For a specific vibrational state, the maximum bond length is longer in the anharmonic oscillator compared to the harmonic oscillator. Thus, the use of $c_f$ and the experimental vibrational frequencies can be seen as a method to come closer to the anharmonic character of the vibrational excitation. However, even though the same corrections are made for the $\nu_1$ and $\nu_3$ state, the reactivity of the $\nu_1$ state is largely underestimated.

Clearly, there are some aspects that are not taken into account in the MD simulations. Two of such aspects, that might explain the deviations in these simulations, are found in literature and discussed on the next page.

1. When approaching the nickel surface, the $\nu_1$ state correlates to a localized oscillation of the C-H bond that is orientated to the surface. The opposite is true for the $\nu_3$ state, in which the energy is localized in the $CH_3$ group that is pointing away from the surface. Therefore, the $\nu_1$ state is more reactive, since the energy in the C-H bond that breaks is higher [106].
2. The vibrational efficiency can also be related to the capability of each vibrational state to undergo non-adiabatic coupling, i.e. the transfer of vibrational energy to either the ground state or a vibrational state of lower energy. The excess energy is converted into motion along the reaction path, which corresponds to the C-H bond breaking at the transition state. This non-adiabatic coupling is stronger for the $\nu_1$ state, hence the higher reactivity [107,108].

In our simulations, the vibrational motion is maintained until $CH_4$ approaches the nickel surface. The motion is then influenced, but not to the same extent as described in the literature. For instance, the energy is not localized in the C-H bond that is orientated to the surface (first aspect). Furthermore, the molecule does not return to the ground state (second aspect).

While it is possible to (artificially) fix the vibrational energy to a specific C-H bond, the second aspect cannot be added to our simulations. Moreover, fixing the vibrational energy to a specific C-H-bond would be specific for each vibrational mode, and as discussed earlier, this is insufficient to meet the objective of this study. If each vibrational mode has its own corrections, the MD simulations can mimic the experimental results, but no valid conclusions are possible for vibrational modes that are not discussed in literature.

Therefore, we must conclude that it is not possible to predict the reaction behavior of all vibrational modes with our MD simulations.

## 7.4. Conclusion

The validity of the MD simulations to describe the reaction behavior of vibrationally excited $CH_4$ was investigated in this chapter.

It is shown that without corrections, $\eta_{vibr}$ of the $\nu_3$ and $2\nu_3$ vibrational state on Ni(111) is underestimated in the simulations. The vibrational efficiency can be increased by adding a correction factor, $c_f$. With a given value of 2, this correction factor increases $\eta_{vibr}$ to the correct order, i.e., $\eta_{vibr,\nu_3} > 1$. However, the same correction is insufficient for the $3\nu_4$ state. This vibrational state has a higher simulated $\eta_{vibr}$ than the $2\nu_3$ state, which is in contrast with literature data.

An additional correction is made by replacing the vibrational frequencies calculated in the simulations by the experimental values. Prior to this correction, the energy difference between the ground state and the $3\nu_4$ vibrational state was 23 kJ/mol higher in the simulations. This correction, combined with $c_f$, results in values of $\eta_{vibr}$ for $\nu_3$, $2\nu_3$ and $3\nu_4$ that are in better agreement with literature, even though optimization of $c_f$ is still necessary.

Finally, it is illustrated that the reactivity of the $\nu_1$ vibrational state is not as predicted in literature, despite of the corrections added to the simulation. This is the most reactive vibrational state, but in the simulations it has a reactivity lower than the $3\nu_4$ state. The cause of this low reactivity is related to the fact that in the simulations, the vibrational energy is not localized in the C-H bond that is directed towards the surface, and eventually will undergo bond breaking. Furthermore, the non-adiabatic coupling of the vibrational modes to the ground state or a vibrational state of lower energy is also not included in the simulations.

Because of the limitations mentioned above, we must conclude that it is not possible to predict the reaction behavior of all vibrational modes with our MD simulations.

The findings of this chapter can be summarized as follows:

- Initial $\eta_{vibr}$ of $\nu_3$, $2\nu_3$ and $3\nu_4$:
  - Much lower compared to experimental values
  - $\eta_{vibr}$ of $\nu_3$ < 1, which is not in agreement with experiments
- Correction factor $c_f$:
  - $\eta_{vibr}$ of $\nu_3$ and $2\nu_3$ more in agreement with experiments
  - $\eta_{vibr}$ of $3\nu_4$ too high, due to high vibrational energy
- Corrected vibrational frequencies:
  - $\eta_{vibr}$ of $\nu_3$, $2\nu_3$ and $3\nu_4$ more in agreement with experiments
  - $\eta_{vibr}$ of $\nu_1$ too low
- Limitations of the MD simulations:
  - No vibrational energy localization in C-H bond ($\nu_1$) or $CH_3$ group ($\nu_3$)
  - No non-adiabatic coupling of the vibrational modes to the ground state or a vibrational state of lower energy

# Summary and conclusions

The increased greenhouse gas (GHG) concentrations compared to the pre-industrial values have led to an enhanced greenhouse effect and, as a consequence, global warming. Anthropogenic GHG emissions, for instance by the continuous use of fossil fuels, are responsible for the enhanced greenhouse effect and proper actions are necessary to stabilize and eventually lower the GHG concentrations, in order to mitigate climate change.

One of the recommended actions is increasing the energy efficiency of industrial processes. This is particularly interesting for the methane reforming processes, since $CH_4$ (and $CO_2$ in the case of dry reforming) is converted into syngas, a valuable chemical mixture of $H_2$ and CO. These processes have a large energy cost under conventional conditions, due to the high temperatures that are required.

A promising alternative to the conventional procedure is the use of plasma catalysis, i.e. the combination of plasma technology and catalysis. The reactive plasma can activate the molecules and induce reactions at reduced temperatures, while the catalyst can increase the selectivity. However, this technology is very complex and there is little fundamental knowledge on the operative interaction mechanisms between plasma and catalyst (cf. Chapter 1). It is difficult to study these interactions experimentally, since any interference with the plasma changes its properties. In addition to experimental research, computational studies are necessary to obtain fundamental information about the mechanisms.

In this dissertation, reactive molecular dynamics simulations are used to investigate the interactions of plasma species on different nickel catalyst surfaces. The plasma species under study are $CH_x$ radicals (x={1,2,3}) and vibrationally excited $CH_4$. A total of six different nickel surfaces are

considered, to study the influence of crystallinity on the reactivity. Furthermore, the capability of MD simulations for describing plasma catalysis is assessed.

In a MD simulation, the trajectories of all atoms in the system are followed through space and time by integrating their equations of motion. The forces between the atoms are derived from a suitable interatomic potential. In this dissertation, the ReaxFF potential is used, employing parameters for Ni/C/H. The applied temperature is varied between 400 K – 1600 K and is controlled with the Berendsen and Bussi thermostats. Both single as well as consecutive impacts are performed to study the reactivity. More information about the simulation method can be found in Chapter 2.

In Chapter 3, the interaction of $CH_x$ radicals with nickel surfaces is investigated at a temperature of 400 K, using the Berendsen thermostat to control the temperature. It is shown that the CH radical has the highest adsorption probability on all surfaces, followed by $CH_2$ and $CH_3$. This is explained by the decreasing number of free electrons in the radical and the increasing steric hindrance in the series CH – $CH_2$ – $CH_3$. The reactivity after adsorption follows the same trend, i.e. it is high for CH and $CH_2$, and low for $CH_3$.

Different mechanisms are observed during the $CH_2$ impacts, dependent on the nickel surface. On Ni(100), the adsorbed H-atoms take part in the reaction mechanisms, whereas the H-atoms adsorbed on the Ni(111) structures do not. Furthermore, the presence of steps in the Ni(111) structure leads to additional C-H bond breaking after $CH_3$ impacts and a slight increase in $C_2H_4$, $C_2H_6$ and $H_2$ formation after $CH_2$ impacts compared to the flat Ni(111).

Little $H_2$ is formed during the simulations at a temperature of 400 K. Therefore, the emphasis in Chapter 4 is on $H_2$ formation in a temperature range of 400 K – 1600 K on Ni(111). The Bussi thermostat is used for these simulations, after being successfully validated with the previous results. Below 1400 K, low $H_2$ yields are obtained in the nanosecond time scale of our

simulations. Above this temperature, $H_2$ formation becomes the dominant process. Again, the reactivity of $CH_3$ is lower than that of $CH_2$ and CH. It is also illustrated that the high temperatures promote C-diffusion into the subsurface of Ni(111). This is of importance since the adsorbed C-atoms can normally form CO if oxidative species are present. By diffusing into the nickel surface, the oxidation of C-atoms is impeded and the catalyst is deactivated.

In Chapter 5, the study on the temperature influence performed in Chapter 4 is extended towards the other nickel surfaces, including an amorphous structure. It is found that after adsorption of a single $CH_x$ radical, the subsequent C-H bond breaking is dependent on both temperature and surface structure. A higher temperature increases the C-H bond breaking. Likewise, step-edges in the structure or surfaces with high surface energy promote C-H bond breaking. However, the surfaces that promote the C-H bond breaking are not necessarily the most selective towards $H_2$ formation during consecutive impacts at high temperatures. It is found that the surface structure initially does influence the C-H bond breaking and $H_2$ formation, but the crystallinity is reduced due to the continuous C-diffusion into the surface. A proper distinction between the different surfaces cannot be made anymore, and the initial C-H bond breaking probability will also change. It is therefore concluded that as the C-diffusion in the surface increases, the role of the surface structure seems to become limited.

Furthermore, it is illustrated that within the temperature range of 400 K – 800 K, the adsorbed H-atoms already react with other incoming radicals, while the C-diffusion into the surface remains low. Even though little $H_2$ is directly formed at these temperatures in our simulations, the fairly high reactivity between incoming radicals and adsorbed species is interesting for plasma catalysis applications.

The scope of the research is changed towards the reactivity of vibrationally excited $CH_4$ in Chapters 6 and 7. First, a method is developed to include vibrational motion in the MD simulations (Chapter 6). Our approach consists

of first calculating the normal coordinates of the vibrational modes. Afterwards, these are linked to the vibrational velocities, keeping into account the mode specific vibrational energy. Finally, a correction to the velocities of the C-atom is made to keep the center of mass velocity of the antisymmetric stretch and bend vibration equal to zero. Rotational motion of the antisymmetric stretch vibration is also corrected. The obtained vibrational motions of $CH_4$ remain constant for at least 6.25 ps, which is sufficient to perform impacts.

These impacts are performed on Ni(111) in Chapter 7, to validate if the reaction behavior of the vibrational modes is simulated correctly. It is shown that the vibrational efficiency ($\eta_{vibr}$) of the $\nu_3$ and $2\nu_3$ vibrational state is underestimated in the simulations. With the use of a correction factor, $c_f$, the vibrational efficiency of both modes is increased to the correct order, i.e., $\eta_{vibr} > 1$. However, the same correction is insufficient to correctly describe the $3\nu_4$ state. This issue is solved by replacing the vibrational frequencies calculated in the simulations by the experimental values.

Despite these corrections, the reactivity of the $\nu_1$ vibrational state is not as predicted in literature. It appears that in the simulations, the vibrational energy is not localized in the C-H bond that is directed towards the surface, and eventually will undergo bond breaking. Furthermore, there is also no non-adiabatic coupling of the vibrational mode to the ground state or lower vibrational states. Therefore, we conclude that it is not possible to predict the reaction behavior of all vibrational modes with our MD simulations.

As a final conclusion to this dissertation, some aspects regarding the possibilities, limitations and future prospects of MD simulations for plasma catalysis are summarized on the following page.

- General remarks on MD simulations:
    - The nanoscale system size allows studies on the change in crystallinity or on the influence of defects. However, changes in morphology require a larger system size and cannot be addressed.
    - MD simulations are also limited with respect to the time scale they can handle. Specifically, if certain reactions are not observed during the MD simulations, it does not necessarily mean that these reactions will not take place at all. The time scale of the MD simulations is possibly too short for these reactions to occur.
    - The realism of MD simulations in describing plasma catalysis is determined by the accuracy of the interatomic potential. Without a proper potential, no accurate information is obtained.
- Plasma species and MD simulations:
    - The reaction behavior of molecules and radicals is correctly described within the simulations. Even ions can be included, as this is done before [159–161].
    - The reactivity of vibrationally excited species is not described correctly, thus these species cannot be included in MD studies on plasma catalysis
- Future prospects:
    - The presence of oxidative species will provide more information regarding the dry reforming mechanisms. Furthermore, other experimentally used catalyst surfaces can be investigated. Clearly, this is dependent on the availability of an accurate interatomic potential.
    - The reactivity on nanoclusters can be investigated. The high degree of curvature in the structure is likely to have an effect on the bond breaking probability.

# Samenvatting en conclusies

De toegenomen concentratie van broeikasgassen in vergelijking met pre-industriële waarden heeft geleid tot het versterkt broeikaseffect, en als gevolg hiervan, opwarming van de aarde. De voornaamste oorzaak van de toegenomen concentratie zijn antropogene broeikasgasemissies, bvb. door het aanhoudende gebruik van fossiele brandstoffen. Er zijn verscheidene acties nodig die de concentraties van de broeikasgassen stabiliseren en uiteindelijk verminderen, om zo de klimaatverandering tegen te gaan.

Een mogelijke actie is het verhogen van de energie-efficiënte van industriële processen. Dit is bijzonder interessant voor methaan reforming processen, aangezien $CH_4$ (en $CO_2$ voor de 'dry reforming') omgezet wordt in syngas, een mengsel van $H_2$ en CO. Dergelijke processen hebben echter een hoge energiekost, door de vereiste hoge temperaturen.

Een veelbelovend alternatief voor de conventionele procedures is het gebruik van plasmakatalyse. Dit is een combinatie van plasmatechnologie en katalyse. Het reactieve plasma kan de moleculen activeren, en reacties teweegbrengen bij lagere temperaturen, terwijl de katalysator de selectiviteit kan verhogen. Deze technologie is echter zeer complex, en er is weinig fundamenteel inzicht in de interactiemechanismes tussen het plasma en de katalysator (cf. Hoofdstuk 1). Dergelijke interacties zijn experimenteel moeilijk te bestuderen, aangezien elke verstoring van het plasma de eigenschappen ervan zal veranderen. Hierdoor is er nood aan computationele studies, die fundamentele informatie over de interactiemechanismes kunnen verkrijgen.

In dit proefschrift zijn reactieve moleculaire dynamica (MD) simulaties gebruikt om de interacties van plasmadeeltjes op verschillende nikkel katalysatoroppervlakken te onderzoeken. De bestudeerde plasmadeeltjes zijn $CH_x$ radicalen (x={1,2,3}) en vibrationeel geëxciteerd $CH_4$. In totaal zijn 6

verschillende nikkeloppervlakken in het onderzoek gebruikt om de invloed van de kristalliniteit op de reactiviteit te bestuderen. Voorts wordt er nagegaan in welke mate MD simulaties geschikt zijn om plasmakatalyse te beschrijven.

In een MD simulatie wordt de beweging van alle atomen gevolgd door ruimte en tijd, door integratie van de bewegingsvergelijkingen. De krachten die op de atomen inwerken zijn afgeleid van een interatomaire potentiaal. In dit proefschrift wordt de ReaxFF potentiaal gebruikt, met parameters voor het Ni/C/H systeem. De opgelegde temperatuur varieert tussen 400 K en 1600 K, en wordt gecontroleerd met de Berendsen en Bussi thermostaten. Zowel enkelvoudige als consecutieve impacts zijn uitgevoerd om de reactiviteit te bestuderen. Meer informatie over de methodiek van de simulaties is gegeven in Hoofdstuk 2.

In Hoofdstuk 3 zijn de interacties van de $CH_x$ radicalen op de nikkel katalysatoroppervlakken onderzocht bij een temperatuur van 400 K, gebruikmakend van de Berendsen thermostaat om de temperatuur te controleren. Er wordt aangetoond dat het CH radicaal de grootste kans op adsorptie heeft op alle oppervlakken, gevolgd door $CH_2$ en $CH_3$. Dit wordt verklaard door het dalende aantal vrije elektronen van het radicaal en de toenemende sterische hindering in de serie CH – $CH_2$ – $CH_3$. De reactiviteit na adsorptie volgt dezelfde trends, nl. deze is hoog voor CH en $CH_2$, en laag voor $CH_3$.

Afhankelijk van het nikkel oppervlak zijn er verschillende mechanismes waargenomen tijdens de $CH_2$ impacts. Op Ni(100) nemen de geadsorbeerde H-atomen deel aan de reacties, terwijl de H-atomen geadsorbeerd op de Ni(111) structuren dit niet doen. Verder leidt de getrapte Ni(111) structuur tot een toegenomen C-H bindingsbreking na impacts van $CH_3$, en een lichte stijging in de vorming van $C_2H_4$, $C_2H_6$ en $H_2$ na $CH_2$ impacts in vergelijking met het vlakke Ni(111).

Er is weinig $H_2$ vorming tijdens de simulaties bij een temperatuur van 400 K. Daarom wordt in Hoofdstuk 4 de $H_2$ vorming op Ni(111) onderzocht in een temperatuurbereik van 400 K – 1600 K. De Bussi thermostaat wordt gebruikt voor deze simulaties, nadat deze met succes gevalideerd is met de vorige resultaten. Bij temperaturen lager dan 1400 K, en binnen de nanoseconde tijdschaal van onze simulaties, zijn de $H_2$ rendementen laag. Bij hogere temperaturen wordt de $H_2$ vorming het dominante proces. De reactiviteit van $CH_3$ is weer lager dan die van $CH_2$ en CH. Het blijkt ook dat de hoge temperaturen de diffusie van C-atomen in het nikkeloppervlak bevorderen. Dit is van belang aangezien de geadsorbeerde C-atomen CO kunnen vormen, als er oxidatieve deeltjes aanwezig zijn. Door diffusie in het nikkeloppervlak wordt dergelijke oxidatie van C-atomen verhinderd en de katalysator wordt gedeactiveerd.

In Hoofdstuk 5 wordt de studie naar de invloed van de temperatuur uit Hoofdstuk 4 uitgebreid naar de andere nikkel oppervlakken, waaronder een amorfe structuur. Het blijkt dat na adsorptie van een enkel $CH_x$ radicaal, de daaropvolgende C-H bindingsbreking afhankelijk is van zowel de temperatuur als van de oppervlaktestructuur. Een hogere temperatuur verhoogt de C-H bindingsbreking. De aanwezigheid van trappen in de oppervlaktestructuur, of oppervlakken met een hoge oppervlakte-energie verhogen de C-H bindingsbreking ook. De oppervlakken die de C-H bindingsbreking bevorderen zijn echter niet de meest selectieve voor $H_2$ vorming tijdens de consecutieve impacts bij hoge temperaturen. Aanvankelijk beïnvloedt de oppervlaktestructuur de C-H bindingsbreking en $H_2$ vorming, maar de kristalliniteit van het oppervlak wordt verminderd door de constante C-diffusie in het oppervlak. Daardoor is het niet meer mogelijk om een goed onderscheid te maken tussen de verschillende oppervlakken. Mogelijk zal de geschatte C-H bindingbreking, die bepaald is na enkelvoudige impacts op zuivere nikkel oppervlakken, ook veranderen door de gereduceerde kristalliniteit van het oppervlak. De conclusie is dat naarmate de C-diffusie in het oppervlak stijgt, de rol van de oppervlaktestructuur beperkt lijkt te worden.

Er is ook aangetoond dat de geadsorbeerde H-atomen al reageren met andere inkomende radicalen in het temperatuurbereik van 400 K – 800 K, terwijl de C-diffusie in het oppervlak laag blijft. Hoewel er weinig directe $H_2$ vorming is bij deze temperaturen in onze simulaties, is de vrij hoge reactiviteit tussen inkomende radicalen en geadsorbeerde deeltjes interessant voor plasmakatalytische toepassingen.

Het onderzoek wordt uitgebreid naar de reactiviteit van vibrationeel geëxciteerd $CH_4$ in Hoofdstukken 6 en 7. Eerst wordt er een methode ontwikkeld om de vibrationele bewegingen toe te voegen aan de MD simulaties (Hoofdstuk 6). In onze werkwijze worden eerst de normaalcoördinaten van de vibrationele modes berekend. Daarna worden deze gekoppeld aan de vibrationele snelheden, rekening houdend met de mode-specifieke vibrationele energie. Ten slotte worden de snelheden van het C-atoom gecorrigeerd zodat de antisymmetrische rek- en buigvibratie geen initiële translationele beweging maken. De rotationele beweging van de antisymmetrische rekvibratie wordt ook gecorrigeerd. De bekomen vibrationele bewegingen blijven constant gedurende ten minste 6.25 ps, wat voldoende is om de impacts uit te voeren.

Deze impacts worden uitgevoerd op het Ni(111) oppervlak in Hoofdstuk 7, om te valideren of de reactiviteit van de vibrationele modes juist gesimuleerd wordt. De vibrationele efficiëntie van de $\nu_3$ en $2\nu_3$ vibrationele toestand ($\eta_{vibr}$) wordt echter onderschat in de simulaties. Gebruikmakend van een correctiefactor, $c_f$, wordt de vibrationele efficiëntie van beide modi verhoogd tot de juiste grootteorde, nl. $\eta_{vibr} > 1$. Dezelfde correctie is echter onvoldoende om de $3\nu_4$ vibrationele toestand juist te beschrijven. Dit probleem wordt opgelost door de vibrationele frequenties die in de simulaties berekend zijn, te vervangen door de experimentele waardes.

De reactiviteit van de $\nu_1$ vibrationele toestand is ondanks deze verbeteringen niet zoals voorspeld in de literatuur. Het blijkt dat de vibrationele energie in de simulaties niet gelokaliseerd is in de C-H binding die gericht is naar het

oppervlak en uiteindelijk gebroken zal worden. Verder is er geen niet-adiabatische koppeling van de vibrationele mode naar de grondtoestand of een lagere vibrationele toestand. Hieruit concluderen we dat het niet mogelijk is de reactiviteit van alle vibrationele modes te voorspellen met onze MD simulaties.

Als eindconclusie van dit proefschrift zijn een aantal aspecten met betrekking tot de mogelijkheden, beperkingen en toekomstperspectieven van MD simulaties op plasmakatalyse hieronder samengevat.

- Algemene opmerkingen over MD simulaties:
    - De simulaties op nanoschaal geven de mogelijkheid om de invloed van kristalliniteit of aanwezigheid van defecten in het oppervlak te bestuderen. Veranderingen in de morfologie kunnen echter niet beschreven worden, aangezien hier een groter systeem voor nodig is.
    - MD simulaties zijn ook beperkt in de tijdschaal die ze aankunnen. Reacties die niet voorkomen tijdens de simulaties, kunnen echter in realiteit wel plaatsvinden. Mogelijk treden deze reacties in werkelijkheid dus op over een langere tijdschaal.
    - De nauwkeurigheid van de interatomaire potentiaal is essentieel om plasmakatalyse realistisch te beschrijven met MD simulaties. Zonder een goede potentiaal, zal er geen accurate informatie verkregen worden.
- Plasmadeeltjes en MD simulaties:
    - De reactiviteit van moleculen en radicalen wordt correct beschreven in de simulaties. Zelfs ionen kunnen inbegrepen worden in de simulaties, aangezien dit eerder al is gedaan [159–161].
    - De reactiviteit van vibrationeel geëxciteerde moleculen wordt niet correct beschreven in de simulaties. Dit type van

plasmadeeltjes kan dus niet gebruikt worden in de MD studie op plasmakatalyse.

- Toekomstig onderzoek:
    - De aanwezigheid van oxidatieve deeltjes in de simulaties zal meer informatie geven over de mechanismes in de 'dry reforming' reacties. Voorts kunnen andere experimenteel gebruikte katalysatoren onderzocht worden. Dit is duidelijk afhankelijk van de beschikbaarheid van een geschikte, nauwkeurige interatomaire potentiaal.
    - De reactiviteit op nanoclusters kan worden onderzocht. Deze sterk gekromde structuren zullen waarschijnlijk de kans op bindingsbreking vergroten.

# List of publications

Publications related to this PhD dissertation

1. **W. Somers**, A. Bogaerts, A.C.T. van Duin and E.C. Neyts, "Plasma Species Interacting with Nickel Surfaces: Towards an Atomic Scale Understanding of Plasma-Catalysis", *J. Phys. Chem. C* 116 (2012) 20958-20965
2. A. Bogaerts, R. Aerts, R. Snoeckx, **W. Somers**, W. Van Gaens, M. Yusupov, E. Neyts, "Modeling of plasma-surface interactions for medical, environmental and nano applications", *J. Physics: Conf. Series* 399 (2012) 012011
3. **W. Somers**, A. Bogaerts, A.C.T. van Duin, S. Huygh, K.M. Bal and E.C. Neyts, "Temperature influence on the reactivity of plasma species on a nickel catalyst surface: an atomic scale study", *Catal. Today* 211 (2013) 131-136
4. **W. Somers**, A. Bogaerts, A.C.T. van Duin and E.C. Neyts, "Interactions of plasma species on nickel catalysts: a reactive molecular dynamics study on the influence of temperature and surface structure", *Appl. Catal. B: Environ.* 154-155 (2014) 1-8

Publications not related to this PhD dissertation

1. **W. Somers**, M.F. Dubreuil, E.C. Neyts, D. Vangeneugden, A. Bogaerts, "Incorporation of Fluorescent Fyes in Atmospheric Pressure Plasma Coatings for In-Line Monitoring of Coating Homogeneity", *Plasma Process. Polym.* 11 (2014) 678-684
2. R. Aerts, **W. Somers**, A. Bogaerts, "Carbon Dioxide Splitting in a Dielectric Barrier Discharge Plasma: A Combined Experimental and Computational study", *ChemSusChem* 8 (2015) 702-716

# List of conference contributions

1. **W. Somers**, E.C. Neyts, A. Bogaerts, “Molecular dynamics simulations of the impact of plasma species on nickel catalyst surfaces for plasma catalysis applications”, **poster presentation** at the 12th High Temperature Plasma Processes Conference (HTPP-12), Bologna, Italy, June 24 – 29, 2012
2. **W. Somers**, A. Bogaerts, E.C. Neyts, “Plasma species interacting with nickel surfaces: towards an atomic scale understanding of plasma-catalysis”, **oral presentation** at the International Symposium on Plasmas for Catalysis and Energy Materials (ISPCEM-2012), Tianjin, China, September 21 – 24, 2012
3. **W. Somers**, A. Bogaerts, E.C. Neyts, “Interactions of plasma species on nickel catalyst surfaces as function of temperature: a reactive molecular dynamics study”, **oral presentation** at the 21st International Symposium on Plasma Chemistry (ISPC-21), Cairns, Australia, August 4 – 9, 2013
4. **W. Somers**, A. Bogaerts, E.C. Neyts, “Interactions of plasma species on nickel catalysts: a reactive molecular dynamics study on the influence of temperature and surface structure”, **poster presentation** at the IAP Workshop on ‘Fundamentals of plasma-surface interactions’, Antwerp, Belgium, November 8, 2013
5. **W. Somers**, A. Bogaerts, E.C. Neyts, “Interactions of plasma species on nickel catalysts: a reactive molecular dynamics study on the influence of temperature and surface structure”, **poster presentation** at the Solvay Workshop on ‘Plasmas for environmental applications’, Brussels, Belgium, March 31 – April 2, 2014

# References


[1] J. Bowman, Land Use Policy **7**, 101 (1990).

[2] V. Ramanathan and Y. Feng, Atmos. Environ. **43**, 37 (2009).

[3] D. G. Kessel, J. Pet. Sci. Eng. **26**, 157 (2000).

[4] M. F. Akorede, H. Hizam, M. Z. A. Ab Kadir, I. Aris, and S. D. Buba, Renew. Sustain. Energy Rev. **16**, 2747 (2012).

[5] J. Houghton, Reports Prog. Phys. **68**, 1343 (2005).

[6] O. R. Pichs-Madruga, Y. Sokona, E. Farahani, S. Kadner, K. Seyboth, A. Adler, I. Baum, S. Brunner, P. Eickemeier, B. Kriemann, J. Savolainen, S. Schlömer, C. von Stechow, T. Zwickel, and J. C. Minx, *IPCC, 2014: Climate Change 2014: Mitigation of Climate Change. Contribution of Working Group III to the Fifth Assesment Report of the Intergovernmental Panel on Climate Change* (Cambrigde University Press, Cambrige (UK) and New York (US), 2014).

[7] R. S. Dhillon and G. von Wuehlisch, Biomass and Bioenergy **48**, 75 (2013).

[8] I. Fechete, Y. Wang, and J. C. Védrine, Catal. Today **189**, 2 (2012).

[9] B. Metz, O. Davidson, H. C. de Coninck, M. Loos, and L. A. Meyer, *IPCC, 2005: IPCC Special Report on Carbon Dioxide Capture and Storage. Prepared by Working Group III of the Interngovernmental Panel on Climate Change* (Cambrigde University Press, Cambrige (UK) and New York (US), 2005).

[10] K. Aasberg-Petersen, I. Dybkjær, C. V. Ovesen, N. C. Schjødt, J. Sehested, and S. G. Thomsen, J. Nat. Gas Sci. Eng. **3**, 423 (2011).

[11] F. Banisharifdehkordi and M. Baghalha, Fuel Process. Technol. **120**, 96 (2014).

[12] J. H. Lunsford, Catal. Today **63**, 165 (2000).

[13] J. D. Holladay, J. Hu, D. L. King, and Y. Wang, Catal. Today **139**, 244 (2009).

[14] J. R. Rostrup-Nielsen, Catal. Today **63**, 159 (2000).

[15] I. Lindsay, C. Lowe, S. Reddy, M. Bhakta, and S. Balkenende, Energy Procedia **1**, 4095 (2009).

[16] J. R. H. Ross, Catal. Today **100**, 151 (2005).

[17] K. O. Christensen, D. Chen, R. Lødeng, and A. Holmen, Appl. Catal. A Gen. **314**, 9 (2006).

[18] E. Ahmadi Moghaddam, S. Ahlgren, C. Hulteberg, and Å. Nordberg, Fuel Process. Technol. **132**, 74 (2015).

[19] A. Aziznia, H. R. Bozorgzadeh, N. Seyed-Matin, M. Baghalha, and A. Mohamadalizadeh, J. Nat. Gas Chem. **21**, 466 (2012).

[20] Y. Matsumura and T. Nakamori, Appl. Catal. A Gen. **258**, 107 (2004).

[21] J. Xu and G. F. Froment, Am. Inst. Chem. Eng. J. **35**, 88 (1989).

[22] H. L. Chen, H. M. Lee, S. H. Chen, Y. Chao, and M. B. Chang, Appl. Catal. B Environ. **85**, 1 (2008).

[23] M. C. J. Bradford and M. A. Vannice, Appl. Catal. A Gen. **142**, 73 (1996).

[24] M. C. J. Bradford and M. A. Vannice, Appl. Catal. A Gen. **142**, 97 (1996).

[25] M. Zeppieri, P. L. Villa, N. Verdone, M. Scarsella, and P. De Filippis, Appl. Catal. A Gen. **387**, 147 (2010).

[26] G. Jones, J. G. Jakobsen, S. S. Shim, J. Kleis, M. P. Andersson, J. Rossmeisl, F. Abild-Pedersen, T. Bligaard, S. Helveg, B. Hinnemann, J. R. Rostrup-Nielsen, I. Chorkendorff, J. Sehested, and J. K. Nørskov, J. Catal. **259**, 147 (2008).

[27] M. E. Dry, Catal. Today **71**, 227 (2002).

[28] J. R. H. Ross, A. N. J. van Keulen, M. E. S. Hegarty, and K. Seshan, Catal. Today **30**, 193 (1996).

[29] J. Sehested, Catal. Today **111**, 103 (2006).

[30] E. C. Neyts and A. Bogaerts, J. Phys. D. Appl. Phys. **47**, 224010 (2014).

[31] S. Samukawa, M. Hori, S. Rauf, K. Tachibana, P. Bruggeman, G. Kroesen, J. C. Whitehead, A. B. Murphy, A. F. Gutsol, S. Starikovskaia, U. Kortshagen, J.-P. Boeuf, T. J. Sommerer, M. J. Kushner, U. Czarnetzki, and N. Mason, J. Phys. D. Appl. Phys. **45**, 253001 (2012).

[32] C. Tendero, C. Tixier, P. Tristant, J. Desmaison, and P. Leprince, Spectrochim. Acta - Part B At. Spectrosc. **61**, 2 (2006).

[33] F. M. Aghamir, N. S. Matin, A. H. Jalili, M. H. Esfarayeni, M. A. Khodagholi, and R. Ahmadi, Plasma Sources Sci. Technol. **13**, 707 (2004).

[34] A. Indarto, N. Coowanitwong, J.-W. Choi, H. Lee, and H. K. Song, Fuel Process. Technol. **89**, 214 (2008).

[35] S. Paulussen, B. Verheyde, X. Tu, C. De Bie, T. Martens, D. Petrovic, A. Bogaerts, and B. Sels, Plasma Sources Sci. Technol. **19**, 034015 (2010).

[36] C. De Bie, T. Martens, J. van Dijk, S. Paulussen, B. Verheyde, S. Corthals, and A. Bogaerts, Plasma Sources Sci. Technol. **20**, 024008 (2011).

[37] T. Nozaki and K. Okazaki, J. Japan Pet. Inst. **54**, 146 (2011).

[38] N. R. Pinhão, A. Janeco, and J. B. Branco, Plasma Chem. Plasma Process. **31**, 427 (2011).

[39] K. J. Pringle, J. C. Whitehead, J. J. Wilman, and J. Wu, Plasma Chem. Plasma Process. **24**, 421 (2004).

[40] G. Scarduelli, G. Guella, D. Ascenzi, and P. Tosi, Plasma Process. Polym. **8**, 25 (2011).

[41] A. Fridman, *Plasma Chemistry* (Cambrigde University Press, 2008).

[42] A. Fridman, S. Nester, L. A. Kennedy, A. Saveliev, and O. Mutaf-Yardimci, Prog. Energy Combust. Sci. **25**, 211 (1999).

[43] H.-H. Kim, Y.-H. Lee, A. Ogata, and S. Futamura, Catal. Commun. **4**, 347 (2003).

[44] J. C. Whitehead, Pure Appl. Chem. **82**, 1329 (2010).

[45] H. Huang, D. Ye, D. Y. C. Leung, F. Feng, and X. Guan, J. Mol. Catal. A Chem. **336**, 87 (2011).

[46] J. Van Durme, J. Dewulf, C. Leys, and H. Van Langenhove, Appl. Catal. B Environ. **78**, 324 (2008).

[47] J. Van Durme, J. Dewulf, W. Sysmans, C. Leys, and H. Van Langenhove, Appl. Catal. B Environ. **74**, 161 (2007).

[48] H. T. Quoc An, T. Pham Huu, T. Le Van, J. M. Cormier, and A. Khacef, Catal. Today **176**, 474 (2011).

[49] A. J. Zhang, A. M. Zhu, J. Guo, Y. Xu, and C. Shi, Chem. Eng. J. **156**, 601 (2010).

[50] X. Tu and J. C. Whitehead, Appl. Catal. B Environ. **125**, 439 (2012).

[51] T. Nozaki, N. Muto, S. Kado, and K. Okazaki, Catal. Today **89**, 57 (2004).

[52] T. Nozaki, N. Muto, S. Kadio, and K. Okazaki, Catal. Today **89**, 67 (2004).

[53] J. Sentek, K. Krawczyk, M. Młotek, M. Kalczewska, T. Kroker, T. Kolb, A. Schenk, K. H. Gericke, and K. Schmidt-Szałowski, Appl. Catal. B Environ. **94**, 19 (2010).

[54] X. Tu, H. J. Gallon, M. V Twigg, P. A. Gorry, and J. C. Whitehead, J. Phys. D. Appl. Phys. **44**, 274007 (2011).

[55] H. K. Song, J.-W. Choi, S. H. Yue, H. Lee, and B.-K. Na, Catal. Today **89**, 27 (2004).

[56] H. J. Gallon, X. Tu, and J. C. Whitehead, Plasma Process. Polym. **9**, 90 (2012).

[57] S. S. Kim, H. Lee, J. W. Choi, B. K. Na, and H. K. Song, Catal. Commun. **8**, 1438 (2007).

[58] M. Kraus, B. Eliasson, and A. Wokaun, (2001).

[59] X. Tao, M. Bai, X. Li, H. Long, S. Shang, Y. Yin, and X. Dai, Prog. Energy Combust. Sci. **37**, 113 (2011).

[60] K. Schmidt-Szałowski, K. Krawczyk, J. Sentek, B. Ulejczyk, A. Górska, and M. Młotek, Chem. Eng. Res. Des. **89**, 2643 (2011).

[61] T. Jiang, Y. Li, C. J. Liu, G. H. Xu, B. Eliasson, and B. Xue, Catal. Today **72**, 229 (2002).

[62] Y.-F. Wang, C.-H. Tsai, W.-Y. Chang, and Y.-M. Kuo, Int. J. Hydrogen Energy **35**, 135 (2010).

[63] S. Shang, G. Liu, X. Chai, X. Tao, X. Li, M. Bai, W. Chu, X. Dai, Y. Zhao, and Y. Yin, Catal. Today **148**, 268 (2009).

[64] H. J. Gallon, X. Tu, M. V. Twigg, and J. C. Whitehead, Appl. Catal. B Environ. **106**, 616 (2011).

[65] X. Tu, H. J. Gallon, and J. C. Whitehead, Catal. Today **211**, 120 (2013).

[66] H.-H. Kim, Plasma Process. Polym. **1**, 91 (2004).

[67] H. L. Chen, H. M. Lee, S. H. Chen, M. B. Chang, S. J. Yu, and S. N. Li, Environ. Sci. Technol. **43**, 2216 (2009).

[68] Y. N. Chun, Y. C. Yang, and K. Yoshikawa, Catal. Today **148**, 283 (2009).

[69] N. Rueangjitt, T. Sreethawong, S. Chavadej, and H. Sekiguchi, Chem. Eng. J. **155**, 874 (2009).

[70] C.-J. Liu, J. Zou, K. Yu, D. Cheng, Y. Han, J. Zhan, C. Ratanatawanate, and B. W.-L. Jang, Pure Appl. Chem. **78**, 1227 (2006).

[71] J. Hong, W. Chu, P. A. Chernavskii, and A. Y. Khodakov, J. Catal. **273**, 9 (2010).

[72] H.-H. Kim and A. Ogata, Eur. Phys. J. Appl. Phys. **55**, 13806 (2011).

[73] J. Sehested, J. A. P. Gelten, and S. Helveg, Appl. Catal. A Gen. **309**, 237 (2006).

[74] F. Holzer, U. Roland, and F.-D. Kopinke, Appl. Catal. B Environ. **38**, 163 (2002).

[75] U. Roland, F. Holzer, and F.-D. Kopinke, Appl. Catal. B Environ. **58**, 217 (2005).

[76] F. Holzer, F. D. Kopinke, and U. Roland, Plasma Chem. Plasma Process. **25**, 595 (2005).

[77] K. Hensel, V. Martišovitš, Z. Machala, M. Janda, M. Leštinský, P. Tardiveau, and A. Mizuno, Plasma Process. Polym. **4**, 682 (2007).

[78] K. Hensel, Eur. Phys. J. D **54**, 141 (2009).

[79] R. Li, Q. Tang, S. Yin, and T. Sato, Fuel Process. Technol. **87**, 617 (2006).

[80] X. Tu, H. J. Gallon, and J. C. Whitehead, J. Phys. D. Appl. Phys. **44**, 482003 (2011).

[81] T. Kozák and A. Bogaerts, Plasma Sources Sci. Technol. **24**, 015024 (2015).

[82] R. Snoeckx, R. Aerts, X. Tu, and A. Bogaerts, J. Phys. Chem. C **117**, 4957 (2013).

[83] R. Snoeckx, Y. X. Zeng, X. Tu, and A. Bogaerts, RSC Adv. **5**, 29799 (2015).

[84] C. De Bie, B. Verheyde, T. Martens, J. Van Dijk, S. Paulussen, and A. Bogaerts, Plasma Process. Polym. **8**, 1033 (2011).

[85] R. Aerts, T. Martens, and A. Bogaerts, J. Phys. Chem. C **116**, 23257 (2012).

[86] R. Aerts, W. Somers, and A. Bogaerts, ChemSusChem **8**, 702 (2015).

[87] M. B. Lee, Q. Y. Yang, S. L. Tang, and S. T. Ceyer, J. Chem. Phys. **85**, 1693 (1986).

[88] Q. Y. Yang, K. J. Maynard, A. D. Johnson, and S. T. Ceyer, J. Chem. Phys. **102**, 7734 (1995).

[89] M. P. Kaminsky, N. Winograd, G. L. Geoffroy, and M. A. Vannice, J. Am. Chem. Soc. **108**, 1315 (1986).

[90] B. Xing, X.-Y. Pang, G.-C. Wang, and Z.-F. Shang, J. Mol. Catal. A Chem. **315**, 187 (2010).

[91] J. Li, E. Croiset, and L. Ricardez-Sandoval, J. Mol. Catal. A Chem. **365**, 103 (2012).

[92] J. E. Mueller, A. C. T. van Duin, and W. A. Goddard, J. Phys. Chem. C **113**, 20290 (2009).

[93] J. E. Mueller, A. C. T. van Duin, and W. A. Goddard, J. Phys. Chem. C **114**, 4939 (2010).

[94] J. E. Mueller, A. C. T. van Duin, and W. A. Goddard, J. Phys. Chem. C **114**, 5675 (2010).

[95] B. Liu, M. T. Lusk, and J. F. Ely, Surf. Sci. **606**, 615 (2012).

[96] A. C. Luntz, Science **302**, 70 (2003).

[97] E. Dombrowski, E. Peterson, D. F. DelSesto, and A. L. Utz, Catal. Today **244**, 10 (2014).

[98] L. B. F. Juurlink, R. R. Smith, D. R. Killelea, and A. L. Utz, Phys. Rev. Lett. **94**, 208303 (2005).

[99] L. Juurlink, P. McCabe, R. Smith, C. DiCologero, and A. Utz, Phys. Rev. Lett. **83**, 868 (1999).

[100] P. Maroni, D. C. Papageorgopoulos, M. Sacchi, T. T. Dang, R. D. Beck, and T. R. Rizzo, Phys. Rev. Lett. **94**, 246104 (2005).

[101] M. P. Schmid, P. Maroni, R. D. Beck, and T. R. Rizzo, J. Chem. Phys. **117**, 8603 (2002).

[102] R. R. Smith, D. R. Killelea, D. F. DelSesto, and A. L. Utz, Science **304**, 992 (2004).

[103] R. Bisson, M. Sacchi, T. T. Dang, B. Yoder, P. Maroni, and R. D. Beck, J. Phys. Chem. A **111**, 12679 (2007).

[104] H. L. Abbott, A. Bukoski, and I. Harrison, J. Chem. Phys. **121**, 3792 (2004).

[105] H. L. Abbott, A. Bukoski, D. F. Kavulak, and I. Harrison, J. Chem. Phys. **119**, 6407 (2003).

[106] L. Halonen, S. L. Bernasek, and D. J. Nesbitt, J. Chem. Phys. **115**, 5611 (2001).

[107] B. Jackson and S. Nave, J. Chem. Phys. **138**, 174705 (2013).

[108] B. Jackson and S. Nave, J. Chem. Phys. **135**, 114701 (2011).

[109] R. Milot and A. P. J. Jansen, **61**, 15657 (2000).

[110] S. Nave and B. Jackson, J. Chem. Phys. **130**, 054701 (2009).

[111] K. G. Prasanna, R. A. Olsen, A. Valdés, and G.-J. Kroes, Phys. Chem. Chem. Phys. **12**, 7654 (2010).

[112] A. L. Utz, Curr. Opin. Solid State Mater. Sci. **13**, 4 (2009).

[113] L. B. F. Juurlink, D. R. Killelea, and A. L. Utz, Prog. Surf. Sci. **84**, 69 (2009).

[114] W. C. Swope, H. C. Andersen, P. H. Berens, and K. R. Wilson, J. Chem. Phys. **76**, 637 (1982).

[115] H. J. C. Berendsen, J. P. M. Postma, W. F. van Gunsteren, A. Dinola, and J. R. Haak, J. Chem. Phys. **81**, 3684 (1984).

[116] G. Bussi, D. Donadio, and M. Parrinello, J. Chem. Phys. **126**, 014101 (2007).

[117] A. C. T. Van Duin, S. Dasgupta, F. Lorant, and W. A. Goddard, J. Phys. Chem. A **105**, 9396 (2001).

[118] K. Chenoweth, A. C. T. van Duin, P. Persson, M.-J. Cheng, J. Oxgaard, and W. A. Goddard, J. Phys. Chem. C **112**, 14645 (2008).

[119] K. Chenoweth, A. C. T. van Duin, and W. A. Goddard, J. Phys. Chem. A **112**, 1040 (2008).

[120] E. C. Neyts, Y. Shibuta, A. C. T. Van Duin, and A. Bogaerts, ACS Nano **4**, 6665 (2010).

[121] E. C. Neyts, A. C. T. Van Duin, and A. Bogaerts, J. Am. Chem. Soc. **133**, 17225 (2011).

[122] U. Khalilov, G. Pourtois, A. C. T. van Duin, and E. C. Neyts, Chem. Mater. **24**, 2141 (2012).

[123] T. B. Massalski, *Binary Alloy Phase Diagrams* (ASM International, 1986).

[124] W. J. Mortier, S. K. Ghosh, and S. Shankar, J. Am. Chem. Soc. **108**, 4315 (1986).

[125] G. C. Abell, Phys. Rev. B **31**, 6184 (1985).

[126] D. Brenner, Phys. Rev. B **42**, 9458 (1990).

[127] H. S. Bengaard, J. K. Nørskov, J. Sehested, B. S. Clausen, L. P. Nielsen, A. M. Molenbroek, and J. R. Rostrup-Nielsen, J. Catal. **209**, 365 (2002).

[128] A. R. Leach, *Molecular Modeling: Principles and Applications*, 2nd ed. (Prentice Hall, 2001).

[129] K. M. Kang, H. W. Kim, I. W. Shim, and H. Y. Kwak, Fuel Process. Technol. **92**, 1236 (2011).

[130] Q. Feng, T. Li, H. Yue, K. Qi, F. Bai, and J. Jin, Appl. Surf. Sci. **254**, 2262 (2008).

[131] Y. Y. Huang, Y. C. Zhou, and Y. Pan, Phys. B Condens. Matter **405**, 1335 (2010).

[132] E. C. Neyts, A. Bogaerts, R. Gijbels, J. Benedikt, and M. C. M. van de Sanden, Nucl. Instruments Methods Phys. Res. B **228**, 315 (2005).

[133] E. C. Neyts, A. Bogaerts, and M. C. M. van de Sanden, J. Appl. Phys. **99**, 014902 (2006).

[134] E. C. Neyts, M. Tacq, and A. Bogaerts, Diam. Relat. Mater. **15**, 1663 (2006).

[135] M. Eckert, E. C. Neyts, and A. Bogaerts, J. Phys. D. Appl. Phys. **41**, 032006 (2008).

[136] M. Eckert, E. C. Neyts, and A. Bogaerts, Chem. Vap. Depos. **14**, 213 (2008).

[137] M. Eckert, E. C. Neyts, and A. Bogaerts, Cryst. Growth Des. **10**, 4123 (2010).

[138] R. Saito, G. Dresselhaus, and M. S. Dresselhaus, *Physical Properties of Carbon Nanotubes* (Imperial College Press, 1998).

[139] F. Abild-Pedersen, O. Lytken, J. Engbæk, G. Nielsen, I. Chorkendorff, and J. K. Nørskov, Surf. Sci. **590**, 127 (2005).

[140] J. Engbæk, O. Lytken, J. H. Nielsen, and I. Chorkendorff, Surf. Sci. **602**, 733 (2008).

[141] A. Gutsol, A. Rabinovich, and A. Fridman, J. Phys. D. Appl. Phys. **44**, 274001 (2011).

[142] M. S. Yaghmaee, B. Shokri, N. H. Khiabani, and A. Sarani, Plasma Process. Polym. **6**, S631 (2009).

[143] W. M. Haynes, *CRC Handbook of Chemistry and Physics*, 91st ed. (CRC Press, 2010).

[144] A. Abánades, E. Ruiz, E. M. Ferruelo, F. Hernández, A. Cabanillas, J. M. Martínez-Val, J. A. Rubio, C. López, R. Gavela, G. Barrera, C. Rubbia, D. Salmieri, E. Rodilla, and D. Gutiérrez, Int. J. Hydrogen Energy **36**, 12877 (2011).

[145] G. Henkelman and H. Jónsson, J. Chem. Phys. **113**, 9978 (2000).

[146] G. Henkelman, A. Arnaldsson, and H. Jónsson, J. Chem. Phys. **124**, 044706 (2006).

[147] J. Greeley and M. Mavrikakis, J. Phys. Chem. B **109**, 3460 (2005).

[148] P. I. Lee and Schwarz J A, J. Catal. **73**, 272 (1982).

[149] Q. Wang, B.-H. Yan, Y. Jin, and Y. Cheng, Plasma Chem. Plasma Process. **29**, 217 (2009).

[150] D. H. Lee, K.-T. Kim, M. S. Cha, and Y.-H. Song, Int. J. Hydrogen Energy **35**, 10967 (2010).

[151] F. Abild-Pedersen, J. K. Nørskov, J. R. Rostrup-Nielsen, J. Sehested, and S. Helveg, Phys. Rev. B - Condens. Matter Mater. Phys. **73**, 115419 (2006).

[152] M. K. Nikoo and N. A. S. Amin, Fuel Process. Technol. **92**, 678 (2011).

[153] E. C. Neyts, J. Vac. Sci. Technol. B **30**, 030803 (2012).

[154] E. C. Neyts, A. C. T. van Duin, and A. Bogaerts, Nanoscale **5**, 7250 (2013).

[155] L. Xie, P. Brault, C. Coutanceau, J.-M. Bauchire, A. Caillard, S. Baranton, J. Berndt, and E. C. Neyts, Appl. Catal. B Environ. **162**, 21 (2015).

[156] C. H. Bartholomew, Appl. Catal. A Gen. **212**, 17 (2001).

[157] G. Herzberg and J. W. C. Johns, Astrophys. J. **158**, 399 (1969).

[158] K. K. Irikura, J. Phys. Chem. Ref. Data **36**, 389 (2007).

[159] E. C. Neyts, K. Ostrikov, Z. J. Han, S. Kumar, A. C. T. van Duin, and A. Bogaerts, Phys. Rev. Lett. **110**, 065501 (2013).

[160] S. Tinck, E. C. Neyts, and A. Bogaerts, J. Phys. Chem. C **118**, 30315 (2014).

[161] E. C. Neyts and A. Bogaerts, Carbon N. Y. **77**, 790 (2014).